Measurements of Spin Asymmetries for Deeply Virtual Compton Scattering off the Proton using the Extended Maximum Likelihood Method

Gary Douglas Smith

Submitted in fulfilment of the requirements for the degree of Doctor of Philosophy

Nuclear Physics Group

School of Physics and Astronomy

University of Glasgow

September 2013

Abstract

Generalised Parton Distributions (GPDs) provide a theoretical framework that promises to deliver new information about proton structure. In the impact parameter interpretation, they describe the substructure of the proton in terms of its quark (and gluon) constituents in three dimensions: two transverse spacial dimensions and one longitudinal momentum dimension. Through Ji's sum rule, they offer a means by which to determine the total angular momentum contribution of quarks to the proton's spin of $\hbar/2$. GPDs are directly related to Compton Form Factors (CFFs), which are distributions that are measurable using Deep Exclusive Scattering (DES) processes such as deeply virtual Compton scattering (DVCS). DVCS is characterised by the scattering of a single photon with large virtuality off a single quark (or gluon) inside the proton, resulting in the production of a hard photon: $\gamma^* p \to \gamma p'$. In this work, data recorded with the CLAS detector at Jefferson Laboratory during the EG1DVCS experimental run were analysed. This experiment ran for over 80 days with a longitudinally polarised electron beam and a solid NH_3 target containing longitudinally polarised protons. The resulting data set accommodated precise measurements of DVCS beam, target and double spin asymmetries, each of which is sensitive to different combinations of CFFs. The final results presented here are fits to these three asymmetries, which were performed using the Extended Maximum Likelihood method. It is intended that these results will be used in the future, along with other DES asymmetry and cross-section measurements, to constrain CFFs and thus move towards a more complete understanding of the structure of the proton.

Contents

List of Figures

Preface

The proton is an essential constituent of every atomic nucleus and has been studied for several decades. However, most of its properties can still not be described from first principles. Over the last two decades, developments in theories relating to the partonic substructure of protons and neutrons have motivated the experimental community to measure exclusive lepton-nucleon scattering processes, such as deeply virtual Compton scattering (DVCS). This is the subject of this work, which is arranged as follows:

The main properties of the proton are introduced in Chapter 1. To keep the discussion brief there is inevitably some assumed knowledge and no attempt has been made to arrange things chronologically. It is expected that readers will be familiar with most of this content already. In addition to the references given, [1], [2], [3] and [4] are excellent sources of further reading. This chapter aims to place this work in a global context and point out some of the unresolved questions.

Chapter 2 discusses the theoretical background and historical developments of lepton-nucleon scattering. Examples of previous experimental results are given. An overall picture of nucleon structure is portrayed then the ideas most relevant to this work are detailed. The last sections in this chapter are dedicated to the topic of DVCS. The level of detail should be sufficient for the reader to understand the significance of the results and become familiar with the terminology used whilst remaining informal enough to maintain the interest of the non-specialist.

The experimental method is outlined in Chapter 3. Chapters 4, 5 and 6 describe the analysis procedures and results. These chapters form the main body of original work.

GDS

Acknowledgements

Thanks go to Professor David Ireland and Dr Morgan Murray for their guidance and support throughout my studies. It was a pleasure to carry out this PhD under their supervision. I would also like to mention my gratitude to Prof Ralf Kaiser for offering me the position and for supervising me during my first year.

Dr Daria Sokhan, Dr David Mahon, Dr David Hamilton, Dr Bryan McKinnon and Dr Ken Livingston provided me with invaluable advice in many areas of these studies and I am indebted to them for their help and experience.

The Nuclear Physics group PhD students are what kept me going on a day-to-day basis. Thanks go to all the PhD students but in particular to Seian, Rachel, Stuart, Burger, Joe, Jen and Stef. Thanks also to the group technicians Scott and Tony.

I am grateful to Harut, Keith, Volker, Mher, Peter, Andrey, Sucheta, Erin, Suman, FX, Yelena, Stache, Angela, the Silvias and everyone else in the EG1DVCS run group.

My close friends provided the right balance of motivation and distraction throughout my PhD. A big thank you all of them and especially to William, Ally, Martin and Eddie.

My close family gave me the unfaltering support and encouragement that I needed to stay committed during the highs and lows of PhD life. A special thank you to my mother Morag, father Douglas, sister Ange, brother Daz and fiancé Susan.

Declaration

This thesis documents work that was carried out by the author between 2009 and 2013 as a member of the Nuclear Physics research group at the University of Glasgow and the CLAS collaboration at Jefferson Laboratory. No part of this thesis has been submitted elsewhere for any other degree or qualification and is all the author's own work unless otherwise referenced in the text.

Chapter 1

Properties of the Proton

1.1 Charge

In 2011 the scientific community celebrated the centenary year of Ernest Rutherford and the birth of nuclear physics. It is well known that the experiments that Geiger and Marsden performed under his supervision, using thin sheets of gold foil, led to the discovery of the atomic nucleus [5]. They later carried out experiments using targets consisting of various gases. Rutherford made the following remark in the journal *Philosophical Magazine* a century ago this year [6]:

> The observations on the scattering of α-particles by matter in general afford strong experimental evidence for the theory that the atom consists of a positively charged nucleus of minute dimensions surrounded by a compensating distribution of negative electrons. The charge on the nucleus for heavy atoms is approximately $\frac{1}{2}Ae$ where A is the atomic weight and e the electronic charge. The experiments in this paper on the scattering of simple gases indicate that the hydrogen atom has the simplest possible structure of a nucleus with one unit charge, and helium comes next with a nucleus of two unit charges. This simple structure for hydrogen and helium atoms has been assumed by Bohr [7] in a recent interesting paper on the constitution of atoms, and has been shown by him to yield very promising results.

Comparison of the relative scattering coefficients for α-particles on light nuclei led to the conclusion that the hydrogen atom has a nucleus with charge $+1$. The name *proton* (Greek for 'first') was coined by Rutherford 7 years later [8]. Table 1.1 lists some values of the static properties of the proton and its isospin partner, the neutron, which was discovered by Chadwick in 1932 [9].

	Proton	Neutron
Charge (e)	+1	0
Mass (MeV/c^2)	938	940
Isospin component	$\frac{1}{2}$	$-\frac{1}{2}$
Spin ($\hbar$)	$\frac{1}{2}$	$\frac{1}{2}$
Magnetic moment (μ_N)	2.79	-1.91
Charge radius (fm)	0.877	n/a
Valence quark content	uud	udd

Table 1.1: Static properties of the nucleon [10].

1.2 Isospin and the Nucleon

The similarity between proton and neutron masses led Heisenberg to postulate that they were two different charge states of the same particle, the nucleon [11]. The quantum number isospin was introduced to explain this symmetry. Isospin takes its name from the similarity its mathematical formalism has to that of spin. The isospin components (I_3) for a given isospin value (I) are enumerated in the same way as spin projections (m_s) are enumerated for a given spin angular momentum (s), but with no physical analogy. The nucleon has an isospin of $\frac{1}{2}$, the proton and neutron have respectively $+\frac{1}{2}$ and $-\frac{1}{2}$ components. Isospin reflects the observation that the (charge-independent) nuclear force has a similar effect on both protons and neutrons. In other words, the strong force is sensitive only to the magnitude of isospin and not its 'direction'.

1.3 Spin Crisis

Spin is a quantum number that accounts for the portion of angular momentum that a particle has which does not arise from its orbital motion. It was first experimentally observed by Gerlach and Stern in 1922 [12]. Protons are classified as fermions, half-odd integer spin particles ($\frac{1}{2}, \frac{3}{2}, \frac{4}{2}, \ldots$ in units of $\hbar$) that obey the Pauli exclusion principle. Quarks are also fermions. This led to the naïve assumption that the proton's spin of $\frac{1}{2}$ was the net result of the addition of the spins from two (spin $\frac{1}{2}$) up quarks and one (spin $-\frac{1}{2}$) down quark. The discovery by the European Muon Collaboration (EMC) that the contribution to the proton's spin from the combined spins of quarks ($\Delta\Sigma$) could only account for a small fraction [13] led to the so-called *spin crisis* of nuclear physics. The remainder of the proton's spin may arise from the orbital angular momenta of quarks (L_q) the orbital angular momenta of gluons (L_g), or gluon helicities (Δg)

$$\frac{1}{2} = \frac{1}{2}\Delta\Sigma + L_q + \Delta g + L_g = J_q + J_g; \tag{1.1}$$

where J_q (J_g) is the total angular momentum contribution from quarks (gluons) and the factor of $\frac{1}{2}$ before the quark spin contribution is a historical convention. In 1996, Ji described a means by which to access J_q using deeply virtual Compton scattering [14]. The spin crisis is an open problem in hadron physics and one of the key motivations for undertaking work such as this.

1.4 Wait a Magnetic Moment

The earliest indication that the proton was not an elementary particle came from the measurement of its magnetic moment [15]. If the proton were a point-like Dirac particle, the expected value would equal one nuclear magnetron (μ_N). Instead it is found to be 2.79 μ_N and is thus given the name *anomalous* magnetic moment. Although it is now known to be due to the underlying dynamic substructure of quarks, the discrepancy is still not well understood.

1.5 Puzzling Radius

The size of the proton is usually quantified in terms of its root-mean-squared electric charge radius. The official 2010 CODATA[1] value uses a combination of results from atomic spectroscopy and elastic electron scattering experiments [16]. Elastic scattering will be discussed in more detail in the next chapter. Recently there has been some controversy regarding the size of protons due to a precise result that was obtained using laser spectroscopy on muonic hydrogen [17]. This result disagrees with the official 2010 CODATA value by 7-σ.

Elastic electron scattering measurements on targets containing neutrons [18], and experiments with slow neutron beams on the electron cloud of heavy atoms [19], have shown that despite possessing no overall charge, neutrons also possess a charge distribution [20] - a result that would clearly not be possible if neutrons were elementary.

1.6 Quark Model

The quark model developed out of the *eightfold way* of Gell-Mann and Ne'eman [21]: a system of categorising hadrons according to isospin, charge and strangeness. Using this system, only three fundamental particles are needed to account for the quantum numbers of the lightest baryons: up, down and strange quarks. This scheme is illustrated for the

[1] The Committee on Data for Science and Technology

eight spin-1/2 baryons in Figure 1.1. Many searches for free quarks were carried out but

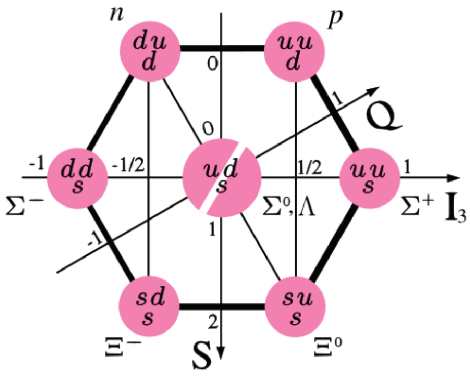

Figure 1.1: The Baryon octet. Each particle is made up from three valence quarks and has a total spin of $\frac{1}{2}$. Charge increases on the axis labelled Q, and the x and y axes correspond to increasing strangeness (S) and isospin component (I_3) respectively. It is a more common convention to assign each strange quark with the value $S = -1$.

proved fruitless, which at the time brought into some question the validity of the model. Successes such as the prediction and subsequent discovery of the spin-$\frac{3}{2}$ Ω^- [22], however, provided strong evidence in support. Since the development of the parton model of Feynman [23] and Bjorken [24], the existence of quarks has been generally accepted. They were able to explain the results of deep inelastic scattering experiments by postulating the existence of point-like sub-nucleonic particles, which they called partons. The properties of partons were found to show consistency with those of quarks. Deep inelastic scattering and the parton model will be discussed in the next chapter. The explanation for the lack of observation of free quarks is now understood to be the result of the behaviour of the strong force, which is explained in the theory of quantum chromodynamics (QCD).

1.7 Quantum Chromodynamics

The global properties of the proton have so far eluded any rigorous explanation from the most advanced fundamental theories of the standard model of particle physics. The difficulties arise from the complexity of QCD at small energy-scales, where the strong coupling constant (α_s) is relatively large. Figure 1.2 shows a graph of the world data for the strong coupling constant as a function of energy scale (Q). The magnitude of the coupling constant for low-Q (soft) QCD processes means that it is an unreasonable approximation to neglect higher order terms ($\sim \alpha_s^n : n \in \mathbb{Z} > 1$). This prevents soft QCD processes from being solved perturbatively. In contrast, for quantum electrodynamics (QED) a perturbative approach is possible, because the fine structure constant is small ($\alpha^{-1} \approx 137$) and does not vary by much depending on the energy-scale. Theoretical descriptions of soft

hadronic processes are instead formulated using quark models, effective field theories, sum rules and lattice QCD calculations. These approaches can only progress with the feedback from precise experimental results.

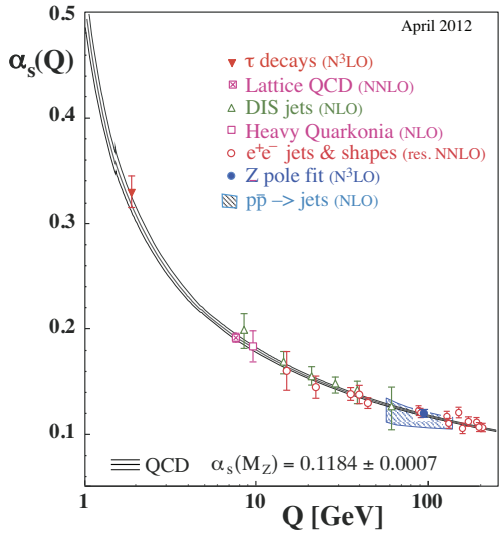

Figure 1.2: The Strong Coupling Constant. [25]

The behaviour of the strong force at small energy scales, or equivalently large distance-scales, gives rise to the property known as *confinement*. Separating quarks by an increasing amount requires more and more energy to be put into the system. Before enough energy is provided to free a quark, the creation of a new quark-anti quark pair becomes more probable. This means that quarks are never observed as free particles and exist only in colour-neutral systems, hadrons.

Colour in the context of QCD represents the equivalent of charge in QED. It is the property which is used to describe how strong-force interacting particles behave. There are three colours (red, green and blue), and their anti-colours, that represent possible allowed states according to the SU(3) symmetry group formalism on which QCD theory is based.

The most striking difference to QED is that the force-carrying particles of QCD (gluons) possess colour charge, whereas in QED the force carriers (photons) are neutral. This gives rise to the phenomenon known as *asymptotic freedom*. At small distance-scales, the colour potential is weak [4], which is caused by *anti-screening* [1]. Since gluons possess colour charge, they do not only interact with quarks but also with other gluons: QCD is a *non-Abelian* gauge theory. At short distances the 'bare' quark (current quark) colour-field potential is reduced by the self-interacting gluon field around it. This means that the mutual force that two quarks experience is negligible when they are close together, and they act as though they are almost free.

1.8 Summary

The purpose of this chapter was to review some of the defining properties of the proton and introduce the notion that these properties must arise from a complex and dynamic underlying substructure. The goal of hadron structure physics is to explain how the interplay between quarks, and gluons in a bound colour-neutral system gives rise to these properties.

Chapter 2

Proton Structure and Electron Scattering

The majority of detailed information about nucleon structure that is already known has been obtained in lepton-nucleon scattering experiments. This approach is complemented by the use of real photon beams, which are also employed in the investigation of nucleon resonances. The study of nucleon resonances provides an important means by which to test quark-model predictions, and is a rich field of research in itself. However, the purpose of this chapter is to explain the significance of a specific type of deep exclusive scattering (DES) process called deeply virtual Compton scattering (DVCS). DVCS is a sub-process of the exclusive leptoproduction of real photons and is accessible through lepton scattering reactions. To reflect the rest of the content in this thesis, electron scattering will be focussed on here.

The discussion will be approached by introducing two types of reactions that are well studied, and to which DVCS is related: elastic scattering and inclusive deep inelastic scattering (DIS). Exclusive processes, such as DVCS and deeply virtual meson production (DVMP) link the results of elastic scattering and DIS experiments by providing a means to measure generalised parton distributions (GPDs). As their name suggests, GPDs provide a more general picture about nucleon structure and the possibility to access new information such as correlated distributions of the transverse positions and longitudinal momentum of partons.

To begin with, a brief description of the most general type of parton distributions, Wigner distributions, will be given. There is presently no known means by which to measure these quantities directly, but by considering nucleon structure from this starting point, it will be clearer to see how other types of distributions that *are* measurable are related, and the limits to what information may be attained overall. The approach will be largely descriptive with the goal of giving the reader an accurate overview of the field

without confusing the most important points with technical details.

2.1 Wigner Distributions

From a classical physics perspective, the state of a gas of particles can be completely described using a phase space distribution $f(\vec{r},\vec{p})$. At any instant of time, the position ($\vec{r}$) and momentum ($\vec{p}$) vectors may in principle both be known exactly for each particle. By extending this idea to include quantum mechanics, the precision with which these conjugate variables can be known simultaneously becomes limited according to the Heisenberg uncertainty principle:

$$\Delta x \Delta p_x \geq \hbar/2, \tag{2.1}$$

where Δx is the uncertainty in one spacial coordinate and Δp_x is the uncertainty in momentum for the same direction. A reminder is given that there is no such restriction for components of position and momentum that are orthogonal.

A Wigner distribution is an example of a quantum mechanical equivalent of a classical phase-space distribution, and reduces to one in the classical limit [14, 26]. Figure 2.1 illustrates the relationship between nucleon Wigner distributions, and other nucleon structure distributions. The complete measurement of generalised transverse momentum distributions (GTMDs) would, via a Fourier transform in the variable that quantifies the transfer of momentum to the nucleon ($\Delta = p' - p$), give access to corresponding Wigner distributions for partons in the proton in five dimensions (two position, three momentum) and thus determine the most complete information on its state [27].

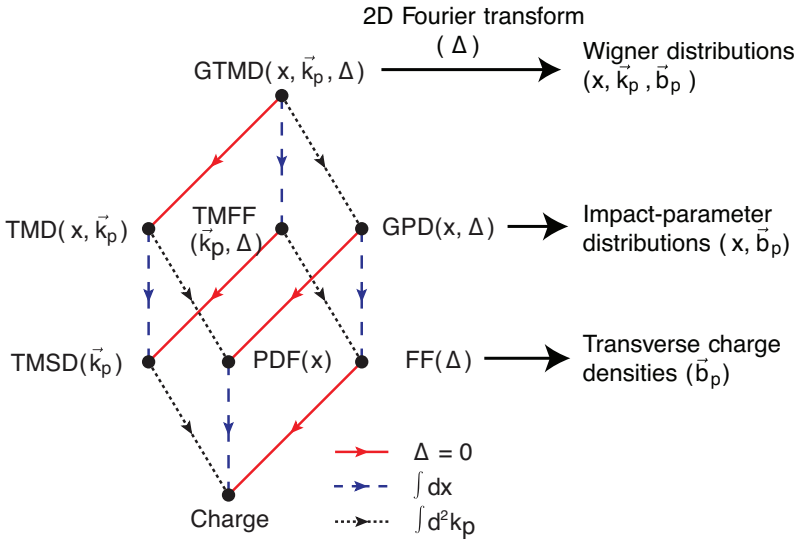

Figure 2.1: Nucleon Structure in the context of Wigner Distributions. Figure adapted from [27].

In practice, in terms of position, only the transverse coordinates of partons can be determined, which are defined in terms of impact parameter ($\vec{b_p}$) space - where distance is given relative to the centre of mass of the system. Exploration of the structure on the distance scales required, necessitates that the interacting particle (probe) carries a large negative squared four-momentum; this will be explained more in Section 2.3. The direction of propagation of the probe is used to define the longitudinal direction. Since the longitudinal momentum is known with precision, this prevents the longitudinal position from being resolved. The Heisenberg uncertainty relation imposes this restriction. The information about nucleon structure that is attainable at present is limited to projections of Wigner distributions. To the author's knowledge there is currently no theoretical formalism that indicates how GTMDs may be measured directly [28].

Integrating GTMDs over the transverse momentum of partons ($\vec{k_p}$) leads to GPDs, probability amplitudes in longitudinal momentum space; x is the fraction of the nucleon's longitudinal momentum held by the parton. GPDs will be discussed in Section 2.4. Alternatively GTMDs in the forward limit ($\Delta = 0$) are transverse momentum distributions (TMDs). TMDs are accessible through semi-inclusive DIS measurements (SIDIS) [29], and experimental programs to measure them are ongoing [30–33]. In the lower half of Figure 2.1 are various types of form factors, which correspond to the parton distributions above them, with the longitudinal momentum dependence integrated out. Only standard form factors (FFs), and their forward limit, charge, are mentioned here. For explanations of transverse momentum form factors (TMFFs) and transverse momentum spin densities (TMSDs) and a formal treatment of GTMDs the reader is referred to [27].

The first measurements made that correspond to projections of nucleon Wigner distributions were charge, form factors (FFs), and parton distribution functions (PDF). These quantities are also projections of GPDs which means that some information about GPDs is already known. It will be shown in the following sections how these distributions are used as a means to constrain GPD models.

2.2 Elastic Scattering

The elastic scattering of an electron (e) on a proton target (p) is defined:

$$e(e) + p(p) \rightarrow e'(e') + p'(p'), \tag{2.2}$$

where the arguments for each particle are the respective four-momenta. This type of reaction has been used to investigate nucleon structure since the mid-1950s. Figure 2.2(a) shows what was, at the time, a ground-breaking elastic electron-proton scattering result, in which an experimentally-determined cross section is compared to theoretical curves.

The theoretical cross section for a relativistic electron, scattering on a point-like particle with charge e_q, is given by the Mott cross section [2]:

$$\left(\frac{d\sigma}{d\Omega}\right)_{Mott} = \frac{\alpha^2}{4E^2\sin^4\frac{\theta}{2}}\frac{E'}{E}\cos^2\frac{\theta}{2}, \tag{2.3}$$

where θ is the electron scattering angle, E (E') is the electron energy before (after) scattering, $d\Omega$ is the solid angle into which the electron is scattered, and $\alpha = e_q^2/(4\pi)$, is the fine structure constant. The measured cross section in the figure deviates from the Mott curve increasingly at large scattering angles. Other theoretical curves that modelled the proton as a point-like object but included the proton's magnetic moment and/or intrinsic spin also failed to agree with the data [34]. This disagreement is understood to be due to the proton having extended structure. Hofstadter's work in this area of research led him to win the Noble prize in 1961. See [35] for a comprehensive review by him.

2.2.1 Form Factors

The Rosenbluth formula [2]:

$$\left(\frac{d\sigma}{d\Omega}\right)_{exp.} = \left(\frac{d\sigma}{d\Omega}\right)_{Mott}\left(\frac{G_E^2(Q^2)+\frac{Q^2}{4M^2}G_M^2(Q^2)}{1+\frac{Q^2}{4M^2}} + \frac{Q^2}{2M^2}G_M^2(Q^2)\tan^2\frac{\theta}{2}\right), \tag{2.4}$$

where M is the nucleon mass, describes the elastic electron-nucleon cross section in terms of the Mott cross-section and the electric (G_E) and magnetic (G_M) *Sachs* form factors, which are functions of the negative squared four-momentum transfer:

$$Q^2 = -q^2, \tag{2.5}$$

where $q = (\nu, \vec{q}) = e - e'$ is the difference in the electron four-momentum before and after scattering. Since the process is elastic means that $t \equiv \Delta^2 = (p'-p)^2 = q^2$. Form factors are sometimes stated as functions of t, or Δ, instead of Q^2. Figure 2.3(a) is an illustration representing elastic scattering of an electron off a proton through the exchange of a single photon. In this representation, which is called the Born approximation, Q^2 is the *virtuality* of the exchanged photon. A full representation of the reaction would include higher order diagrams including: the exchange of two photons, loops to account for the emission and subsequent reabsorption of a photon, and the radiative emission of a photon. Corrections are often carried out to remove any effect caused by the radiative emission of photons. Calculations indicate that other higher order terms should be negligible [36].

In Equation 2.4, the second bracketed term on the right-hand-side is a semi-empirical

parameterisation that accommodates for the target particle being spin 1/2 in nature, with an anomalous magnetic moment and extended structure [2]. In the limit $Q^2 = 0$, G_E is the charge of the nucleon and G_M is its anomalous magnetic moment. Sachs form factors are determined by comparing the experimentally measured cross-section to the Mott cross section at fixed values of Q^2 for various electron scattering angles, and performing a *Rosenbluth separation* [37, 38]. Figure 2.2(b) shows graphs of Sachs form factors for protons and neutrons using world data [39].

The interpretation of Sachs form factors at an arbitrary fixed value of Q^2 is most easily understood in the Breit frame. In this frame there is no energy transfer ($\nu = 0$) and the Fourier transform of G_E (G_M) is analogous to a classical charge distribution (magnetisation density) [2]. Similar to the way in which the Fourier transform of the diffraction pattern of a light source returns the spacial dimensions of the object from which the light was diffracted, the Fourier transform of a nucleon's (or nucleus') form factor provides information on the spacial distributions of charges and currents, and thus its extended structure.

In the last decade and a half there has been a revival of form factor measurements due to improvements in the production of polarised beams and polarimeter technology. Precise results have been determined over a large range of Q^2 using the polarisation transfer technique ($\vec{e}p \rightarrow e\vec{p}$) [40–42]. A surprising discrepancy is observed when the ratio of electric to magnetic form factors for unpolarised measurements and polarised measurements are compared. For the unpolarised results, the ratio appears to be constant as a function of Q^2. This is known as form factor scaling. In contrast, there is a distinctive drop-off when the polarised results are instead compared. This discrepancy is yet to be resolved but one suggestion is that although the contribution from two-photon exchange is expected to be small, it may still play a significant role [43]. Dedicated two-photon exchange experiments have since been carried out [44, 45]. The results are yet to be confirmed.

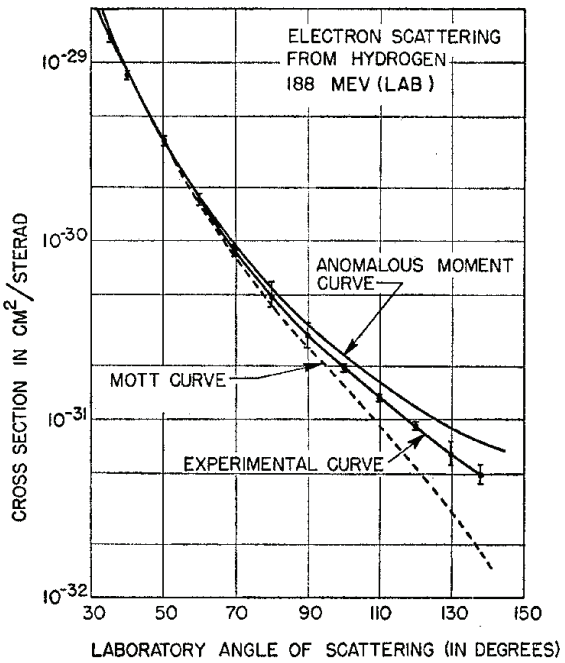

(a) Elastic electron scattering cross section result from SLAC, published in 1955. The deviation of the experimental curve from the Mott cross section is apparent [34].

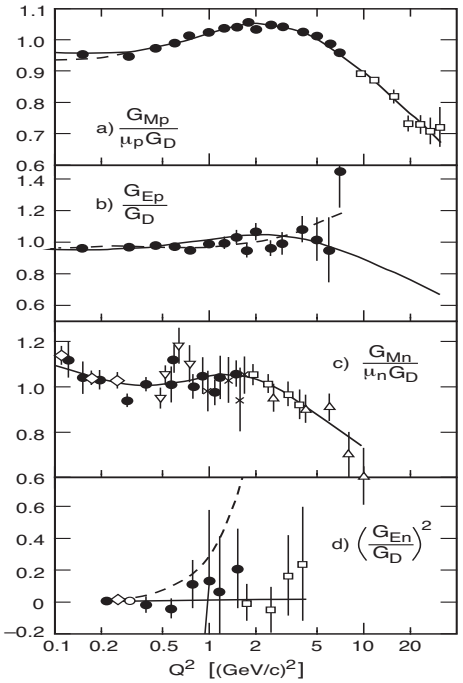

(b) Electromagnetic form factor measurements for protons and neutrons using world data. Data points are normalised to a dipole parameterisation [39].

Figure 2.2: Results from elastic scattering measurements, which indicate that the nucleon has extended structure.

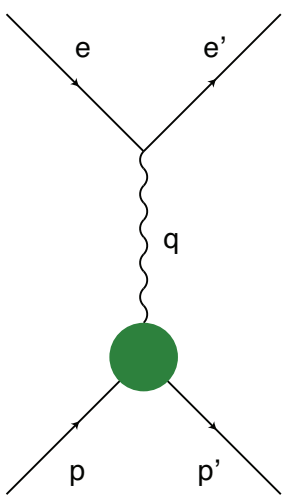

(a) Elastic scattering.

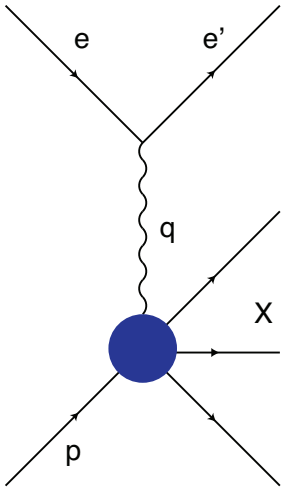

(b) Deep inelastic scattering.

Figure 2.3: Illustrations of two types of electron-proton scattering reactions. Variables are defined in the text.

2.3 Deep Inelastic Scattering

Deep inelastic scattering (DIS) is a reaction that is used to investigate nucleon structure in terms of parton distributions. The first DIS experiments were performed at the Stanford Linear Accelerator (SLAC) in the late 1960s and early 1970s [46]. The electron beam at SLAC was capable of reaching higher energies and luminosities than previous accelerators had been able to, opening up a new kinematic region in which protons could be studied.

In general, for an experiment in which an electron is scattered off a proton, the invariant mass of the virtual photon-proton system (or final-state hadronic system) is

$$W^2 = (p+q)^2 = M^2 + 2M\nu - Q^2, \tag{2.6}$$

where p (M) is the proton four-momentum (mass). For the elastic scattering case $W^2 = M^2$, and $2M\nu = Q^2$. The deep inelastic regime corresponds to reactions in which W^2 is large enough to reach beyond any individually distinguishable proton resonance, and Q^2 and ν are large enough so that the virtual photon wavelength:

$$\lambda \geq \frac{\hbar}{2\sqrt{Q^2+\nu^2}} = \frac{\hbar}{2|\vec{p}|}, \tag{2.7}$$

is small enough to be capable of probing the proton's substructure. Typical values that are used in practice are: $W > 2\ GeV/c^2$, $Q^2 > 1\ (GeV/c)^2$. Through Equation 2.6 these conditions also impose a lower limit on ν.

In the most simple type of DIS experiment, the electron beam interacts with the proton target and only the scattered electron is detected in the final state. All possible final states involving the nucleon-virtual photon system are *included* in reconstructions, which is why this type of measurement is termed *inclusive*. Figure 2.3(b) is an illustration of inclusive DIS. In terms of particles and their respective four-momenta the reaction is

$$e(e) + p(p) \rightarrow e'(e') + X, \tag{2.8}$$

where X is the (unknown) final state hadronic system.

The most immediately striking result from DIS experiments was the phenomenon known as scaling. In the elastic scattering case, a dependence of the cross-section on Q^2 indicated that the proton has extended structure. For DIS, it was found that the cross-section was almost independent of Q^2. This suggested that there is no form factor associated with the proton's constituent particles, or in other words they appear to be point-like. The theoretical formalism behind scaling is given in terms of the Parton Model. An out-

line based on the treatment given in [2] will now be given.

2.3.1 Parton Model

For inelastic scattering, $W^2 > M^2$ and $2M\nu > Q^2$. One way to quantify the inelasticity of the process is with the dimensionless variable:

$$x_B = \frac{Q^2}{2p\cdot q} = \frac{Q^2}{2M\nu}, \tag{2.9}$$

which is known as x-Bjorken. In the parton model, x-Bjorken equates to the fraction of the nucleon's momentum held by the struck quark, as will now be explained.

A frame of reference (f) is chosen in which the momentum of the proton approaches infinity in one direction, here taken as the longitudinal direction; this is known as an *infinite momentum frame*. The virtual photon momentum remains unchanged by applying the conditions $q_f^2 = -Q^2$ and $p_f \cdot q_f = p\cdot q$. These conditions allow the *impulse approximation* to be applied, which is that the proton constituents must be non-interacting due to time-dilation. In terms of the fraction of the nucleon's longitudinal momentum held by the active parton, x, the invariant mass of the parton-virtual photon system is

$$(xp_f + q_f)^2 = x^2M^2 - Q^2 + 2xp_f\cdot q_f; \tag{2.10}$$

which must be approximately zero since the partons are non-interacting and must therefore be on-shell and thus adhere to Einstein's energy equation. This implies that $x = x_B$, since x^2M^2 is much smaller than both Q^2 and ν. The parton model is often said to be valid in the Bjorken limit, which is $Q^2 \to \infty$ at fixed x_B.

2.3.2 Structure Functions

The double differential cross-section for unpolarised inclusive DIS is given by

$$\frac{d^2\sigma}{d\Omega dE'} = \frac{\alpha^2}{4E^2\sin^4\frac{\theta}{2}}\left(W_2(\nu,Q^2)\cos^2\frac{\theta}{2} + 2W_1(\nu,Q^2)\sin^2\frac{\theta}{2}\right), \tag{2.11}$$

where W_1 and W_2 are structure functions that describe the response of the nucleon. It is instructive to define these hadronic elements in terms of dimensionless structure functions:

$$F_1(x,Q^2) = MW_1(\nu,Q^2), \tag{2.12}$$

$$F_2(x,Q^2) = \nu W_2(\nu,Q^2). \tag{2.13}$$

Figure 2.4(b) shows a large selection of the world data for the structure function F_2 for the proton. At values of $0.08 < x < 0.4$, F_2 is relatively constant when plotted against Q^2, which is an exhibition of scaling. Deviations from this trend at smaller values of x are due to the increased probability of interacting with quark anti-quark pairs that are created out of the vacuum (sea quarks).

Interpreted within the Parton Model, these structure functions are simply related to a sum over each quark type i, of the number densities of partons $q_i(x)$, weighted by their charge e_q

$$F_1(x) = \frac{1}{2}\sum_i e_q^2 q_i(x). \tag{2.14}$$

These number densities are the parton distribution functions (PDFs).

The Callan-Gross relation:

$$F_2(x) = 2xF_1(x) = x\sum_i e_q^2 q_i(x); \tag{2.15}$$

provides a direct connection between both structure functions. It assumes that partons are spin-1/2 particles. Experimental confirmation of the Callan-Gross relation therefore provided evidence that this property of partons is consistent with quarks.

Figure 2.4(a) shows a graph of proton PDFs for partons of different flavours, and gluons. The up and down valence quarks (u_v, d_v) are seen to dominate at $x \approx 1/3$, with about twice the contribution coming from up quarks as down quarks. This agrees with the quark model which states that the proton contains one down and two up valence quarks. As x gets smaller, the increasingly large contribution from sea quarks (d, u, s, c) and gluons (g) is evident.

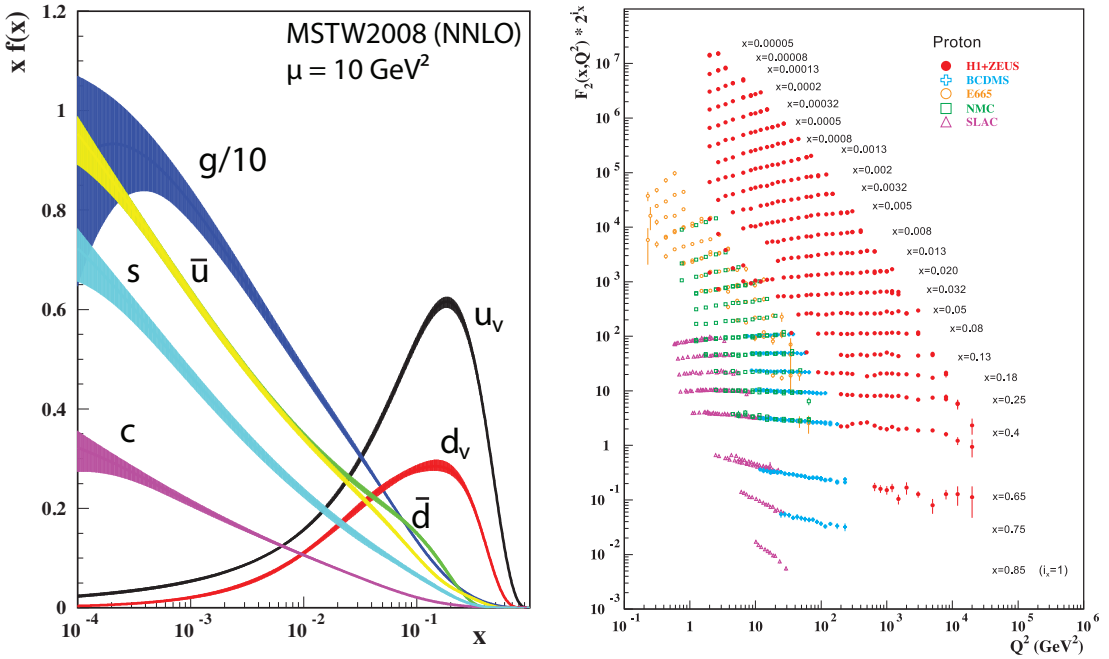

(a) Unpolarised parton distribution functions.

(b) The proton structure function F_2^p measured using lepton scattering on protons.

Figure 2.4: Results from DIS experiments relating to the parton structure of nucleons [10].

2.4 GPDs and Deep Exclusive Scattering

In the previous sections it was shown that form factor and PDF measurements can be used to provide complementary information about nucleon structure. Physical interpretations of these one-dimensional parameterisations lead to one-dimensional 'images' of the nucleon in terms of impact parameter space and longitudinal momentum space respectively. In the case of form factors, a two-dimensional spacial representation can be made by imposing rotational symmetry in the transverse plane. The concentration of the discussion will now move towards the methods used to extend these ideas, and access a more complete picture of nucleon structure by studying deep exclusive scattering (DES).

2.4.1 Initial developments

During the 1990s, Müller et al [47], Radyushkin [48] and Ji [14, 49], amongst others[1], made significant advancements to the theoretical framework surrounding parton distributions by suggesting a means to access *non-forward* non-local matrix elements through DES processes [51]. Originally given the name off-forward parton distributions, generalised parton distributions (GPDs) were shown to be accessible through deeply virtual Compton scattering (DVCS) and deeply virtual meson production (DVMP) [52].

The off-forwardness of processes such as DVCS and DVMP arises from the fact that the momentum of the nucleon is allowed to change whilst the scattering occurs; this will be explained below in the section on GPD variables. The non-local property refers to the fact that the position of the interacting quark is not restricted to one spacial location during the scattering process. By comparison PDFs describe forward non-local processes and FFs describe non-forward local processes [51].

In 2000, a method was found to interpret GPDs in terms of correlated transverse positions and longitudinal momenta of partons [53], and therefore provide a means by which to describe nucleon structure in terms of the distribution of quarks (and gluons) in three mixed momentum and space coordinates. This will be explained in more detail in Section 2.4.11.

This section is dedicated to some of the main aspects of GPDs including their interpretation, and relationships to form factors and PDFs. Some GPD models will also be mentioned. To follow the discussion it is necessary to first become familiar with some important QCD concepts that arise in the GPD framework. For a recent review article containing a more rigorous treatment of the ideas relevant to this work also see "GPDs in the valence region from DVCS" [51].

[1] See, for example, [50] for an extensive description of GPDs, which includes references to many of the most significant journals that contributed to their initial development.

2.4.2 Factorisation

The benefit of using electromagnetic probes to study hadrons comes from the fact that they are structureless in nature, accommodating precise calculations of the processes they are involved in. With the correct formulation, the QED subprocesses in lepton-hadron reactions can be separated from the QCD subprocesses. Where hard and soft QCD processes contribute, they may also be separable. When this is the case, the only incalculable quantities that remain are the soft QCD processes. These are parameterised using models that are tested experimentally. In general the technique of separating out reaction subprocesses into those that are calculable and those that are parameterised is called *factorisation*. Given the complexity of QCD at small energy-scales, factorisation is an essential tool for the hadron structure physicist.

2.4.3 Universality

It can be the case for two (or more) types of hadronic reactions, that the calculable hard processes are different, but the incalculable soft processes are identical. Universality is the term used to describe the fact that such identical soft process distributions share the same fundamental description. Universality can only be applied to a reaction when a factorisation proof exists.

The use of models to describe complimentary processes is a means by which to cross-check them. If a process is well known in one context, that knowledge is still valid in another context. This means that when a known process mixes with an unknown process, the information on the known process can be used to deduce information on the unknown one. In Figure 2.5, leading order diagrams for the exclusive leptoproduction of photons (2.5(a)) and mesons (2.5(b)) are given. The large red blobs in both represent the same GPDs. The smaller light-blue blob in Figure 2.5(b) is known as a *distribution amplitude* (DA). The relevant DAs for the meson in the reaction being studied can be determined independently using hadron-hadron reactions.

2.4.4 Twist

Twist is formally defined as the dimension of the hadronic tensor minus its spin [54]. The redefinition given in [55] relates more closely to phenomenology. Higher orders of twist are suppressed by a power of $M/\sqrt{Q^2}$. Leading order calculations correspond to those involving twist-2 elements only. There are only four quark-helicity conserving GPDs at the twist-2 level. These GPDs will be discussed below.

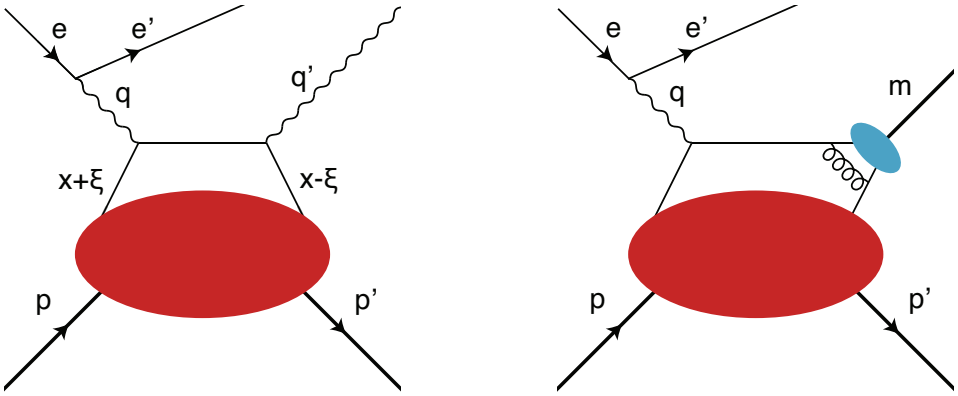

(a) Deeply virtual Compton scattering. (b) Deeply virtual meson production.

Figure 2.5: Illustrations of deep exclusive processes. Variables are defined in the text.

2.4.5 GPD variables

The exclusive electroproduction of real photons is defined:

$$e(e) + p(p) \rightarrow e'(e') + p'(p') + \gamma(q'), \tag{2.16}$$

where γ is the produced photon, and other variables take the same meanings as before. Virtual Compton Scattering (VCS) is a subprocess of this reaction, given by:

$$\gamma^*(q) + p(p) \rightarrow p'(p') + \gamma(q'), \tag{2.17}$$

where γ^* is the virtual photon probe with four-momentum q defined as before.

It is in the Bjorken limit that this reaction is given the name *deeply* virtual Compton scattering (DVCS). DVCS is dominated by the twist-2 process shown in Figure 2.5(a). This is known as the *handbag approximation* and corresponds to the virtual photon probe interacting with a single quark. There are no gluon vertices in this diagram, making it the simplest process with which GPDs can be studied. For this reason, in the context of GPDs, DVCS is sometimes referred to as the "golden channel".

The interpretation of GPDs is conveniently done in the light-front frame, with the virtual photon and proton travelling at the speed of light along opposite longitudinal directions; given by the 3rd (or z) component here[2]. This is another example of an infinite

[2]This refers to the directions of the virtual photon four-momentum and average of the proton four-momentum before and after scattering.

momentum frame. General vectors in light cone coordinates are defined:

$$v^+ = \frac{1}{\sqrt{2}}(v_0 + v_3), \qquad v^- = \frac{1}{\sqrt{2}}(v_0 - v_3), \qquad v^\perp = (v_1, v_2). \tag{2.18}$$

This system has the advantage that particles travelling along the ($+$ or $-$) z-direction at the speed of light have only one ($+$ or $-$) light cone coordinate component, which greatly simplifies calculations [54].

GPDs are given as functions of the variables x, t, and ξ. Various (equivalent) conventions exist for these variables; the system used in [56] is adopted here. GPDs also have a Q^2 dependence, which is governed by the hard scattering part of the process. This can be calculated using QCD evolution equations and is therefore usually omitted [51]. The average fractional momentum of the struck quark x is defined by

$$k^+ = xP^+, \tag{2.19}$$

where k is the average quark momentum and $P = \frac{1}{2}(p + p')$ is the average momentum of the proton. This variable is not experimentally measurable using DVCS, which results in complications in accessing GPDs. The skewness variable ξ is defined by

$$\Delta^+ = -2\xi P^+, \tag{2.20}$$

and equates to minus half the longitudinal momentum fraction transferred to the struck quark. As shown in Figure 2.5(a), this means that prior to scattering the interacting quark has momentum fraction $x + \xi$, and after scattering it has $x - \xi$. The variable t takes the same definition as for elastic scattering:

$$t = \Delta^2 = (p' - p)^2. \tag{2.21}$$

Associated with t is a transverse momentum 'kick', $\Delta_\perp^2$, that the nucleon experiences during the interaction. An additional constraint for the handbag approximation to be valid is that t must be small [50]. The momentum transfer ξ is said to occur at the quark level and $\Delta_\perp^2$ at the nucleon level [54].

It is important to note that GPDs are not interpreted in a framework where the fractional momentum of the struck parton x is equal to the scaling variable x_B, as was the case for the Parton Model. In fact x_B is more closely related to the skewness variable, which may be written [57]:

$$\xi = x_B \frac{1 + \frac{t}{2Q^2}}{2 - x_B + x_B \frac{t}{Q^2}}. \tag{2.22}$$

In the Bjorken limit with small t, giving $Q^2 >> |t|$, this reduces to

$$\xi \approx \frac{x_B}{2 - x_B}. \tag{2.23}$$

Experimentally, only t and ξ are accessible for DVCS and DVMP. Double deeply virtual Compton scattering can in principle be used to access x but the cross-section for this reaction is expected to be over two orders of magnitude smaller than DVCS [58]. Extraction of the x-dependence of GPDs in general relies on the application of model predictions, with some exceptions: for example, the extraction of GPDs at the point $x = \xi$.

In principle x and ξ range between -1 and 1, but time reversal invariance prevents ξ from taking negative values [51]. In the case $x > \xi$ ($x < -\xi$), GPDs represent the probability amplitude of interacting with a quark (anti-quark). In the case $-\xi < x < \xi$ the virtual photon probe initially interacts with a quark (or anti-quark) which is then put back into the nucleon as an anti-quark (quark). For this scenario GPDs represent the probability to interact with a quark anti-quark pair in the nucleon [51].

2.4.6 Leading order GPDs

For nucleons there are four twist-2 quark-helicity conserving GPDs for each quark flavour $q = u, d, s$. H_q and $\widetilde{H}_q$ are nucleon helicity conserving, whilst E_q and $\widetilde{E}_q$ are nucleon helicity flipping [14]. Since they do not depend on quark-helicity, H_q and E_q are called unpolarised GPDs. $\widetilde{H}_q$ and $\widetilde{E}_q$ are quark-helicity dependent and are thus called polarised GPDs [54]. GPDs of higher twist and those for which quark helicity is not conserved also exist, but descriptions of them are out of the scope of this work. The discussion here is restricted to the four GPDs mentioned above, which are leading order in the perturbative expansion of the scattering process.

2.4.7 Relation to FFs

The first x-moments of the leading order GPDs are the elastic scattering form factors **??**:

$$\begin{aligned}
\int_{-1}^{1} H_q(x,\xi,t)dx &= F_1(t), \\
\int_{-1}^{1} \widetilde{H}_q(x,\xi,t)dx &= F_2(t), \\
\int_{-1}^{1} E_q(x,\xi,t)dx &= G_A(t), \\
\int_{-1}^{1} \widetilde{E}_q(x,\xi,t)dx &= G_P(t).
\end{aligned} \tag{2.24}$$

$F_1(t)$ and $F_2(t)$ are the Dirac and Pauli form factors[3], which are related to the Sachs form factors that were discussed in Section 2.2 by

$$\begin{aligned} G_E(Q^2) &= F_1(Q^2) - \frac{Q^2}{4M^2}F_2(Q^2) \\ G_M(Q^2) &= F_1(Q^2) + F_2(Q^2); \end{aligned} \tag{2.25}$$

$G_A(t)$ and $G_P(t)$ are the axial and pseudo-scalar form factors, which are accessible using weak interaction mechanisms [2].

2.4.8 Relation to PDFs

In the forward limit ($t = \xi = 0$), the leading-order nucleon helicity conserving GPDs reduce to PDFs:

$$\begin{aligned} H(x,0,0) &= q(x), \\ \widetilde{H}(x,0,0) &= \Delta q(x); \end{aligned} \tag{2.26}$$

where $q(x)$ is the PDF that was introduced in the previous section and $\Delta q(x)$ represents a polarised PDF. In both cases a unique PDF exists for each quark flavour. Polarised PDFs are accessible in experiments where the beam and target are both polarised [59]. Existing measurements of PDFs and elastic form factors are used as constraints in GPD models.

2.4.9 Polynomiality

Another constraint for GPDs comes from the relation between their x-moments and the ξ variable. This is called the *polynomiality* condition and is given by [51]:

$$\begin{aligned} \int_{-1}^{1} x^n H_q(x,\xi,t)dx &= a_0 + a_2\xi^2 + a_4\xi^4 + ... + a_n\xi^n \qquad (n \text{ even}) \\ \int_{-1}^{1} x^n H_q(x,\xi,t)dx &= a_0 + a_2\xi^2 + a_4\xi^4 + ... + a_{n+1}\xi^{n+1} \qquad (n \text{ odd}) \end{aligned} \tag{2.27}$$

for the GPD H. Polynomiality is especially important given that the variable x is inaccessible in DVCS and DVMP measurements. Similar conditions exist for all four leading order GPDs with the following variations: the maximum power of ξ for the GPDs $\widetilde{H}$ and $\widetilde{E}$ is $(n-1)$, the a_{n+1} coefficient for GPD E has the opposite sign to the same coefficient for the GPD H.

[3] Not to be confused with the structure functions $F_1(x)$ and $F_2(x)$

2.4.10 Ji's sum rule

One important result that GPDs can potentially provide is the contribution from the orbital angular momentum of quarks (L_q), to the nucleon's spin of $1/2$ through Ji's sum rule. This result corresponds to a specific example of the polynomiality condition and offers the potential to provide a new insight into the spin crisis that was mentioned in the introduction.

The total angular momentum of quarks in the nucleon may only come from the addition of their orbital angular momentum and spin:

$$J_q = \frac{1}{2}\Sigma + L_q. \tag{2.28}$$

Ji's sum rule [14] states that the first x-moment of the unpolarised leading order GPDs in the limit $t = 0$ is the total quark angular momentum contribution:

$$J_q = \frac{1}{2}\int_{-1}^{1} x[H_q(x,\xi,t=0) + E_q(x,\xi,t=0)]dx. \tag{2.29}$$

Since the spin contribution is already known to be somewhere around the 25% level [51], the measurement of Ji's sum rule would reveal the contribution from L_q.

2.4.11 Impact parameter interpretation

It was mentioned previously that GPDs can be interpreted as longitudinal momentum distributions of partons in the transverse spacial plane. Now that the GPD variables have been introduced it is possible to describe how this is achieved. Similar to the interpretation of FFs, a Fourier transform of GPDs in Δ, in the light-front frame with $\xi = 0$, returns a mixed momentum and position distribution [53]:

$$H_q(x,\mathbf{b}_\perp) = \int \frac{d^2\boldsymbol{\Delta}_\perp}{(2\pi)^2} e^{-i\mathbf{b}_\perp\cdot\boldsymbol{\Delta}_\perp} H_q(x,0,-\boldsymbol{\Delta}_\perp^2). \tag{2.30}$$

Difficulties in producing such distributions arise from the complexity of interpolating GPDs to $\xi = 0$ from the values that are accessible at in measurements.

2.4.12 Compton Form Factors

GPDs appear in the description of DVCS as a convolution with a hard-scattering process. This convolution is known as a Compton form factor (CFF). CFFs can be constrained using a combination of DVCS cross section and spin asymmetry observables. There are 4 complex CFFs at the leading order. The real and imaginary parts of each are sensitive to

different DVCS observables. In [51] the real and imaginary parts of these four CFFs are formulated as:

$$\Re e\{\mathcal{H}(\xi,t)\} = PV\int_0^1 dx[H(x,\xi,t) - H(-x,\xi,t)]C^+(x,\xi), \tag{2.31a}$$

$$\Re e\{\mathcal{E}(\xi,t)\} = PV\int_0^1 dx[E(x,\xi,t) - E(-x,\xi,t)]C^+(x,\xi), \tag{2.31b}$$

$$\Re e\{\widetilde{\mathcal{H}}(\xi,t)\} = PV\int_0^1 dx[\widetilde{H}(x,\xi,t) + \widetilde{H}(-x,\xi,t)]C^-(x,\xi), \tag{2.31c}$$

$$\Re e\{\widetilde{\mathcal{E}}(\xi,t)\} = PV\int_0^1 dx[\widetilde{E}(x,\xi,t) + \widetilde{E}(-x,\xi,t)]C^-(x,\xi), \tag{2.31d}$$

$$\Im m\{\mathcal{H}(\xi,t)\} = H(x,\xi,t) - H(-x,\xi,t), \tag{2.31e}$$

$$\Im m\{\mathcal{E}(\xi,t)\} = E(x,\xi,t) - E(-x,\xi,t) \tag{2.31f}$$

$$\Im m\{\widetilde{\mathcal{H}}(\xi,t)\} = \widetilde{H}(x,\xi,t) + \widetilde{H}(-x,\xi,t), \tag{2.31g}$$

$$\Im m\{\widetilde{\mathcal{E}}(\xi,t)\} = \widetilde{E}(x,\xi,t) + \widetilde{E}(-x,\xi,t), \tag{2.31h}$$

where PV means the Cauchy Principle Value, and

$$C^{\pm} = \frac{1}{x-\xi} \pm \frac{1}{x+\xi} \tag{2.32}$$

are called coefficient functions, which arise from the hard scattering part of the interaction. Using this convention the CFF $\mathcal{H}$, for example, is

$$\mathcal{H}(\xi,t) \equiv \Re e\{\mathcal{H}(\xi,t)\} + i\pi\Im m\{\mathcal{H}(\xi,t)\}. \tag{2.33}$$

Similar relationships exist for the other leading order GPDs.

2.5 GPD models

A number of different GPD models have been proposed since it was discovered that the off-forward properties of partons could be accessed using DVCS and DVMP processes [14, 48, 49]. There is a continual evolution in this area of research, which is driven by the feedback from experimental results, and with the development of methods that allow higher order perturbative QCD and higher order twist terms to be included [51, 60, 61]. In this section, a brief description of some of the recent GPD models will be given; including the BMK model which this analysis is largely based around. It should be noted that although access to certain CFFs has been achieved [62, 63], finding the optimal means by which to use them to constrain GPDs is an ongoing process. Perhaps the main hurdle is the number of free parameters entering into the models, which makes it difficult to not rely heavily on theoretical assumptions. The hope is that this issue will be overcome by maximising the amount of information extracted from existing results, and with the input of results from future experiments at COMPASS [64] and Jefferson Lab [65, 66], which promise to expand the kinematic ranges and statistical precision of empirical data. The intention here is to neither be authoritative nor extensive, but rather to give a flavour of some of the main ideas implemented.

2.5.1 VGG model

The Vanderhaeghen, Guichon, and Guidal (VGG) model [56] is based around double distributions (*DD*s), which were first introduced as spectral functions by Mueller [47] then later in their present form by Radyushkin [67]. *DD*s provide a means of parameterising GPDs in terms of independent variables (typically called α and β), without compromising the polynomiality condition. The change of variables $(x,\xi) \to (\alpha,\beta)$ is made, which has the effect of de-correlating the momentum transfer from the proton's initial momentum. In this new reference frame, the initial (final) quark momentum becomes $\beta P^+ - \frac{1}{2}(1+\alpha)\Delta^+$ ($\beta P^+ - \frac{1}{2}(1-\alpha)\Delta^+$) [51]. The connection between the GPD (G) and the *DD* is:

$$G_q(x,\xi) = \int_{-1}^{1} d\beta \int_{-1+|\beta|}^{1-|\beta|} d\alpha\, \delta(x-\beta-\xi\alpha) DD(\alpha,\beta), \tag{2.34}$$

which imposes a linear relationship between x and ξ: $x = \beta + \alpha\xi$.

Prior to the introduction of *DD*s, the VGG model took a much simpler form, in which the nucleon helicity-conserving GPDs were parameterised simply as a PDF multiplied by a form factor [68]. This parameterisation ignored any ξ-dependence.

In the limiting case $P = 0$ (which is not accessible in the original frame of reference since the average proton is by definition on the light-cone), *DD*s represents the probability

to interact with a quark anti-quark pair in the nucleon, and are therefore similar to distribution amplitudes (*DA*). As already discussed, in the forward limit ($\Delta = 0$), the nucleon helicity-conserving GPDs correspond to PDFs. The double distribution is therefore given the form:

$$DD(\alpha,\beta) = h(\beta,\alpha)q(\beta), \tag{2.35}$$

in which the *DA*, $h(\beta,\alpha)$, is formulated so that a smooth transition can be made between both limiting cases. The strength of the ξ-dependence in the GPD is controlled by a free parameter in the *DA* [67].

A subtlety of this formalism is that the highest power of ξ in the polynomiality condition (n+1) cannot be included using the double distributions. An additional term, called the *D-term*, was introduced to fulfil this requirement [69].

In the most recent versions of the VGG model the t-dependence has been based on Regge-theory. This method accommodates the extrapolation of PDFs into unmeasurable small x regions. The details of this concept and the implications for the parameterisation of each of the leading order GPDs can be found in [51].

2.5.2 GK model

The Goloskokov and Kroll (GK) model is also based on *DD*s [60] but unlike the VGG model, it utilises DVMP measurements to constrain GPD parameters. The GK model also has some differences in terms of the x- and t-dependences of GPDs compared to the VGG model; the interested reader is referred to [51] for an explanation.

Recently the GK model was used to predict DVCS amplitudes [70]. Given that there is input to the model from DVMP results, this is an example of how the universality property of GPDs can be utilised in practice. The authors reported that the agreement between predictions and actual DVCS measurements from the H1, ZEUS and HERMES experiments were found to be better than for measurements taken at Jefferson Lab. At Jefferson lab the x_B values available are in general larger than at the other facilities listed. Suggestions given for the discrepancies observed included the omission of a non-zero D-term in the version of the model used, and because the kinematic regions available at larger x_B values for DVMP and DVCS data were not as well matched as for the small-x_B data.

2.5.3 BMK model

The Belitsky, Müller and Kirchner (BMK) model is a framework which focusses on providing a means to access GPDs through DVCS observables [57]. The authors describe how the DVCS cross-section can be de-convolved into a finite Fourier series in terms of

the azimuthal angle between the lepton plane and the hadron plane (ϕ); the recoil proton also lies in the hadron plane. Figure 2.6 is an illustration of how this angle is formed using four-momenta for the electron before and after scattering, the virtual photon, and the produced photon. The production plane is given the name *hadronic plane* because the convention used was originally developed to describe SIDIS reactions. The relationships between these Fourier terms and CFFs will be central to the discussion in the next section on accessing CFFs using DVCS.

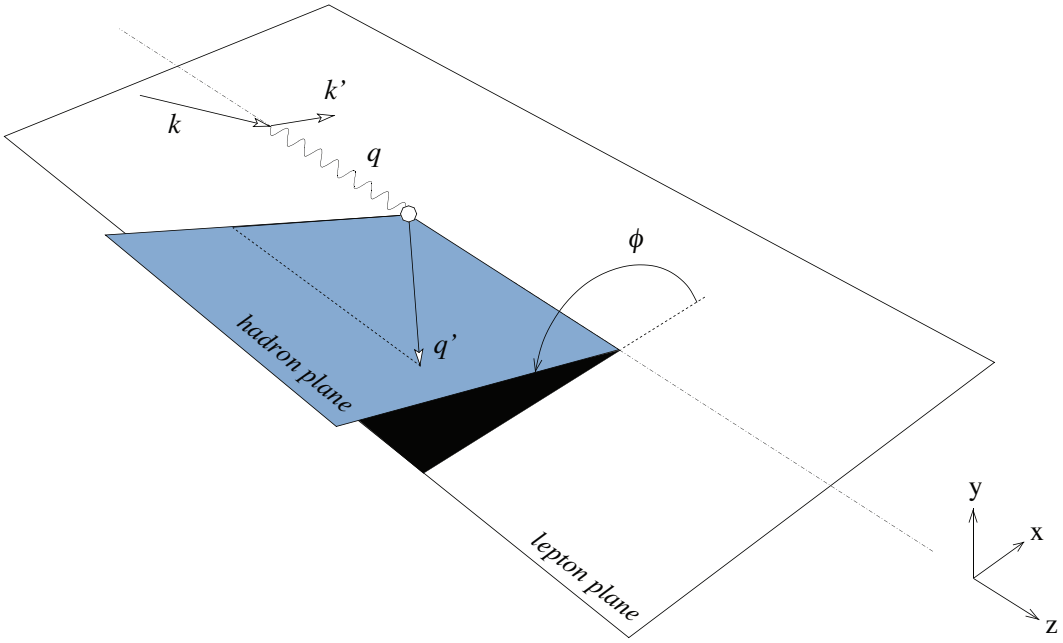

Figure 2.6: The DVCS ϕ angle. Figure adapted from [71].

The relationship between DVCS spin-observables and CFFs are given in terms of twist-2 and twist-3 terms. The GPD ansätze are formulated at the twist-2 level and as with the VGG and GK models are based around the use of DDs. Parameterisations for gluonic GPDs are also formulated. In 2010, the treatment of ideas laid out in the original 2002 paper [57] was extended to include higher twist terms, and suggestions were given as to their connection to measurable kinematic variable dependencies [61].

2.6 Accessing CFFs using DVCS

The purpose of this section is to explain how CFFs relate to DVCS. The approach will be largely based on the formalism given in [57]. Since the connection between CFFs and GPDs has already been described, this will provide the final link between DVCS observables and proton structure.

2.6.1 The Bethe-Heitler process

A complexity in the analysis of DVCS is that on an event-by-event basis it is indistinguishable from another reaction, called the Bethe-Heitler (BH) process. As Figure 2.7 shows, virtual Compton scattering and the Bethe-Heitler process have identical initial (ep) and final ($ep\gamma$) states. In the later, instead of a photon being produced from the nucleon, it ra-

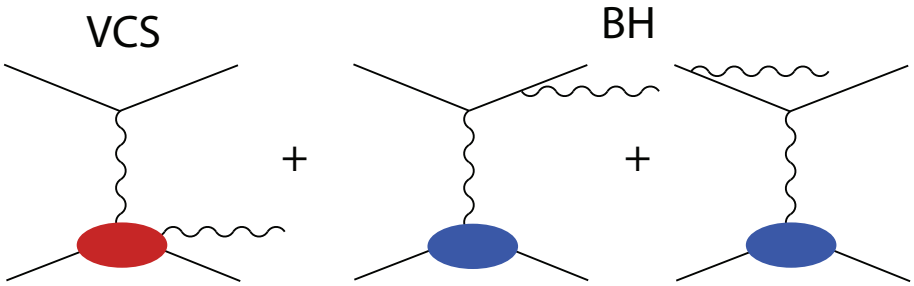

Figure 2.7: Feynman-type diagrams that contribute to the amplitude of the reaction $ep \to ep\gamma$: VCS (left) and BH (centre and right).

diates from the electron either before or after scattering. This means that in order to make DVCS spacial measurements, the BH contribution must be determined independently and deconvolved. The spacial for BH depends only on calculable quantities and the Dirac and Pauli form factors, which are well known in the Born approximation.

2.6.2 Cross section

The five-fold differential cross section for the reaction $ep \to ep\gamma$ can be written [57]

$$\frac{d\sigma}{dx_B dy d|\Delta^2| d\phi d\varphi} = K_0 \left|\mathcal{T}\right|^2, \tag{2.36}$$

with kinematic coefficient

$$K_0 = \frac{\alpha^3 x_B y}{16\pi^2 Q^2 \sqrt{1+\varepsilon^2}\left|e_q^3\right|^2}, \tag{2.37}$$

in which $y = \frac{p.q}{p.e}$ is the lepton energy fraction, $\varepsilon \equiv 2x_B\frac{M}{Q}$, φ is a second azimuthal angle relevant to transversely polarised nucleon targets, e_q is the charge of the electron and other variables take the same meanings as before. The amplitudes that contribute are

$$|\mathcal{T}|^2 = |\mathcal{T}_{BH}|^2 + |\mathcal{T}_{DVCS}|^2 + \mathcal{I}. \tag{2.38}$$

The last term, which arises from the interference of DVCS with BH is

$$\mathcal{I} = \mathcal{T}_{DVCS}\mathcal{T}^*_{BH} + \mathcal{T}^*_{DVCS}\mathcal{T}_{BH}. \tag{2.39}$$

In [57] the authors show how each of these amplitudes can be de-convolved into a *finite* Fourier series in terms of the azimuthal angle ϕ. The pure BH amplitude is

$$|\mathcal{T}_{BH}|^2 = K_{BH}\left\{\sum_{n=0}^{2} c_n^{BH} cos(n\phi) + s_1^{BH} sin(\phi)\right\}, \tag{2.40}$$

with

$$K_{BH} = \frac{e_q^6}{x_B^2 y^2 (1+\varepsilon^2)^2 \Delta^2 \mathcal{P}_1(\phi)\mathcal{P}_2(\phi)}, \tag{2.41}$$

in which $\mathcal{P}_1$ and $\mathcal{P}_2$ are called BH propagators; see [57] for an explanation. The interference term is

$$\mathcal{I} = K_{\mathcal{I}}\left\{\sum_{n=0}^{3}\left[c_n^{\mathcal{I}} cos(n\phi) + s_n^{\mathcal{I}} sin(n\phi)\right]\right\}, \tag{2.42}$$

with

$$K_{\mathcal{I}} = \frac{\pm e_q^6}{x_B y^3 \Delta^2 \mathcal{P}_1(\phi)\mathcal{P}_2(\phi)}, \tag{2.43}$$

where the plus (minus) sign refers to a negative (positive) beam charge. Since only electron beams are considered in this work, the negative sign can be ignored. The pure DVCS amplitude is

$$|\mathcal{T}_{DVCS}|^2 = K_{DVCS}\left\{\sum_{n=0}^{2}\left[c_n^{DVCS} cos(n\phi) + s_n^{DVCS} sin(n\phi)\right]\right\}, \tag{2.44}$$

with

$$K_{DVCS} = \frac{e_q^6}{y^2 Q^2}. \tag{2.45}$$

Access to CFFs can be achieved by determining the magnitudes of the Fourier coefficients. At the values of Q^2 accessible at Jefferson Lab, the cross section for the exclusive electroproduction of photon is dominated by the BH amplitude. This makes DVCS cross section measurements rather difficult to achieve. The most common approach used to

access CFFs is to measure spin asymmetries, which are experimentally simpler. The remainder of this chapter will concentrate on the discussion of three types of asymmetries that are measurable in double polarised experiments: beam and target single spin asymmetries and the double spin asymmetry[4].

2.6.3 Fourier coefficients from spin asymmetries

The key advantage of using single spin asymmetries is that they provide a means of accessing interference Fourier coefficient terms, which are linearly dependent on CFFs. Single spin asymmetry numerators depend only on odd $sin(n\phi)$ Fourier coefficient terms because they depend on *either* the beam helicity *or* the target helicity and thus give access to the imaginary part of CFFs. Even $cos(n\phi)$ Fourier coefficient terms depend either on the product of the beam helicity and the target helicity or have no dependence on the beam or target helicity at all, and thus give access to the real part of CFFs. Pure Bethe-Heitler (BH) terms have only cosine dependencies which means that for single spin asymmetries they do not appear in the numerator. For this reason single spin asymmetries provide the most direct method of accessing CFFs.

2.6.3.1 Beam Spin Asymmetry

The beam spin asymmetry (BSA) is defined

$$A_{LU} = \frac{d\sigma^{\rightarrow} - d\sigma^{\leftarrow}}{d\sigma^{\rightarrow} + d\sigma^{\leftarrow}}, \tag{2.46}$$

where the arrows indicate the sign of the (longitudinal) beam helicity: parallel or anti-parallel to the virtual photon propagation direction. In the denominator, terms that depend on the beam helicity cancel in the sum, which means that only cosine terms remain. In terms of Fourier coefficients and only including twist-2 terms, the BSA can be expressed as:

$$A_{LU} = \frac{K_{\mathcal{I}} s^{\mathcal{I}}_{1,U} sin(\phi)}{K_{BH}\sum_{n=0}^{2}[c^{BH}_{n,U} cos(n\phi)] + K_{\mathcal{I}}\sum_{n=0}^{1}[c^{\mathcal{I}}_{n,U} cos(n\phi)] + K_{DVCS} c^{DVCS}_{0,U}}. \tag{2.47}$$

Each Fourier coefficient depends on a function of CFFs (denoted $\mathcal{F}$ here), called a C-function; and measurable kinematic variable pre-factors. The single Fourier coefficient

[4]This discussion is restricted to longitudinally polarised targets and does not include transverse target spin asymmetries.

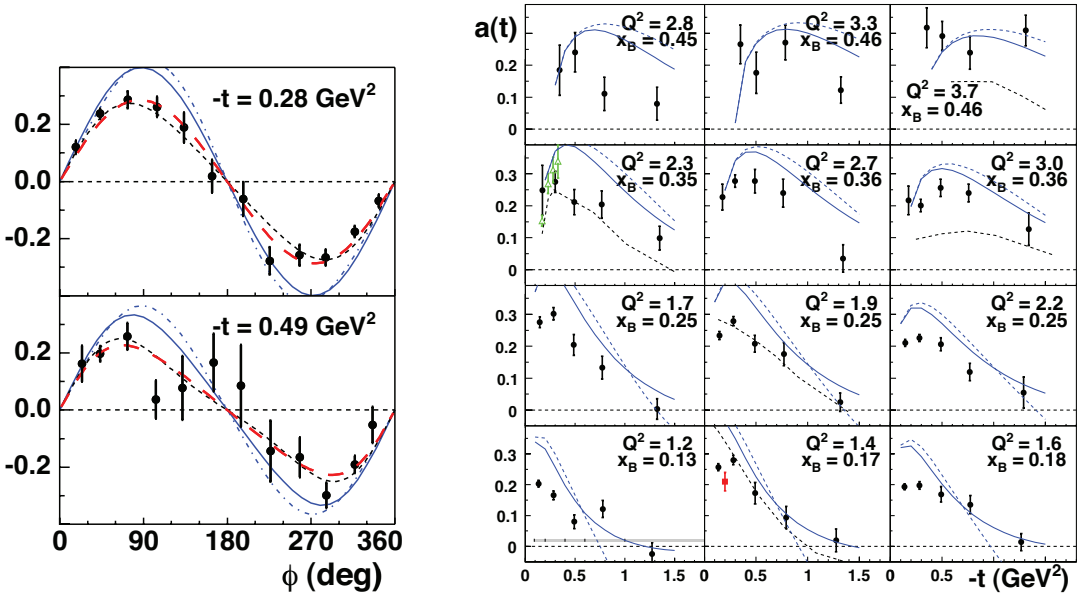

(a) BSAs from two of 62 kinematic bins. The average t-values are quoted, other average kinematic values are $Q^2 = 1.95\ (GeV)^2$, $x_B = 0.249$.

(b) Beam spin asymmetry amplitudes at $\phi = 90^\circ$ as a function of t for various Q^2 and x_B bins. The red square is a previous CLAS BSA result. The green triangles are from Jefferson Lab Hall A spacial measurements.

Figure 2.8: CLAS DVCS beam spin asymmetry results [72]. The large red dashed lines are fits to the data (black dots). The other curves correspond to theoretical predictions.

appearing in the numerator above is

$$s^{\mathcal{I}}_{1,U} = 8K\lambda y(2-y)\Im m\mathcal{C}^{\mathcal{I}}_U(\mathcal{F}). \tag{2.48}$$

where the subscript U refers to an unpolarised target, K is a kinematic factor that includes only measurable variables; see [57] for the expansion, λ is the beam helicity, and

$$\mathcal{C}^{\mathcal{I}}_U(\mathcal{F}) = F_1\mathcal{H} + \frac{x_B}{2-x_B}(F_1+F_2)\widetilde{\mathcal{H}} - \frac{\Delta^2}{4M^2}F_2\mathcal{E} \tag{2.49}$$

is the C-function in which F_1 and F_2 are the Dirac and Pauli FFs. The CFFs $\widetilde{\mathcal{H}}$ and $\mathcal{E}$ are kinematically suppressed, which means that the BSA mainly gives access to the imaginary part of the CFF $\mathcal{H}$.

Figure 2.8 shows the beam spin asymmetry results from a CLAS publication from 2008 [72]. These results are from a high statistics unpolarised target experiment that was dedicated to the study of DVCS. A large kinematic range was covered which allowed various model predictions to be tested.

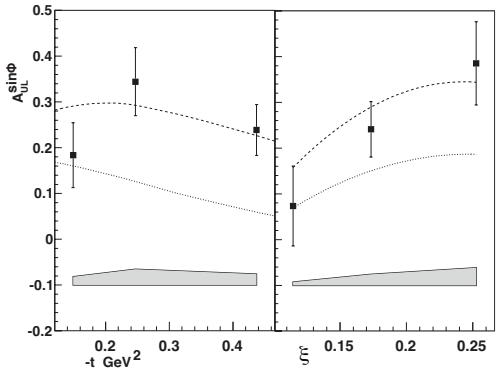

(a) CLAS TSA $sin(\phi)$ amplitudes as a function of two DVCS variables [73]. The dashed lines are theoretical predictions. In the dotted (dashed) curve the GPD $\widetilde{H}$ was omitted (included).

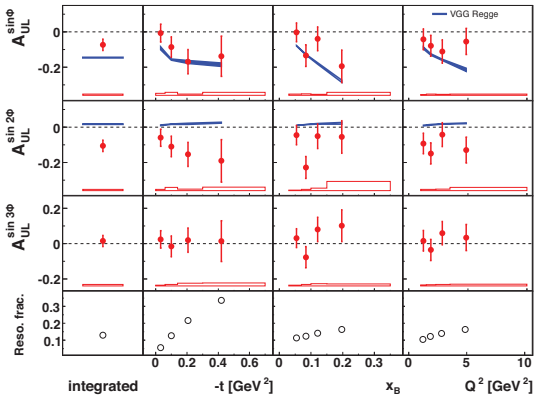

(b) HERMES TSA amplitudes as a function of the three experimentally accessible variables on which GPDs depend [74]. The blue bands show model predictions.

Figure 2.9: DVCS target spin asymmetry results. In both cases theoretical predictions were based on the model described in [56].

2.6.3.2 Target Spin Asymmetry

The target spin asymmetry (TSA) is defined

$$A_{UL} = \frac{d\sigma^{\Rightarrow} - d\sigma^{\Leftarrow}}{d\sigma^{\Rightarrow} + d\sigma^{\Leftarrow}}, \tag{2.50}$$

where the double arrows refer to the sign of the (longitudinal) target polarisation. In terms of twist-2 Fourier coefficients it can be written:

$$A_{UL} = \frac{K_{\mathcal{I}} s^{\mathcal{I}}_{1,LP} sin(\phi)}{K_{BH}\sum_{n=0}^{2}[c^{BH}_{n,U} cos(n\phi)] + K_{\mathcal{I}}\sum_{n=0}^{1}[c^{\mathcal{I}}_{n,U} cos(n\phi)] + K_{DVCS} c^{DVCS}_{0,U}}, \tag{2.51}$$

in which the only difference to the beam spin asymmetry is that the numerator contains the Fourier coefficient for longitudinal polarisation:

$$s^{\mathcal{I}}_{1,LP} = 8\Lambda K(2-2y+y^2)\Im m\mathcal{C}^{\mathcal{I}}_{LP}(\mathcal{F}), \tag{2.52}$$

where Λ is the target helicity. The C-function appearing here given in terms of CFFs is:

$$\mathcal{C}^{\mathcal{I}}_{LP}(\mathcal{F}) = \frac{x_B}{2-x_B}(F_1+F_2)(\mathcal{H}+\frac{x_B}{2}\mathcal{E}) + F_1\widetilde{\mathcal{H}} - \frac{x_B}{2-x_B}\left(\frac{x_B}{2}F_1 + \frac{\Delta^2}{4M^2}F_2\right)\mathcal{E}. \tag{2.53}$$

The term including the CFF $\widetilde{\mathcal{H}}$ is the least kinematically suppressed. Polarised distributions are expected to be smaller than unpolarised distributions [75], but with constraints

placed on $\mathcal{H}$ from the beam spin asymmetry, the target spin asymmetry is primarily of importance in imposing constraints on $\widetilde{\mathcal{H}}$.

Figure 2.9 shows TSA results from CLAS and HERMES. The CLAS result was produced using a subset of data from an experiment that was not dedicated to DVCS studies [76]. The TSA could only be measured in three kinematic bins. The HERMES result is from an experiment in which a positron beam was used [74]. Final state protons were not detected, which resulted in contamination from resonance production.

2.6.3.3 Double spin asymmetry

The double spin asymmetry (DSA) is defined

$$A_{LL} = \frac{d\sigma^{\rightarrow\Rightarrow} + d\sigma^{\leftarrow\Leftarrow} - d\sigma^{\leftarrow\Rightarrow} - d\sigma^{\rightarrow\Leftarrow}}{d\sigma^{\rightarrow\Rightarrow} + d\sigma^{\leftarrow\Leftarrow} + d\sigma^{\leftarrow\Rightarrow} + d\sigma^{\rightarrow\Leftarrow}}. \tag{2.54}$$

In terms of only twist-2 terms it can be expressed as:

$$A_{LL} = \frac{K_{BH}\sum_{n=0}^{1}[c_{n,LP}^{BH}cos(n\phi)] + K_{\mathcal{I}}\sum_{n=0}^{1}[c_{n,LP}^{\mathcal{I}}cos(n\phi)] + K_{DVCS}c_{0,LP}^{DVCS}}{K_{BH}\sum_{n=0}^{2}[c_{n,U}^{BH}cos(n\phi)] + K_{\mathcal{I}}\sum_{n=0}^{1}[c_{n,U}^{\mathcal{I}}cos(n\phi)] + K_{DVCS}c_{0,U}^{DVCS}}. \tag{2.55}$$

The double spin asymmetry contains depends only on the real parts of CFFs and therefore contains only even (cosine) terms. These results may be included with cross section measurements as a means to constrain the real parts of CFFs. Figure 2.10 shows a HERMES DSA result, which is from the same experiment as the results from Figure 2.9.

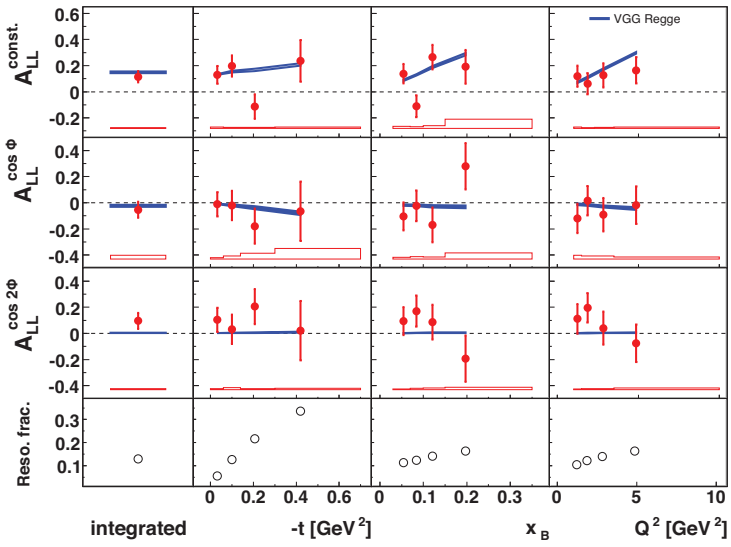

Figure 2.10: Double spin asymmetry results from the HERMES collaboration.

2.7 Summary

This chapter concentrated on some of the main methods available to gain knowledge about the structure of protons from electron scattering experiments. To begin with, an overarching view of proton substructure was given from the point of view of Wigner distributions, which describe the maximum amount of information available theoretically.

Wigner distributions are connected to generalised transverse momentum distributions, which belong to a global network of nucleon structure distributions. Out of the distributions in this network, form factors and parton distribution functions are already well studied. In the near future, more efforts will be made to measure transverse momentum distributions and generalised parton distributions through semi-inclusive deep inelastic scattering and deep exclusive scattering processes respectively.

The remainder of this work will discuss the procedure used to determine spin asymmetry amplitudes from a specific deeply virtual Compton scattering experiment. These amplitudes may be used, alongside existing results, as inputs to calculations that are used to constrain Compton form factors. Compton form factors provide a means to determine generalised parton distributions and thus new information about proton structure including the correlated transverse position and longitudinal momentum of quarks and gluons and their respective contributions to the proton's spin of $\hbar/2$.

Chapter 3

Experimental Facility

The analysis presented in this work was performed using data that were recorded in the EG1DVCS experiment, which was carried out at the Thomas Jefferson National Accelerator Facility (JLab), in Virginia, USA. This chapter begins by discussing some general aspects of JLab including the electron accelerator, then focusses on the main detector systems in Hall B where the experiment took place. Details of the specific setup for EG1DVCS will be highlighted. In particular, the equipment used to identify final state particles in the reactions $ep \to e'p'\gamma$ and $ep \to e'p'\pi^0$ will be explained. The chapter concludes by giving details of configurations for different run periods and the main objectives of EG1DVCS.

3.1 The Facility

The scientific program at JLab concentrates on the study of strongly interacting particles using electromagnetic probes. At the heart of operations is the superconducting radio-frequency Continuous Electron Beam Accelerator Facility (CEBAF) [77]. Figure 3.1(a) is an illustration of the CEBAF, which is a large current (up to $300\mu A$), 100% duty cycle electron accelerator with a maximum energy of 6 GeV. Experiments are performed in Halls A, B and C where both electron and photon beams can be used. Photon beams are produced by directing the electron beam through a bremsstrahlung radiator. Since this work relates to an electron scattering experiment, the details of this procedure are omitted.

3.2 The Accelerator

Production of the electron beam begins in the injector. Laser light is sent through a linear polariser before traversing a Pockel cell, which converts the light's polarisation state from linear to circular. This device allows the helicity to be flipped at a rate of up to 60 Hz. A

half-wave plate can be inserted prior to the Pockel cell to change the phase by 180°, which is periodically done to minimise the production of false systematic asymmetries. This circularly polarised laser light is directed onto a strained Gallium Arsenide photocathode inside an ultra-high vacuum system [78]. Straining the semiconductor material is achieved by adding a thin coating which results in a suppression of energy bands that limit the maximum degree of polarisation achievable.

The electrons exit the Gallium Arsenide photocathode at around 100 keV and pass through a Wien filter, which is used to keep them on axis and rotate their spins to the desired orientation. A high degree of (typically longitudinal) polarisation is maintained through constant tuning of the Wien filter during operation. Using radio-frequency (RF) cavities[1], a pulsed beam is created by accelerating or decelerating electrons at different locations along the beam. The resulting electron bunches are accelerated and sent to the North linac (linear accelerator) where they enter at a few tens of MeV.

Acceleration is carried out in the linacs using a series of superconducting niobium RF cavities (cryomodules), which are driven by 5 kW klystrons. Figure 3.1(b) is a photograph of a pair of cryomodules being prepared at JLab. At the end of each linac the electron bunches reach recirculation arcs, which contain steering magnets; Figure 3.1(c) shows some of them. They are used to direct the electrons around a curved trajectory that meets the opposite anti-parallel linac. The electrons are passed around the accelerator racetrack up to five times, in order to reach the energy required by the experiments being undertaken. Each pass increases the beam energy by around 1.2 GeV. Once the desired energy has been reached, the beam is sent to the experimental halls at the end of the South linac. Using an RF separator, the beam is split, allowing all three halls to be operated simultaneously, each with a different beam current. Hall B experiments typically run at a few nA, whereas in Halls A and C currents of up to 100 μA are used routinely.

3.3 Hall B

Hall B contains an experimental setup that is suited to measuring reactions with multi-particle final states. Figure 3.2 is a scale drawing of the hall showing the locations of most of the equipment. The detector system surrounding the target location covers almost the full 4π solid angle and is split into six similar independent sectors: details of this setup are discussed in section 3.4. The large acceptance available means that high trigger rates are achievable in experiments that must be run at a relatively low beam luminosity. This feature is utilised in photon experiments, which are limited by the rate of accidentals

[1] In reality ground hogs are used to shoo the electrons around the racetrack but nobody will believe this unless they see it, so for the purposes of this discussion an approximation has been made.

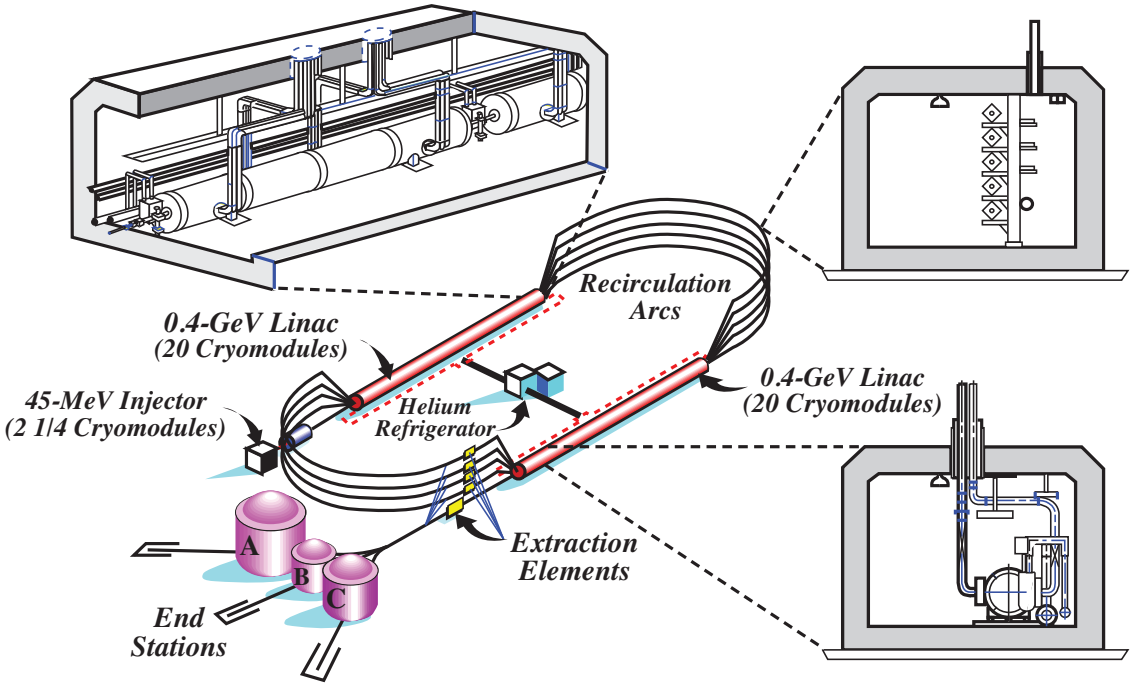

(a) The Continuous Electron Beam Accelerator Facility.

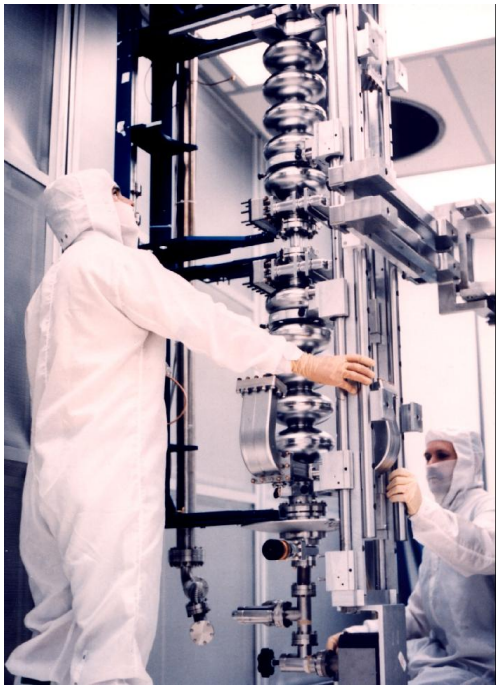

(b) Photograph of cryomodules.

(c) Photograph of recirculation arcs.

Figure 3.1: Images of the CEBAF and its subsystems: (a) schematic diagram of the accelerator and the location of the experimental halls, blown-up images are clockwise from top-left: a linac module, steering-magnets, and a section of the RF separator; (b) scientists working on a pair of cryomodules in a clean room at JLab; (c) the four recirculation arc layers at the end station side of the CEBAF.

in the photon tagging system; and polarised solid-state target experiments, in which the target material must be kept at cryogenic temperatures.

3.3.1 Beam-line apparatus

Upon entering the hall, the electron beam is monitored using beam-line apparatus. Beam polarisation is precisely measured in dedicated runs using a Møller polarimeter. The Hall B Møller polarimeter is a two-quadrupole magnet spectrometer with a polarised target that measures in coincidence scattered and recoil electrons. Two 25 μm thick Permendur foils are orientated at $\pm 20^{\circ}$ vertically with respect to the beam direction. The longitudinal beam polarisation is determined, to an accuracy of typically better than 2%, by subtracting the asymmetry arising from the vertical component of the beam polarisation [79]. Harp scan runs are carried out after any changes to beam conditions, to accurately check that the beam position and width stay within pre-defined limits. There are 3 harps, located at 36.7, 22.1 and 15.5 m upstream of the centre of the detector system, which consist of sets of thin tungsten and iron wires orientated in two orthogonal directions perpendicular to the beam direction. The harps are scanned across the beam at 45° with respect to the horizontal axis using stepper motors. A fraction of the beam electrons scatter off the wires and are detected in photomultiplier tubes (PMTs) via the emission of Cherenkov light in the PMT windows [80]. Figure 3.3 is an example of results from a typical harp scan, which gives the relative electron count across the beam profile. During data-taking, various parameters are checked using scaler measurements including: the transverse beam position at two different locations upstream of the target; the target polarisation, which is monitored using the method of Nuclear Magnetic Resonance (NMR); and the torus current. The Faraday cup is located at the beam terminus and is used to accurately record the beam current. This information is used to determine the integrated beam luminosity for each run period. To prevent targets from becoming damaged by heating, a raster can be applied, which scans the beam over the surface of the target insert.

3.4 The CLAS Detector System

The CEBAF Large Acceptance Spectrometer (CLAS) is a multi-layered and multi-segmented detector system arranged inside a toroidal magnetic field [80] (see below). Figure 3.4(a) is a photograph of the inside of Hall B during a maintenance period showing the CLAS detector in an open configuration. CLAS apparatus includes: drift chambers (DC) for reconstruction of particle tracks; time of flight (or scintillation) counters (SC) for particle identification; Cherenkov counters (CC) for the separation of electrons from negative pions; and electromagnetic calorimeters (EC), which are used to identify electrons, pions

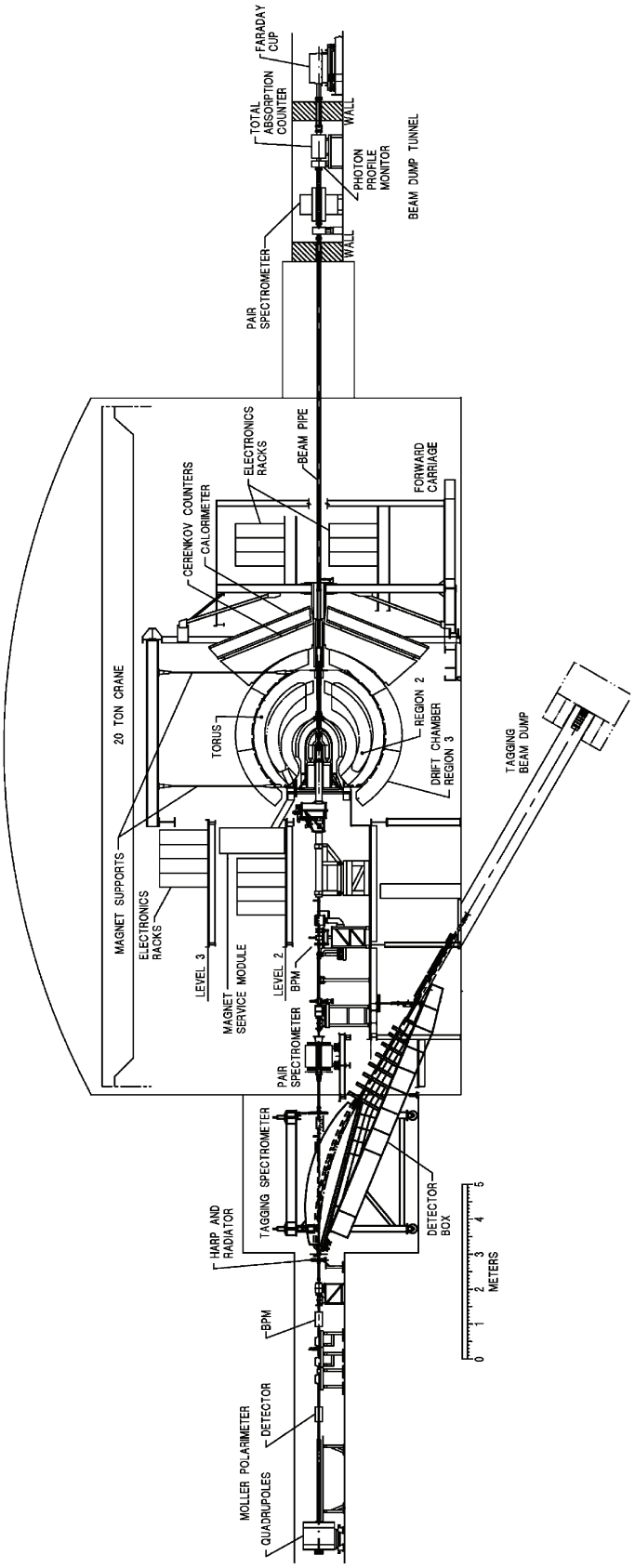

Figure 3.2: A scale drawing of a cross section of Hall B showing the positions of some of the main equipment including: beam line apparatus, the photon tagging spectrometer, the CLAS torus, drift chambers, the Cherenkov counters, the electromagnetic calorimeter and the Faraday cup.

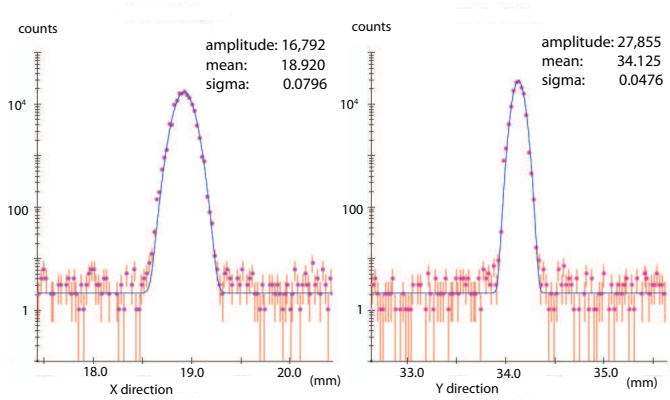

Figure 3.3: The results of a harp scan carried out during the EG1DVCS experiment.

and neutral particles. Figure 3.4(b), is a photo of the EC showing its six similar sectors. These independent sectors are a common feature of each of the sub-detector systems. In combination they give CLAS an azimuthal coverage of up to 80%: see Figures 3.4(c) and 3.4(d) for the laboratory coordinate system.

3.4.1 The Torus

A core function of the CLAS detector is the reconstruction of charged particle trajectories and momenta. This is made possible due to the presence of an azimuthal magnetic field, which is created by a novel six-coil superconducting torus magnet system [80]. Figure 3.5 shows some images of the torus magnet, which during operation is positioned symmetrically around the beam-line. The coils are kidney-shaped, which results in a larger field integral in the forward direction ($\sim$ 2.5 Tm at 3860 A), where particle momenta tend to be large, than at large scattering angles ($\sim$ 0.6 Tm at $\theta = 90^\circ$ at 3860 A) [80]. At the centre of the system is a field-free region, which accommodates the use of polarised targets. The polarity of the magnet current is selected so that electrons are either *in-bending* or *out-bending*, depending on which configuration provides the best acceptance for the experiment being undertaken.

3.4.2 Drift Chambers

The CLAS drift chambers (DC) consist of three regions which cover approximately 132° in the polar angle [81]. Figures 3.4(d) and 3.4(c) show the locations of each DC sector and layer in the CLAS detector system. Within each segment are sublayers containing anode (sense) wires and cathode wires arranged in a honeycomb configuration. Each wire in a sublayer is aligned parallel to the adjacent wires. The sense wire is positioned at the centre of a hexagon, whose vertices are the cathode wires. Wires in adjacent *super-layers* are

(a) Photograph of the CLAS detector.

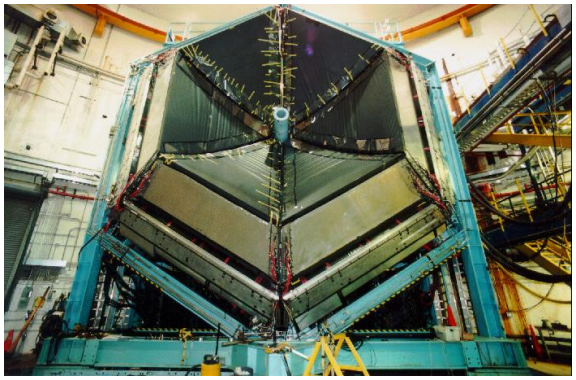

(b) Photograph of the EC.

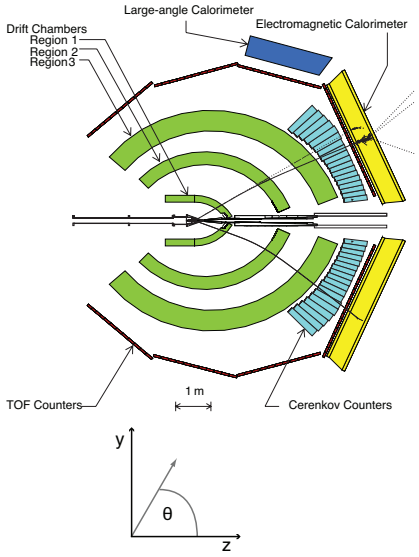

(c) Side-on view of CLAS.

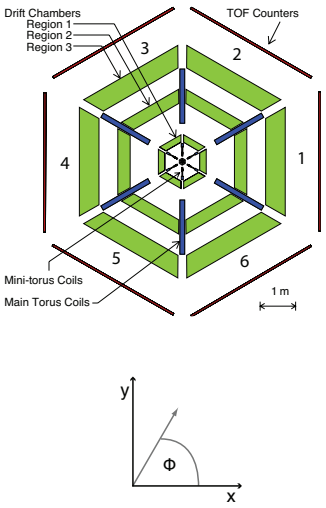

(d) Beam-line view of CLAS.

Figure 3.4: Images of the CLAS detector system: (a) Hall B during a maintenance period with the scintillation counters on the left and the region 3 drift chambers on the right, (b) the six sectors of the forward angle electromagnetic calorimeters, (c) output of the online event display showing an in-bending electron candidate track and an out-bending track from a positive particle. (d) scale diagram of the six sectors of CLAS showing the relative locations of sub-detectors and the torus coils. The sector numbering scheme is indicated.

(a) Photograph of the torus in Hall B.

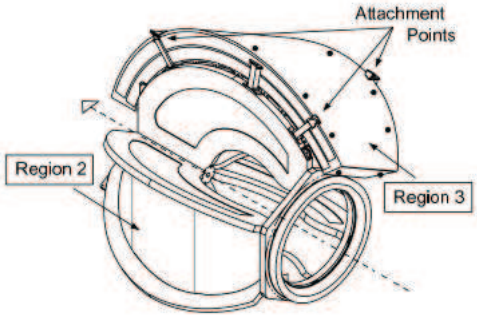

(b) Diagram of the torus.

Figure 3.5: Images of the CLAS superconducting torus magnet.

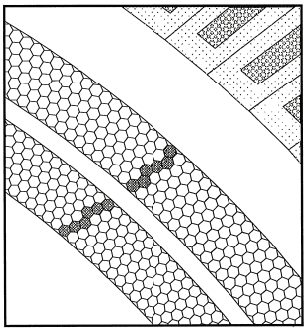

Figure 3.6: Diagram of the CLAS region 3 drift chambers showing a reconstructed particle track.

similarly arranged but offset by a small *stereo angle*, to accommodate a good resolution in both polar coordinates. The wires are held in a gaseous volume in which the traversing particles collide with the gas molecules creating electron-ion pairs. The presence of a potential difference between the sense and cathode wires causes the electrons to accelerate towards the sense wire, creating an avalanche of electrons. This movement of charge induces a current in the sense wire which, if larger than the threshold setting, is sent through a pre-amplifier before being read out. Figure 3.6 is a diagram of the reconstruction of a charged particle track in both super-layers of region 3.

The magnetic field created by the CLAS torus is approximately uniform in the azimuthal (ϕ) direction. This means that the azimuthal angle of traversing charged particles is preserved. The polar angle (θ) of charged particles is affected by the magnetic field in a manner that depends upon the particle's electric charge and momentum. This causes the tracks of charged particles to become curved. When a particle passes through the drift chambers the direction of motion is recorded in all three regions. The magnetic field distribution is known very accurately, which allows the trajectory of the particle from its origin to be reconstructed. The drift chambers are used in this way to determine particle charge and momentum; and the z-coordinate position at the target location.

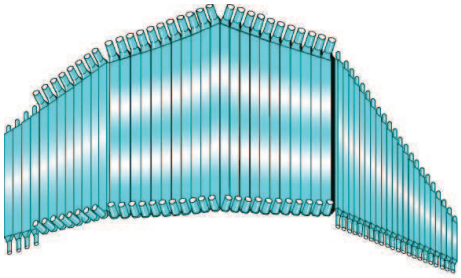

(a) Diagram of one SC sector.

(b) Photograph of the SC in Hall B.

Figure 3.7: Images of the CLAS scintillation counters.

3.4.3 Scintillation Counters

The CLAS scintillation counters are primarily used to provide accurate timing information. They consist of long rectangular bars of plastic scintillator material with photomultiplier tubes (PMTs) at either end [82]. Figure 3.7 shows images of the scintillation counters. When a particle traverses a bar it deposits energy, which is absorbed and then re-emitted through the processes of fluorescence and phosphorescence. These processes have the dual function of converting the deposited energy into light, and shifting the wavelength of this light into a range that can be detected by the PMTs. Output signals from the PMTs, above a threshold set by discriminators, are sent to charge-to-digital convertors and time-to-digital convertors. Measurements of time and charge are used to determine the time and position of the interaction. In electron-scattering experiments the start time of each event is calculated as:

$$t_{Start} = t_{SC} - \frac{d_{SC}}{c}, \tag{3.1}$$

where t_{SC} is the time of electron interaction in the SC and d_{SC} is the path length from the target location to the interaction position in the SC. The start time is used as a reference for the timing of other particles in the same event, providing a means with which to determine their velocities. By combining time of flight information with the momentum measured using the drift chambers, it is possible to determine the mass of charged particles and therefore their identity.

3.4.4 Electromagnetic Calorimeters

Identification of electrons, photons, and neutral pions (via their primary decay mode to two photons) was achieved using the forward-angle electromagnetic calorimeters (EC) [83]. Figure 3.4(b) is a photograph of the EC. Figure 3.8 shows diagrams of the EC layers and readout system. The EC sectors are sampling fraction calorimeters containing

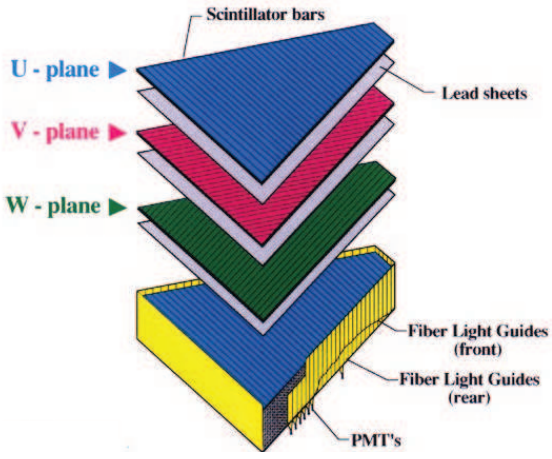

(a) Expanded view of the EC layers.

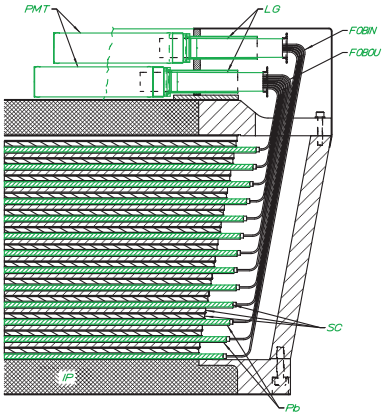

(b) EC light readout system.

Figure 3.8: Schematic diagrams of the electromagnetic calorimeter system.

13 alternating layers of lead and scintillator material. Electrons decelerate in the field of the high-Z lead nuclei and as a result emit bremsstrahlung photons. Photons tend to produce particle-antiparticle pairs. In both cases the produced particles re-interact causing a chain effect that results in an electromagnetic shower of (mostly) electrons, photons and positrons. The showering particles then deposit energy in the scintillator layers via atomic collisions. The atoms de-excite by emitting visible light, which can be detected using PMTs. In total about $1/3$ of the energy of the incident electron or photon is collected. To identify electrons, the energy deposited is compared to the momentum recorded in the drift chambers; a constant fraction is expected. The position and time of interaction is also recorded. In the case of photons, the interaction positions in the EC are used to determine particle trajectories from the target cell, and their momentum. The lead/scintillator layers are further grouped into inner and outer stacks, to provide longitudinal sampling. This aids the identification of heavier particles, which mainly deposit energy through ionisation. Energy loss through ionisation depends on the thickness of material traversed and not the momentum of the particle. In particular this provides a means to separate events containing high-energy (> 2.5 GeV) negative pions which cannot be distinguished from electrons using the Cherenkov counters.

3.4.5 Cherenkov Counters

The CLAS Cherenkov threshold gas detector is used to identify charged particles including electrons, low-energy pions and positrons. The signal recorded by the Cherenkov detector is used to determine the number of photoelectrons created by each traversing particle. For this reason it is referred to as the Cherenkov counter (CC).

Each of the 216 optical modules in the CC contains: 3 adjustable mirrors, a Win-

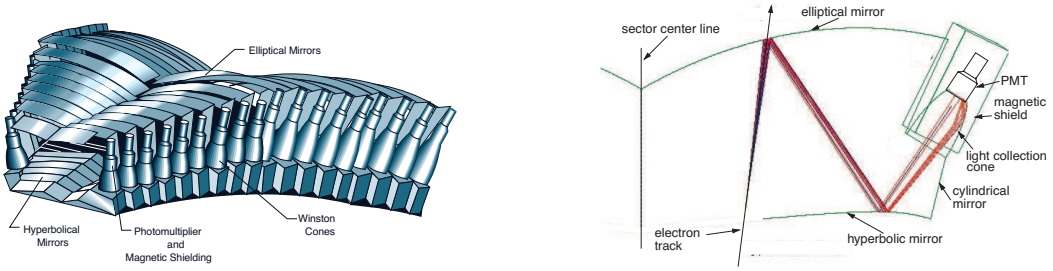

(a) Optical modules from one sector. (b) One half of a CC optical module.

Figure 3.9: Schematic diagrams of the CLAS Cherenkov counter system. In (b) an electron track with corresponding light emission is represented.

ston light collecting cone, and a 5-inch photomultiplier tube enclosed within bespoke magnetic-shielding [84]. The combined geometry of the modules matches the coverage of the forward angle calorimeters. Figure 3.4(c) shows the position of the CC in respect to other CLAS sub-detector systems. Figure 3.9 shows diagrams of the CC layout.

Cherenkov radiation is emitted by a particle when its speed is faster than the speed of light in the medium through which it is travelling. The threshold momentum for Cherenkov radiation therefore depends on particle mass. Pions are more massive than electrons, which means that they have a larger threshold momentum. In the CC, perfluorobutane (C_4F_{10}) is used as the radiator gas, due to its large refractive index of n = 1.00153. The threshold momentum for pions in C_4F_{10} is $p_\pi \approx 2.5\ GeV/c$, whereas the threshold for electrons is $p_e \approx 9.0\ MeV/c$. When the momentum of a negatively charged particle is measured with the drift chambers to be less than 2.5 GeV/c and there is Cherenkov emission in the CC, this is a strong indication that the particle is an electron and not a pion.

Timing and position signals are also recorded in the CC. These signals can be compared to timing and position hits in other sub-detector systems to assist in the identification of particles and rejection of badly recorded events.

3.4.6 Inner Calorimeter

A recent addition to the CLAS detector setup is a small total-energy calorimeter that can be placed inside the region 1 drift chambers: the inner calorimeter (IC). The IC is used in experiments that specifically require the detection of photons at smaller polar angles than the EC covers. The IC was also used by itself or in combination with the EC to reconstruct neutral pions from their primary decay into two photons. Figure 3.10 shows images of the IC, which consists of a matrix of 424 tapered lead-tungstate crystals coupled to avalanche photodiodes. In the EG1DVCS experiment the IC was placed less than 70 cm downstream

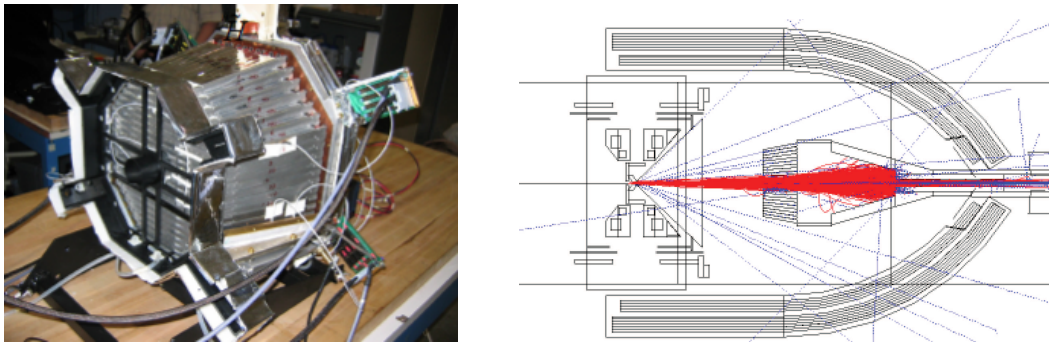

(a) Photograph of the IC. (b) Simulation of IC and target.

Figure 3.10: Images of the Inner Calorimeter. In (b) the output from a Monte Carlo simulation of the CLAS detector system is shown. In the centre is the IC and on the left is the target system, both are contained within the region 1 drift chambers. The red tracks represent Møller electrons originating from the target cell, which have been forward-focussed due the presence of the target field.

of the target cell[2].

3.5 Dynamically Polarised Target

A longitudinally polarised proton target was one of the experimental specifications of the EG1DVCS experiment. Solid-state ammonia ($^{14}NH_3$) was chosen as the target material because previous investigations have shown that it can be highly polarised ($> 90\%$) using the method of Dynamic Nuclear Polarisation (DNP), and it is resilient against radiation damage [85].

3.5.0.1 Dynamic Nuclear Polarisation of NH_3

In the case of ammonia, DNP works by continuously transferring polarisation from electrons in (mainly) $^{14}NH_2$ paramagnetic radicals to the $^{14}NH_3$ nuclei using tuned microwaves. The paramagnetic radicals are introduced to the $^{14}NH_3$ sample prior to the experiment[3]. The $^{14}NH_2$ molecules contain unpaired electrons which become polarised when placed in a magnetic field. A polarisation of unpaired electrons nearing unity can be achieved by cooling the material to $\sim$1 K and placing it in a strong magnetic field (> 5 T/K) [86]. Nuclear polarisation is achieved by inducing transitions that flip the spins of both the free-electrons and nearby nuclei using microwaves. The nuclear polarisation helicity direction is selected using the frequency of the microwave. This means that both polarisation states

[2] 57.95cm in Part A, 67.97 cm in Part B.

[3] In the case of EG1DVCS this was achieved by irradiating the sample at a small electron accelerator facility at NIST in Gaithersburg, Maryland.

(parallel and anti-parallel to the field direction) can be created without the need to flip the sign of the magnetic field. Electron spin relaxation times are much shorter ($\sim 10^{-3}$) than nuclear spin relaxation times ($\sim 10^{3}$). The same free-electrons can therefore be re-used to polarise nuclei. Nuclear spins are transferred between nuclei directly, which results in the bulk material becoming polarised. Over time the net polarisation of the nuclei increases and can reach over 90% [85].

3.5.1 The CLAS polarised NH_3 target

The target system used for EG1DVCS was developed specifically for electron scattering experiments at CLAS [86], utilising the DNP method discussed in the previous section. The design accommodates the measurement of exclusive processes, which require a large detector acceptance.

Target material is located in cells mounted on an insert that can be moved up and down remotely using a stepper motor. Figure 3.11 shows images of the target insert and the target system in CLAS. In parts A and B (C) of the experiment the top two cells contained $^{14}NH_3$ ($^{14}ND_3$). Amorphous Carbon was contained in the cell below the $^{14}NH_3$ cells and the bottom target was left empty. These two additional targets were included for the purpose of background studies. The Carbon target was used to represent the molecular part of $^{14}NH_3$. This system provided a method of alternating the target material during operation without the need to physically enter the hall. The magnetic field was created using superconducting Helmholtz coils. These coils are shaped to provide an opening aperture of 50°. Figure 3.10(b) is an output from a simulation showing the target magnet, which doubled up as a shield against Møller electrons.

3.6 Trigger System

The CLAS data acquisition system (DAQ) is operated by a two-tiered trigger [80]. In electron experiments, the Level-1 trigger is activated when there is both energy deposited in the electromagnetic calorimeters[4] and a signal above threshold in the Cherenkov counters. With these conditions fulfilled, all PMT signals arriving promptly are processed and used to gate PMT time-to-digital convertors and analogue-to-digital convertors. The Level-2 trigger is activated when suitable tracks in the drift chambers are found. If this condition is not met then the events satisfying the Level-1 trigger are cleared. This whole process takes only a few micro-seconds. If the Level-2 trigger is satisfied then signal digitisation occurs. The time taken to determine that the trigger condition is *false*, or *true plus*

[4]The EC threshold was set to 500 MeV for EG1DVCS.

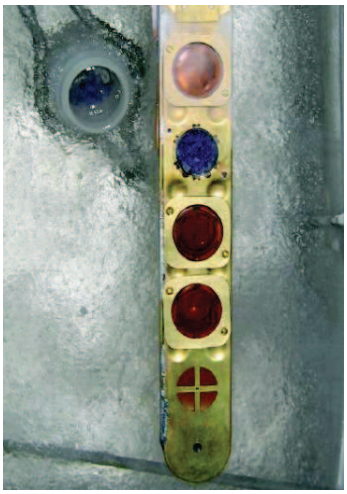

(a) Photograph of insert.

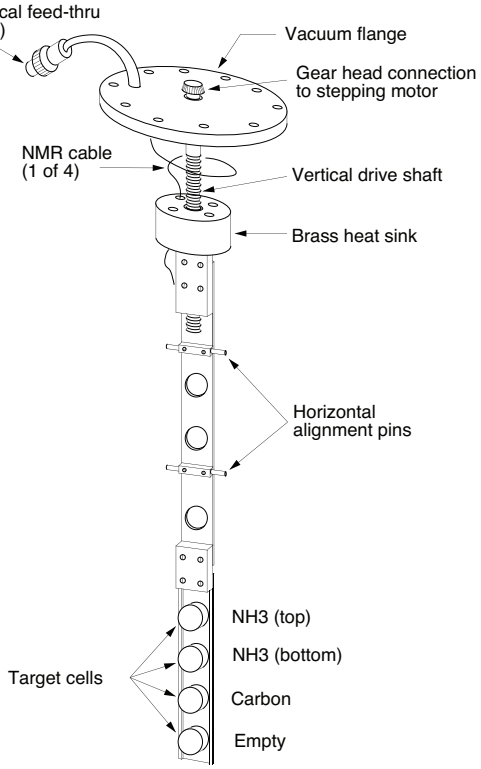

(b) Scale drawing of insert.

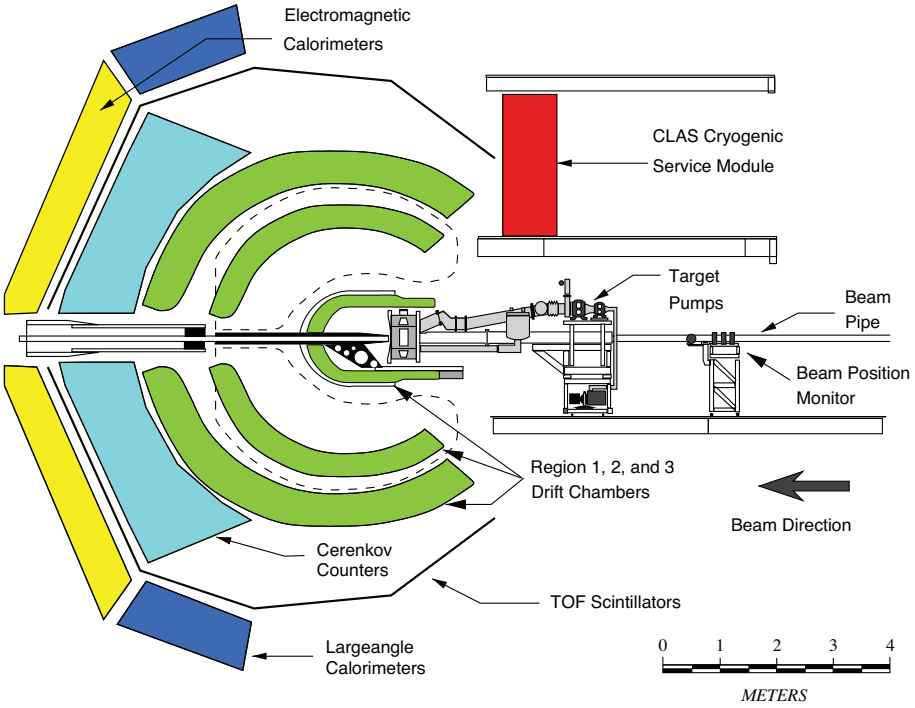

(c) Scale drawing of the target system in the CLAS detector.

Figure 3.11: Images of the CLAS NH_3 target system. In (a) the top target cells contain NH_3. The Kapton window has been removed in the second cell from the top revealing the irradiated ammonia beads, which are blue. The target insert sits in a Helium bath, which is used to cool it to cryogenic temperatures.

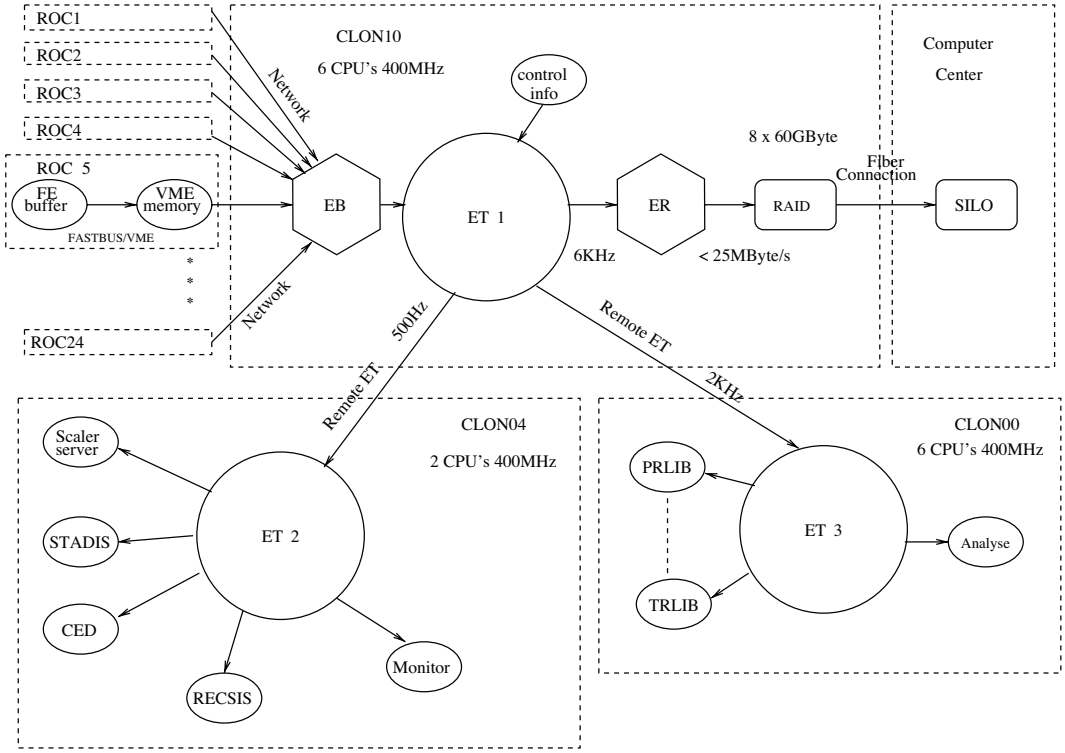

Figure 3.12: The data flow schematic for CLAS including: readout controllers (ROCs), the CLAS online acquisition computer CLON10, event builder (EB), event transporters (ETs), and event recorder (ER).

the time to undertake digitisation, contributes to dead-time: the time during which the detector cannot accept more triggers. Data readout is controlled by the *trigger supervisor* which can be programmed to accept either Level-1 or Level-2 triggers. Readout occurs independently of the triggering process and therefore does not contribute to dead-time.

3.7 Data Acquisition

The CLAS DAQ uses a UNIX operating system. The flow of data is represented in figure 3.12. Data are digitised in 24 VME crates then sent to matching readout controllers (ROCs) where they are organised in tables corresponding to active detector components. The resulting data arrays are then sent to the CLAS online acquisition system (CLON) which is used to process the event prior to permanent storage and live monitoring as follows.

The Event Builder (EB) combines the data arrays into *banks*, which contain complete events arranged in tables that can be easily linked. Each event is assigned: a unique event number, an event type, trigger information, and a run number. Each run number corresponds to the portion of data that was accumulated over a period between which the operator started and ended the DAQ system. During EG1DVCS a typical run was

ended once 40 M events were recorded. The event transporters (ET1, ET2, ET3) are used to provide shared access to data between various live monitoring processes and final processing by the event recorder (ER). The ER writes the data to a local RAID array then sends it to a remote tape silo.

3.8 The EG1DVCS Experiment

The primary goal of the EG1DVCS experiment was [75]:

> To study the target single spin asymmetries (SSA) in deeply virtual Compton scattering (DVCS) using the CEBAF 6 GeV polarised electron beam, a polarised solid state $^{14}NH_3$ target, and the CEBAF Large Acceptance Spectrometer together with the newly built Inner Calorimeter.

This was the first dedicated DVCS target spin asymmetry experiment to be carried out at Jefferson Lab. The proton DVCS target spin asymmetry was previously measured in Hall B at Jefferson Lab using the EG1b experiment data set [76] and has also been measured by the HERMES collaboration [74].

In EG1b, only a fraction of the data were taken with a high enough beam energy for reactions to fall within the Bjorken scaling regime, and photon detection was limited to relatively large polar angles ($\theta_\gamma > 8^\circ$) [73]. DVCS analyses were not the main objective of EG1b and thus the statistics were only sufficient to extract the dominant $\sin(\phi)$ amplitude in three kinematic bins.

The HERMES collaboration obtained results for the proton target spin asymmetry and double spin asymmetry using a polarised ($\approx 50.0\%$) positron beam on a polarised ($\approx 80.0\%$) gaseous hydrogen target. Final state protons were not detected in this experiment, which resulted in the final sample being contaminated by events from: semi-inclusive DIS, resonance production and π^0 production. The magnitude of contamination was quantified using Monte Carlo simulations.

During EG1DVCS operation, almost the maximum energy (6 GeV) electron beam available at Jefferson Lab was utilised for most of the run period. Table 3.1 lists some key figures on EG1DVCS running, including beam energies and start and end dates of each part of the experiment. The experiment ran for a combined total of 127 days at twice the (final state) luminosity of any previous electron scattering experiments in Hall B (1.4×10^{34} Z/A nucleons $cm^{-2}s^{-1}$ [5]). This high rate was possible due to the effectiveness of the polarised target's Helmholtz magnets at screening against Møller electrons [75]. The addition of the inner calorimeter to the standard CLAS configuration gave access to a phase-space region where, according to simulations, the DVCS spacial is larger [73]. The combination of these experimental benefits of EG1DVCS mean that there is over an order of magnitude more statistics in the final DVCS sample ($\approx$73,911) than either the EG1b experiment (1,793) [75] or the HERMES result (2,824) [87] had. In addition to the measurement of DVCS target single spin asymmetries on protons, a number of

[5] Units give Hydrogen target equivalent luminosity.

part	target z position (cm)	primary target	run numbers	beam energy (GeV)	torus current (A)	dates [start,end] (D M Y)
A	-57.95	$^{14}NH_3$	58708 - 59161 59161 - 59220	5.887 4.730	2250.0	[04 02 09, 16 03 09]
B	-67.97	$^{14}NH_3$	59221 - 59978 59978 - 60004 60005 - 60223	5.954	2250.0 -2200.0 2250.0	[23 04 09, 14 06 09]
C	-68.18	$^{14}ND_3$	60223 - 60648 60648	5.752	2250.0	[21 08 09, 22 09 09]

Table 3.1: Run information for the EG1DVCS experiment

other studies are being undertaken with the EG1DVCS data set. As Table 3.1 indicates, a Deuterated Ammonia target was used for part of the assigned beam time to allow for studies requiring a Neutron target. Analyses that are undergoing include:

- Proton DVCS double spin asymmetries.
- Neutron DVCS beam and target spin asymmetries.
- Semi-inclusive deep-inelastic scattering (SIDIS) single and double spin asymmetries for pions on protons [31] and neutrons.
- Inclusive polarised structure functions on protons and deuterons.
- Deeply virtual meson production (DVMP); exclusive neutral pion production.
- Di-hadron asymmetries.
- Nuclear single spin asymmetries.

3.9 Summary

In combination, the stable CEBAF electron beam, multi-functional CLAS detector system, highly polarised target and robust data acquisition system provided an experimental setup that was well suited to the measurement of the exclusive electroproduction of photons. In the following chapters the analysis procedure used to extract DVCS spin asymmetries from the data recorded during EG1DVCS will be discussed.

Chapter 4

Analysis 1 - Event Selection

This chapter explains the procedure used to select the sample of events that the asymmetry analysis was carried out with. This involved firstly identifying the three final state particles in the exclusive electroproduction of photons reaction: $e + p \rightarrow e' + p' + \gamma$. After the particles were individually identified, the reaction as a whole was isolated using exclusive variable distributions. Exclusive variables will be discussed in Section 4.8.

A second analysis was undertaken to identify events corresponding to the exclusive electroproduction of neutral pions: $e + p \rightarrow e' + p' + \pi^0 \rightarrow e' + p' + \gamma\gamma$. This was necessary because it was not possible to completely eliminate neutral pion production events from the exclusive electroproduction of photons sample. The main decay mode for neutral pions is into two photons. Events in which one of the two decay photons was detected, and the other escaped detection, contributed to the photon production event sample as a source of background. The amount of contamination was quantified using Monte Carlo simulated data. The procedure used will be described in the next chapter. The particle identification and exclusive cuts used to identify this reaction will be described in this chapter.

Before the event selection methods are discussed, the data processing procedures that were carried out prior to them will now be outlined.

4.1 Calibrations, Cooking and Skimming

In Hall B experiments, the raw data take the form of values recorded in time-to-digital convertors (TDCs) and charge-to-digital convertors (QDCs), which are arranged in banks; this was already mentioned in Chapter 3. In CLAS terminology, the process by which the raw data are converted into useful analysis variables – such as the positions of hits in the detectors, deposited energy, and particle momenta – is called cooking.

To identify any effects that the specific experimental setup for the EG1DVCS exper-

iment had on the data compared to previous CLAS experiments, and also to account for changes to the experimental configurations for different run periods, calibration studies for each sub-detector system were carried out using the cooked data. These studies were performed by experienced members of the EG1DVCS analysis group and included: DC hit position and timing alignments, EC and CC pulse height corrections, SC timing corrections and IC energy and timing calibrations. Once the calibrations were optimised, the data were corrected by re-cooking them using results from the calibration studies as input. The final data form, which was used in this analysis, is referred to as pass-1 data. This data consisted of around 60,000 files in total, which were grouped by run number, with each run containing about 85 files.

Events in which the DAQ system was not triggered by an electron or positron were removed from the sample of data. This is an example of what is known in CLAS terminology as data-skimming. The method used to identify electrons as the triggering particle will be discussed below. Events containing positrons were not included in this work. The resulting file type was a PAW (physics analysis workstation) [88] format called Ntuple-10. A further data-skim was carried out to minimise the data size by an order of magnitude by removing unessential variables and applying bit compression. The resulting format is known as Ntuple-22. The Ntuple-22 files were converted to a format called ROOT-22, to accommodate analyses within the ROOT data analysis framework [89]. New data versions were made when modifications or additions to the included variable types were made. The final data form that was used as the starting point for this analysis was: *pass-1, version-3, ROOT-22*.

4.2 Data Quality and File Rejection

Prior to the event-by-event analysis, the data were checked on a file-by-file basis. The files used in this analysis were selected following the procedures outlined in a run group technical note [90]. Files in run periods with similar experimental configurations were arranged into 65 groups and the electron rate distributions for each sector within each group were compared. Anomalous electron rates indicate that there was a temporary problem with a vital detector component. Files with electron rates that fell outwith 5-σ of the mean rate of the group they were part of were rejected. Files were also rejected if they had: missing or incorrect Faraday cup information, zero target polarisation, or a missing data structure.

A further check of the election rates was performed once the electron identification procedures of this analysis were finalised. Electron identification will be explained in Section 4.5.1. It was discovered that for three run numbers, there were files with very

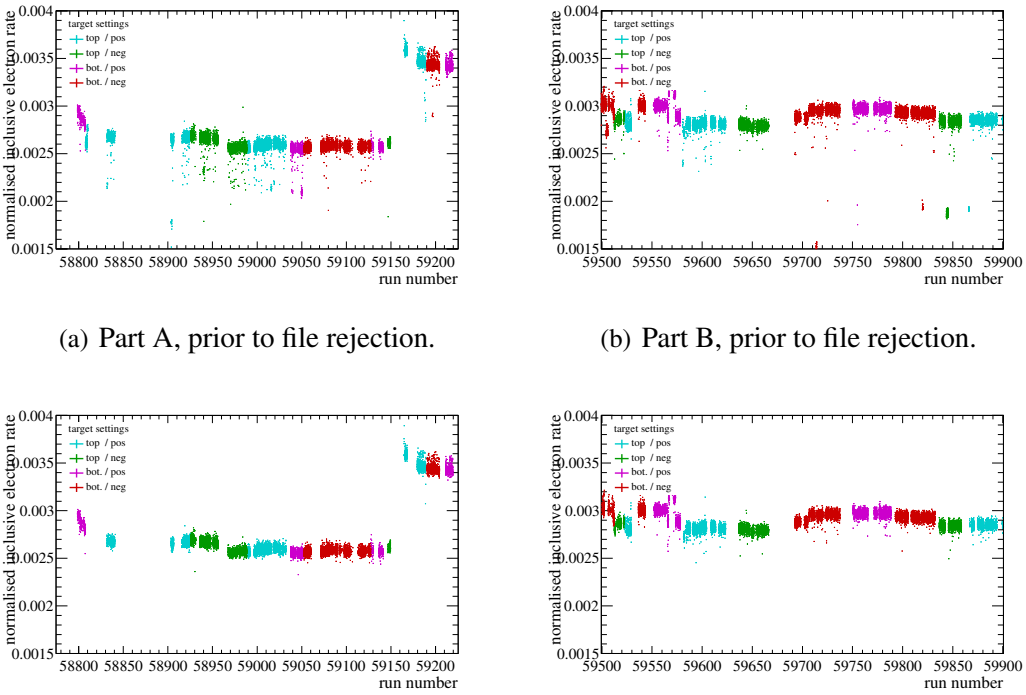

(a) Part A, prior to file rejection.

(b) Part B, prior to file rejection.

(c) Part A, after file rejection.

(d) Part B, after file rejection.

Figure 4.1: Electron rates per file for both NH3 target cells, normalised to the beam charge collected for events triggering the DAQ (integrated faraday cup current). In (a) and (c) all files were included. In (b) and (d) only good files (see text) were included. The step features are a result of changes in configuration. In (a) and (c) the high rates of the run numbers around 59200 are due to a change in beam energy from 5.9 GeV to 4.7 GeV. Small step variations result from the slightly different radiation lengths of the top and bottom targets.

low electron rates: 59714, 59844 and 59845. A check of the electronic experimental logbooks confirmed that there had been a problem with a major detector component during these runs. During run 59714 the SC crate crashed and a high voltage board had to be replaced. During runs 59844 and 59845, there was a problem with the EC TDCs, which was resolved by rebooting them.

A study of the stability of neutral pion masses [91] highlighted that during runs 58813 and 58814 a problem occurred with the Inner Calorimeter.

Instabilities in the transverse beam position caused the beam to hit the target cell wall during some runs. A study of the extent of this effect was written up as a technical note [92] and found to affect only a few runs.

Files that failed any of these additional checks were rejected from this analysis. Figure 4.1 shows inclusive electron rates (summed over all sectors) per file as a function of run number before and after bad file rejection for data taken on both top and bottom NH_3 targets. Data taken with the Carbon and Empty targets were treated in a similar manner.

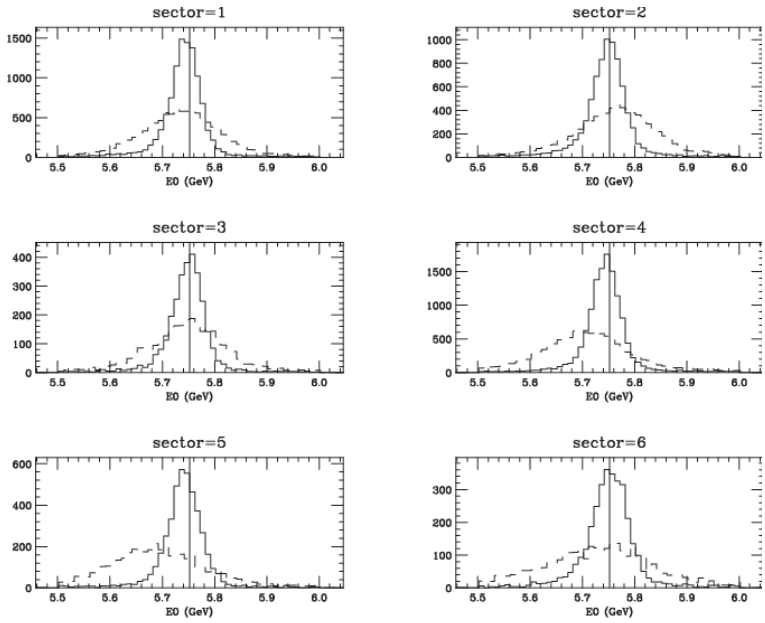

Figure 4.2: Beam energy calculated from elastic electron-proton scattering before (dashed line) and after (solid line) a correction to the direction cosines of charged particles. Results for part C data are shown here.

4.3 Data Corrections

4.3.1 Charged particle vertices and direction cosines

The standard CLAS method of determining the direction-cosine vector of a charged particle at the interaction vertex involves extrapolating it backwards through the DC superlayers to the position that intersects a plane perpendicular to the sector it traversed. To improve the accuracy of the vertex position, the (x, y) position of the beam was calculated using the raster ADC values. The z-coordinate and direction-cosines were then determined by extrapolating the charged particles back through the target magnetic field from DC layer 1 to this position. These procedures were adopted from run group technical notes [93, 94]. Figure 4.2 shows, sector-by-sector, the effect this correction had on the beam energy as reconstructed using elastic electron-proton scattering. Both the peak-energy sector-dependence and energy-widths were improved.

4.3.2 EC energy

Slow gain-drifts were observed for the EC after periods where the EC PMT high voltages had been switched off. The source of these drifts was never found. A run-by-run, sector-by-sector correction factor to EC energy values was applied, which was considered to be sufficient since the gain drifts were correlated in time [91]. Figure 4.3 shows the effect of this correction on the detected energy relative to the detected momentum for electrons.

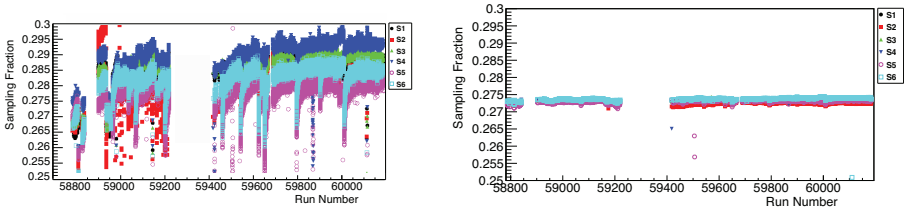

(a) Before correction. (b) After correction.

Figure 4.3: Ratio of energy deposited in the EC to momentum (sampling fraction) for electrons before and after the application of EC gain correction factors. Files corresponding to the outlying data points were not included in this analysis.

4.4 Event Selection

The cuts used in the data skimming process had the function of removing events that were of no potential interest to any EG1DVCS analysis. Events with potential electron candidates were identified by applying the following conditions:

- **DC charge = -1 e**. Particle charge was used as the primary means of particle identification. Negative particles were identified using the curvature of trajectories in the drift chambers.

- **DC momentum $>$ 0.5 GeV/c**. The EC energy threshold set in the DAQ trigger was taken as the minimum acceptable momentum value.

- **EC timing $>$ 0.00 ns and SC timing $>$ 0.00 ns**. Only time-based drift chamber tracks were included in the pass-1 data sample. DC tracks with only hit-based information were discarded by ensuring that timing information was utilised. Time-based tracks benefit from improved positional resolution, which is achieved by correcting the DC hit positions using SC timing information [73].

- **EC sector number = CC sector number = DC sector number**. Equating the sector numbers of sub-detector systems imposed an element of positional matching, which had the effect of reducing contributions from random coincidences.

- **CC geometrical matching variable $<$ 0.15**. The angle between the SC and CC (in radians-squared) was used as a means by which to match electron candidate tracks. The value taken corresponded to an agreement of the hit position in a CC chamber to within 4 paddles (scintillator bars) of the SC. A study written up as a technical note [95] showed that the majority of electron candidates fell within 2 SC paddles. Negative pions below the minimm threshold required to produce Cherenkov light in the CC can knock-out electrons at large angles. Random coincidences can occur in

the SC and CC. Contributions to the signal background from both of these scenarios were reduced by applying this condition.

- **EC deposited energy/DC momentum $>$ 0.12 c**. At large momentum values ($>$2.5 GeV/c) it is not possible to separate pion events from electron events using the CC, because both particles create Cherenkov light in the CC gas volume. The energy recorded in the EC is almost independent of momentum for pions. This condition provided a means with which to suppress the contribution from pion events that did have a corresponding signal in the CC.

The events of interest to this analysis require the presence of an electron in the final state. These data-skim cuts were used as a preliminary method of identifying electrons. Events without at least one particle fulfilling all of these conditions were removed from the sample used in the following procedures.

4.5 Particle Identification

The final state particles of the reactions $ep \rightarrow ep\gamma$ and $ep \rightarrow ep\pi^0$ were identified by applying further data cuts to the sample containing at least one preliminary identified electron. This section explains in turn the procedure used to identify each particle.

Some of the standard particle identification data cuts that are needed for inclusive or semi-inclusive processes can be loosened or even omitted when all final state particles are identified. For inclusive DIS processes a strict electron identification procedure is required as there is no other means by which to adequately minimise the background contribution from reactions containing other negative particles (mainly pions) instead of electrons. For SIDIS processes, and exclusive reactions in which one of the final state particles is identified using the missing mass method, strict particle identification cuts are also required in order to suppress the background contributions caused by particle misidentification. When all final state particles of the reaction being studied are identified, the misidentification of particles is further suppressed at the stage of reaction identification, where events are selected based on quantities that utilise complete information on the initial and final states. In this work some of the particle identification cuts were therefore relaxed compared to those used in inclusive [96] and semi-inclusive [31] analyses that were carried out with the same EG1DVCS data.

4.5.1 Electron identification

The identification of events with one and only one good electron was carried out before identifying other particles. Electron identification cuts had the combined function of: reducing the combined noise background, rejecting events containing negative pions and rejecting events from regions where the detector efficiency was poor. The preliminary electron ID cuts that were outlined in the previous section were first applied to every particle in every event. Particles fulfilling all of the these conditions were then subjected to the following constraints:

1. **DC momentum $>$ 0.8 GeV/c**. Electron candidates with momenta below 0.8 GeV/c were removed. In this region the CC suffers from low efficiency and radiative events contribute a significant source of background. Figure 4.4 shows distributions of electron events after the application of all electron ID cuts apart from this cut.

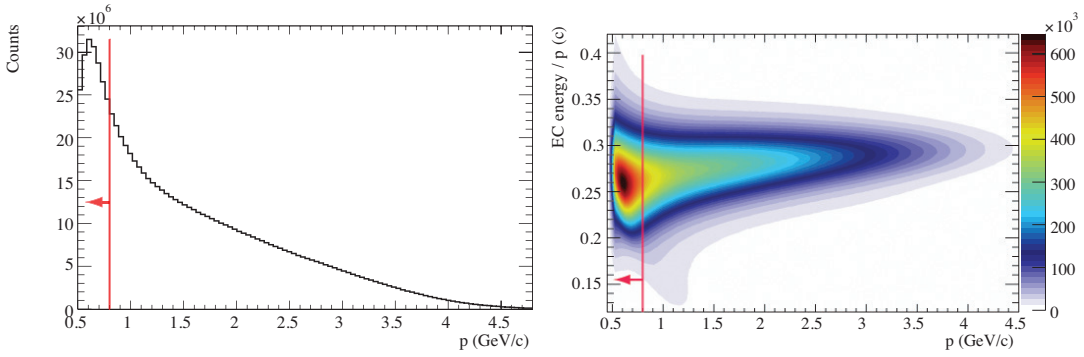

(a) DC momentum. (b) Sampling fraction vs DC momentum.

Figure 4.4: Electron ID data cut 1. The red lines shows the position of the cut applied and the arrows indicates the discarded region.

2. **Inner EC deposited energy $>$ 0.06 GeV**. Moderately high energy (2.9 GeV $<$ E_{π^-} $<$ 6.0 GeV) pions mainly deposit energy through the process of ionisation. The amount of energy deposited by ionising particles depends on the thickness of the material through which they travel and is almost independent of their momentum. Figure 4.5 show distributions of the energy deposited in the inner part of the EC for electron candidates after all cuts apart from the cut on this variable. In 4.5(b) this variable has been plotted against (10$\times$) the number of photoelectrons detected in the CC. Below 0.06 GeV and the two photoelectron level is a peak of negative pion events which were removed by applying this cut.

3. **|z-vertex - target centre| $<$ 3.0 cm**. Interactions that occurred outside of the target material were not of interest to this analysis. Contributions from interactions that occurred in the target cell windows and other material through which the electrons

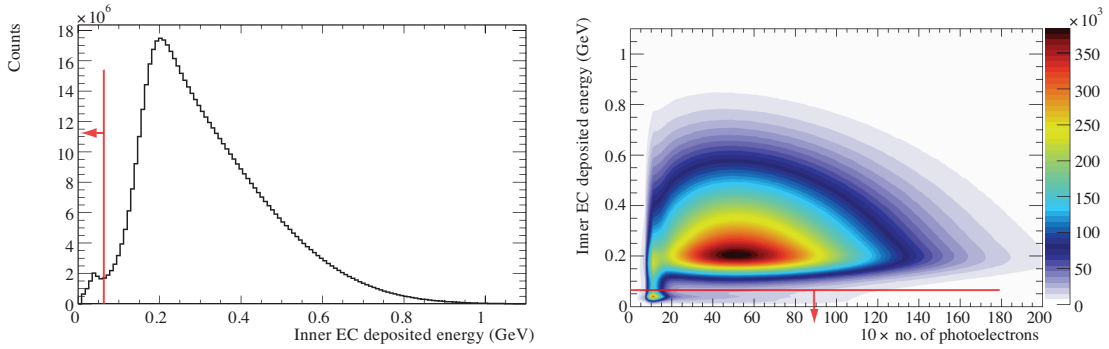

(a) Inner EC deposited energy (EC_{Inner}). (b) EC_{Inner} vs CC number of photoelectrons.

Figure 4.5: Electron ID data cut 2. The red lines shows the position of the cut applied.

traversed were minimised by applying this cut. Figure 4.6 shows the z-vertex after all other electrons ID cuts apart from this one.

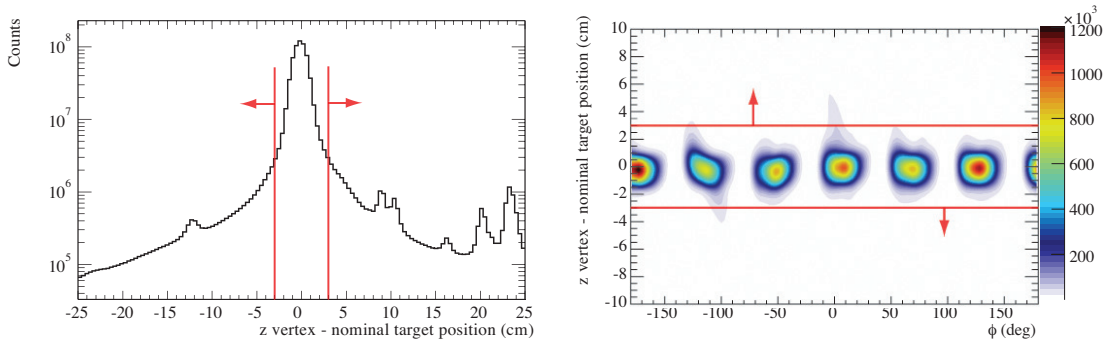

(a) z-vertex at target (b) z-vertex vs ϕ at DC layer 1

Figure 4.6: Electron ID data cut 3. Note that a log-scale has been used in (a). The red lines shows the positions of the cut applied.

4. $|$**CC time - start time**$|$ $<$ **2.0 ns**. Electron candidates travelling from the target traverse the CC before the SC. The time difference between interactions in these two sub-detector systems depends on particle velocity. At the same momentum, pions travel slower than electrons which means that the time taken to travel from the CC to the SC is longer. This cut was used to remove the contribution from negative pions and random coincidences. Figure 4.7 shows the time difference after all other electrons ID cuts apart from this one.

5. **Standard EC fiducial cut**. The detection efficiency at the edges of the EC is poor because when particles interact there the electromagnetic shower is not completely contained within the detection volume. It is a common procedure in many CLAS analyses to apply what are know as standard fiducial cuts (FCs), which limit retained events to regions that have been identified as having good detection efficien-

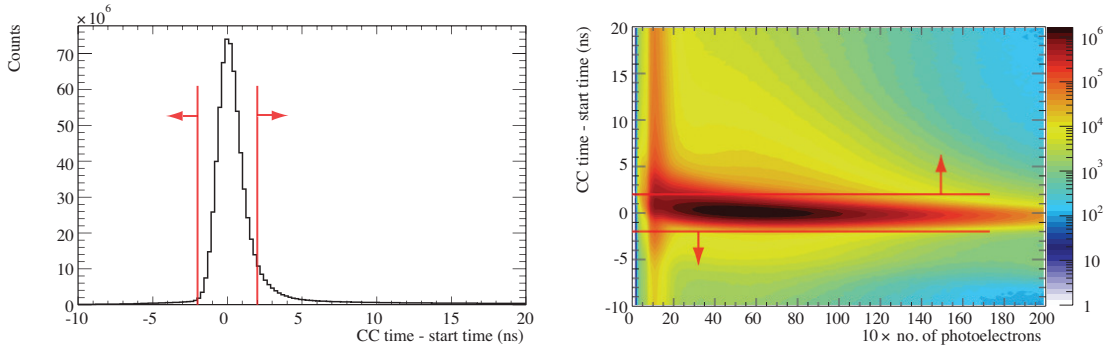

(a) CC time relative to SC time (Δt). (b) Δt vs nphe

Figure 4.7: Electron ID data cut 4. CC time was corrected for the travel time from the target to the interaction in the CC. Note that in (b) a logarithmic scale has been used. The red lines shows the positions of the cut applied.

cies . Figure 4.8 shows EC hit positions for electron candidates in terms of lab (x,y) and EC (U,V,W) coordinate systems; see the previous chapter for an explanation of these coordinate systems.

6. **IC shadow fiducial cut**. The position of the IC within the centre of the CLAS detector system caused the paths for particles at small scattering angles to be blocked. Some small angle scattering particles were detected after interacting with the support structure surrounding the IC. The position and energy of these events was not well reconstructed. To eliminate badly reconstructed events a charge- and momentum-dependent fiducial cut [97] was applied to electron candidate events. Figure 4.9 shows angular positions of electron candidates after all other electron identification cuts and those that were rejected by this cut.

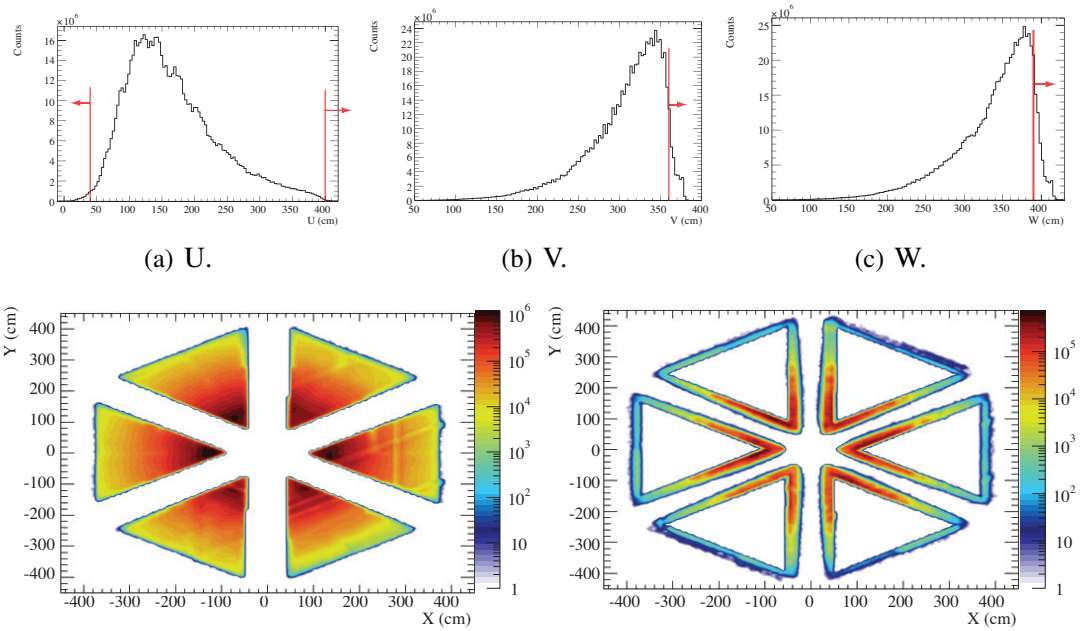

(a) U. (b) V. (c) W.

(d) EC hit positions after all cuts. (e) Events rejected by this cut.

Figure 4.8: Electron ID data cut 5. The distributions in (a)-(c) are plotted after all electron ID cuts apart from this one. The red lines show the positions of the cuts applied. In (d) the positions of good electron candidates are plotted in terms EC positions in lab-coordinates. The events rejected by this cut after all other cuts were applied are shown in (e).

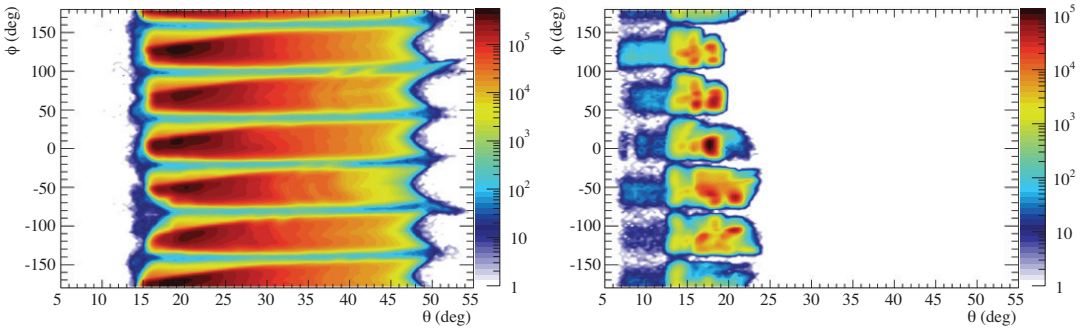

(a) Angular positions of good events. (b) Angular positions of rejected events.

Figure 4.9: Electron ID data cut 6. In (a) the electron candidates remaining after all electron cuts have been applied are shown. In (b) the events removed by this cut after all other electron ID cuts are shown. Note the log scale in the z-direction.

4.5.2 Proton identification

The identification of protons was achieved using the sample of events containing one and only one fully identified electron per event. The following conditions were used to reject events with positive tracks that corresponded to: random coincidences, positive pions, positive kaons, deuterons, and other heavier ions.

1. **|z-vertex - target centre| < 4.0 cm**. For proton candidates, as with electron candidates, only interactions that occurred in the target material were of interest. The vertex-resolution is not as good as for electrons. The cut applied was therefore made slightly wider for protons. Figure 4.10 shows plots of the z-vertex for proton candidates after all other proton ID cuts apart from this one.

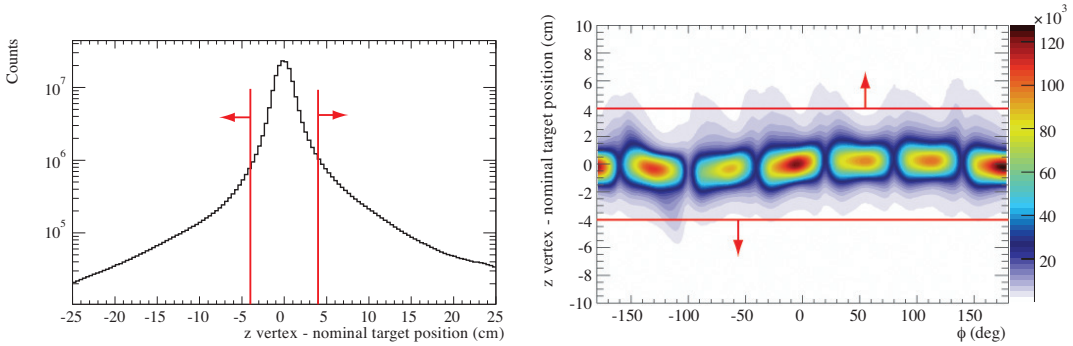

(a) z-vertex at target. (b) z-vertex vs ϕ

Figure 4.10: Proton ID data cut 1. The red lines show the positions of the cut applied.

2. **Momentum-dependent β cut**. The primary means to distinguish protons from other positively charged particles involved using a combination of DC momentum and SC timing information. The velocity relative to the speed of light $\beta = d_{SC}/(ct_{SC})$ was calculated using the distance travelled from the target to the interaction point in the SC (d_{SC}) and the time taken to travel that distance (t_{SC}): the time recorded minus the start time. Figure 4.11(a) shows β plotted against momentum after all proton ID cuts apart from the cut on this variable. Figure 4.11(b) shows the same plot after this cut. Figure 4.11(c) shows the difference in time calculated using the SC timing and DC momentum $\Delta t_{pr} = t_{SC} - d_{SC}(p^2+m^2)^{1/2}/(pc) = t_{SC} - d_{SC}/(\beta_p c)$ after all proton ID cuts apart from the cut on this variable. Figure 4.11(d) shows the same plot after this cut. At larger momentum values the timing resolution is better. This meant that the cut width could be made more narrow at higher momentum values where the β values for positive pions are closer to those of protons.

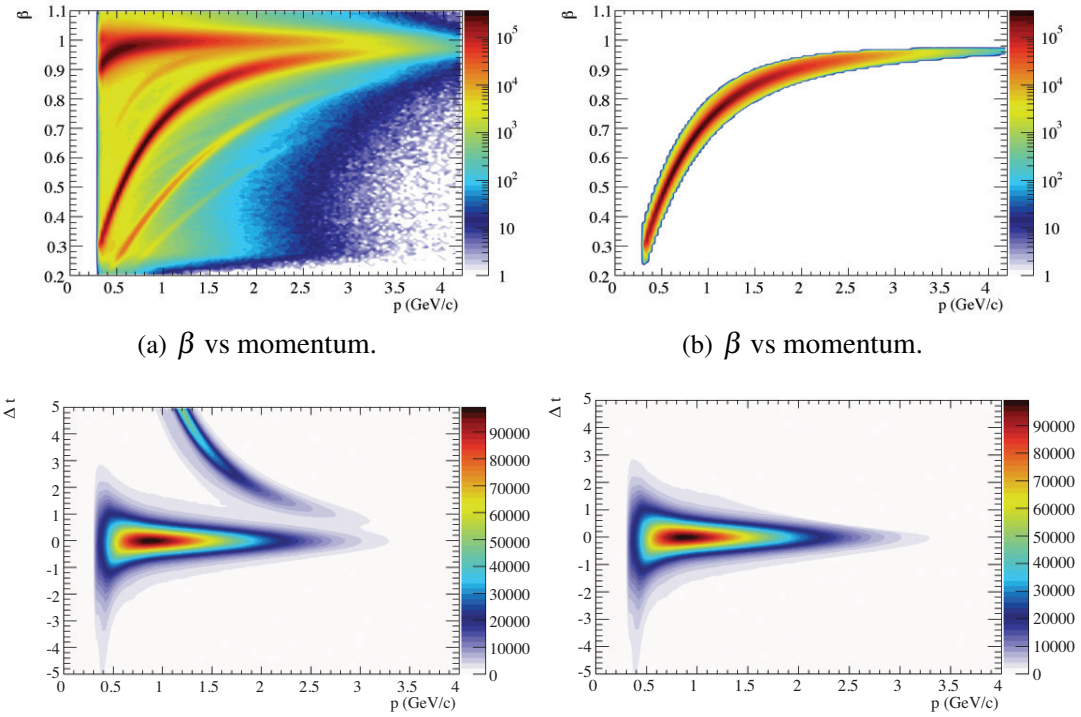

(a) β vs momentum.

(b) β vs momentum.

(c) Δt_{pr} vs DC momentum.

(d) Δt_{pr} vs DC momentum.

Figure 4.11: Proton ID data cut 2. In (a) and (c) regions which contain events from protons, pions, kaons and deuterons can be distinguished; (b) and (d) show the effect of the momentum-dependent β cut.

3. **IC shadow fiducial cut**. Proton candidate events were subjected to a positively-charged particle version of the same IC shadow fiducial cut as electrons [97]. Figure 4.12 shows the positions of proton candidates in terms of the lab coordinates (ϕ, θ) and the events rejected by this cut after all other proton ID cuts were applied.

4.5.3 EC photon identification

Photon identification was split into two categories corresponding to the two different photon-detectors: EC and IC. This section details the procedures used to identify photons that were detected in the EC. EC photon cuts were applied to the set of events containing one and only one fully identified electron and one and only one fully identified proton. Particles that were detected in the EC with no corresponding charged track in the DC were assigned neutral charge. In order to identify photons, neutral EC particles were subjected to the following conditions:

1. $\beta > \mathbf{0.92}$ **c**. Neutral particles that are detected in the EC include neutrons and photons. To eliminate neutrons from the sample a fixed cut was applied to $\beta = d_{EC}/(ct_{EC})$, where t_{EC} is the time recorded minus the event start time and d_{EC} is

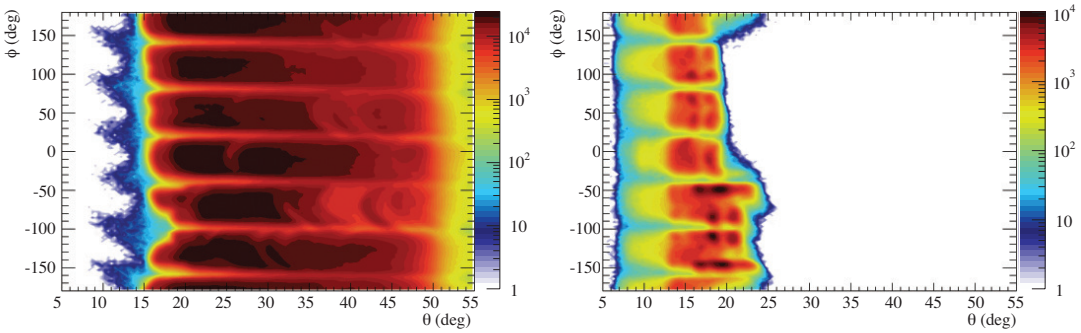

(a) Angular positions of good events. (b) Angular positions of events.

Figure 4.12: Proton ID data cut 3. These plots are equivalent to those in Figure 4.9 except here proton candidates are shown.

the distance travelled from the target to the EC. Figure 4.13 shows β distributions after all EC photon cuts apart from the cut on this variable.

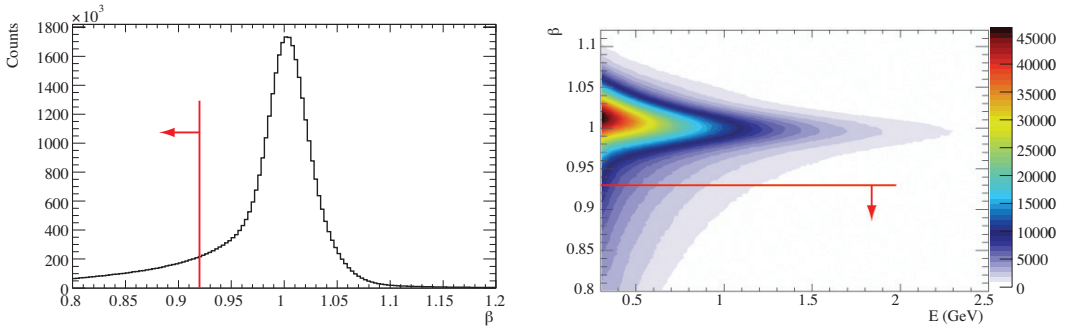

(a) β. (b) β vs energy.

Figure 4.13: EC Photon ID data cut 1. The red lines show the position of the cut applied.

2. **Energy $>$ 300 MeV**. The minimum energy value for EC photons in the data skim was 250 MeV. Below this energy the efficiency of the EC is poor which means that energies, timing and positions are not well reconstructed. The selection of events corresponding to the exclusive electroproduction of photons and the exclusive electroproduction of neutral pions, both required photons to be identified. Neutral pions were reconstructed from their primary decay mode into two photons. In the photon production case it was found that it was not possible to distinguish good events from the combined background for photon energies below 1 GeV. This additional cut was applied along with kinematic cuts which are discussed in Section 4.7. In the neutral pion production case the minimum energy for EC photons at which the signal to background ratio for neutral pion masses was found to be maximal was at 300 MeV [98]. Figure 4.14 shows the EC energy for photon candidate events after all EC photon cuts apart from the cut on this variable.

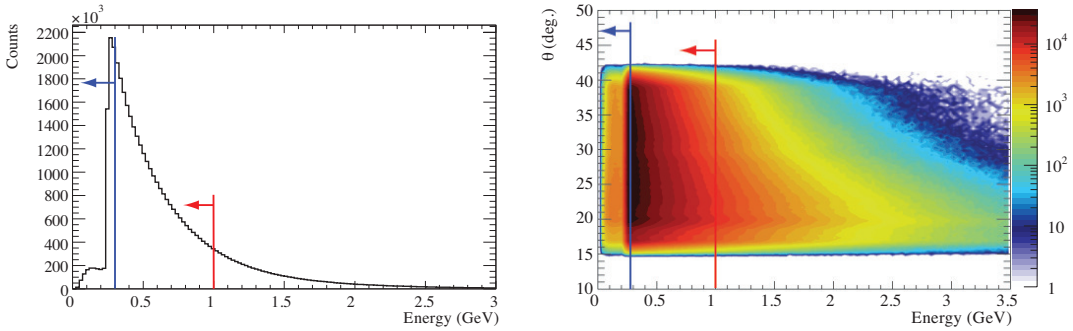

(a) EC Energy. (b) θ vs Energy.

Figure 4.14: EC Photon ID data cut 2. The red (blue) line shows the position of the cut applied to EC neutral particles in photon (neutral pion) production candidate events.

3. **Standard EC fiducial cut**. The same EC standard fiducial cut that was applied to electrons was applied to EC photon candidate particles. Figure 4.14 shows the same plots as in Figure 4.8 but for photons candidates instead of electrons.

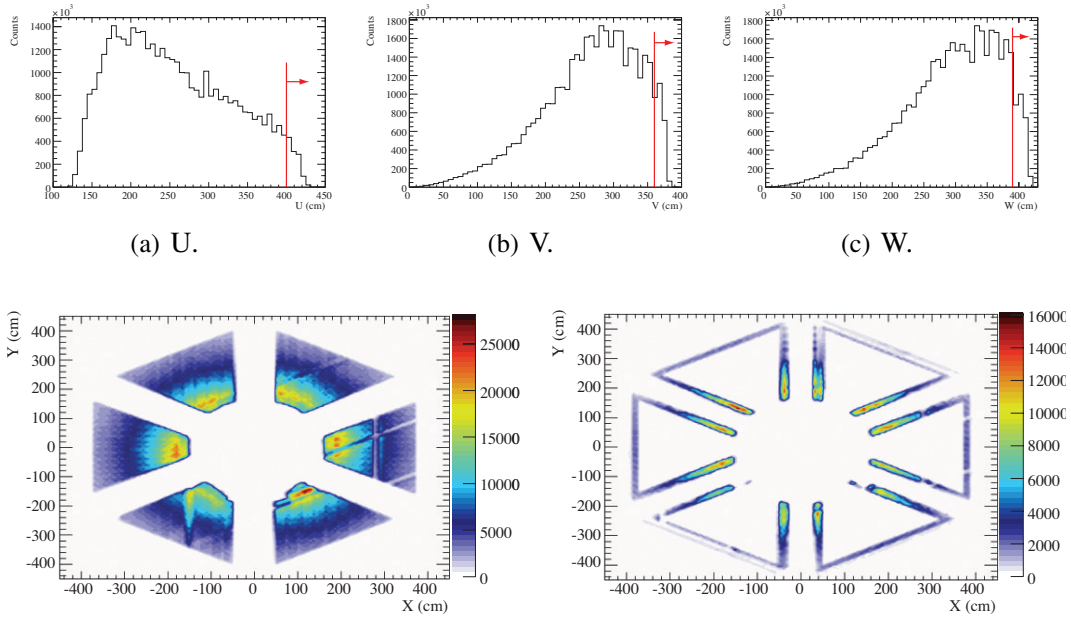

(a) U. (b) V. (c) W.

(d) (x,y) positions after all cuts. (e) Events rejected by this cut.

Figure 4.15: EC Photon ID data cut 3. The red lines show the positions of the cuts applied.

4. **IC shadow fiducial cut**. A neutral particle version of the fiducial cut [97] that was applied electron and proton candidate events was applied to photon candidates. In this case there was no momentum-dependence included in the conditions because neutral particles travel in a straight line. Figure 4.16 shows the positions of EC photon candidates that were rejected by this cut, and the scattering angle distribution for good events.

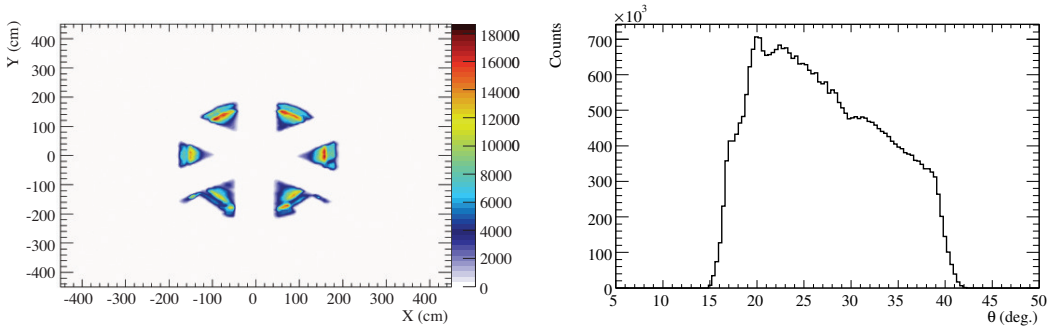

(a) Events rejected by this cut. (b) θ after all EC photon ID cuts.

Figure 4.16: EC Photon ID data cut 4.

4.5.4 IC photon identification

IC particles were presumed to be neutral in charge. The particle identification and reaction cuts were relied upon to eliminate the contributions from other particles.

1. **Energy $>$ 300 MeV**. The same minimum energy values used for EC photons were set for IC photons. As was the case for the EC, the IC was used to detect single photon events and events in which two photons were used to reconstruct neutral pions. Figure 4.17 shows the IC energy for photon candidate events after all IC photon cuts apart from the cut on this variable.

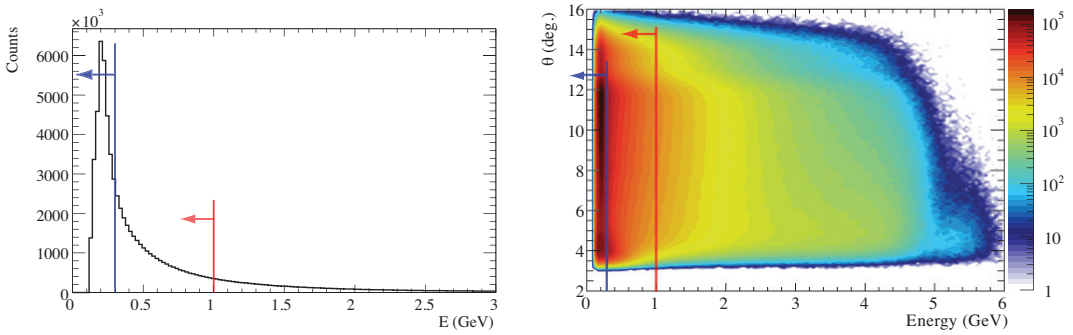

(a) Energy. (b) θ vs energy.

Figure 4.17: IC Photon ID data cut 1. The red (blue) lines shows the position of the cut applied for photon (neutral pion) production candidate events.

2. **Fiducial cut**. The energy and position reconstruction of events in the IC was achieved using a clustering algorithm that performed a weighted sum of hits in neighbouring crystals. Photons that interacted at the edges of the IC ($< 3/4$ of the width of a crystal from the edge) are not reconstructed well and were therefore removed from the event sample. Figure 4.18 shows the hit positions in the IC after all other IC photon ID cuts apart from this one.

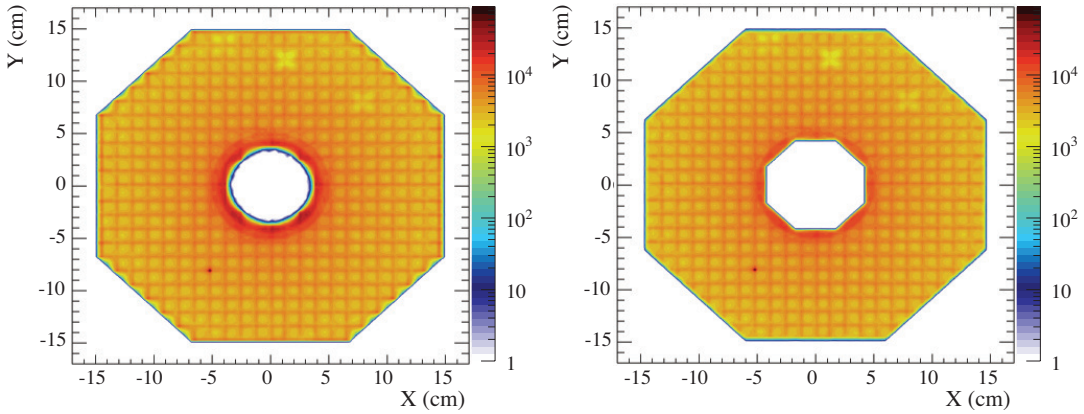

(a) Before this cut. (b) After this cut.

Figure 4.18: IC Photon ID data cut 2. Hit positions in the IC after all other IC photon ID cuts.

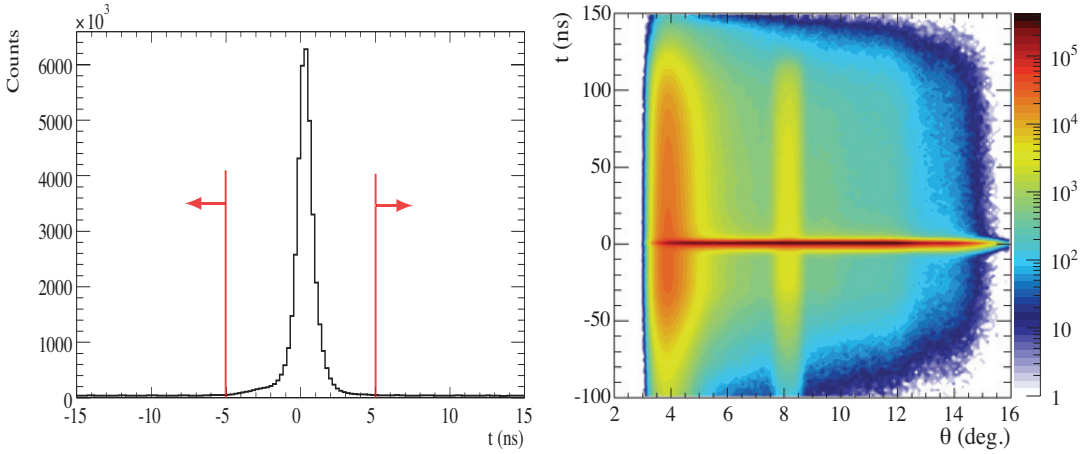

(a) Time. (b) Time vs θ.

Figure 4.19: IC Photon ID data cut 3. In (b) the distribution at 8 degrees is due to a malfunctioning pixel. The red lines show the position of the cut applied.

3. $|\mathbf{t}| < \mathbf{5}$ **ns**. The IC central region is positioned close to the beam line. A significant background signal from the electron beam was detected in the IC at low angles. These events were not synchronised in time with the event start time and the majority of them were removed from the sample by applying this timing cut. Figure 4.19 shows timing distributions for IC particles after all IC photon cuts apart from the cut on this variable.

4.5.5 Neutral pion identification

There were two photon detectors which means that there were three detector combinations that could be used to detect neutral pions: two photons detected in the IC, two photons detected in the EC, or one photon detected in each. The background reaction of interest

($ep \to ep\pi^0$) required the identification of an electron and a proton in the final state. The identification of events containing a neutral pion was therefore carried out using the sample of events containing one and only one electron and one and only one proton. Neutral pion candidates were identified by cycling through every combination of two good photons in each event and selecting good events based on the value of the reconstructed pion mass, $M_{\gamma\gamma}$, compared to the particle data group (PDG) value, $M^{\pi^0}_{PDG}$.

Three different mass cuts were used to identify events containing neutral pion candidates depending on the photon detection topology. The reconstructed-mass distribution widths varied due to the different resolutions of the EC and IC. The cuts used coincide with the optimal widths found for semi-inclusive processes, which are explained in a run group technical note [98]. The values used were: $|M_{\gamma\gamma} - M^{\pi^0}_{PDG}| < 0.030$ GeV/c^2 for IC-IC events, $|M_{\gamma\gamma} - M^{\pi^0}_{PDG}| < 0.035$ GeV/c^2 for EC-EC events, and $|M_{\gamma\gamma} - M^{\pi^0}_{PDG}| < 0.035$ GeV/c^2 for IC-EC events. Figure 4.20 shows mass distributions for the three possible cases.

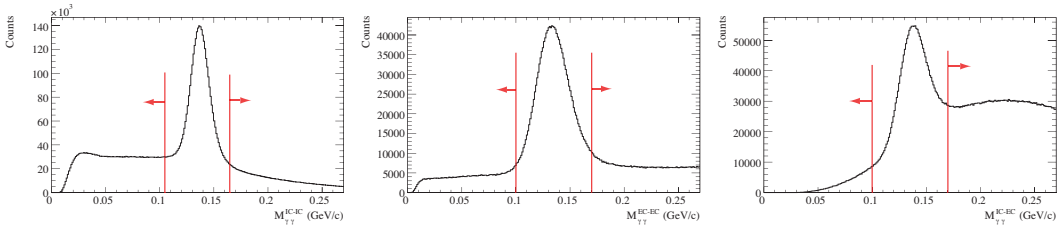

(a) IC-IC pion mass. (b) EC-EC pion mass. (c) IC-EC pion mass.

Figure 4.20: Neutral pion data cut. The red lines show the positions of the cuts applied.

Events containing one and only one good neutral pion were retained for the purposes of determining the background contribution from neutral pions in the exclusive electroproduction of photons data sample.

4.5.6 Event numbers

Table 4.1 lists the numbers of events remaining after successive particle ID cuts were applied. The cut numbers correspond to those of the particle in the corresponding row. Events in which multiples of the same particle passed the cuts were counted more than once. Proton numbers are given for events in which there was one and only one good electron. Photon numbers are quoted for events in which there was one and only one good electron, and one and only one good proton. For example in the column labelled cut 2 in the row for protons the value quoted is the number of particles that passed proton cuts one and two, for events containing one and only one particle passing all electron identification cuts.

Cut	1	2	3	4	5	6
Electron	1260	1180	1030	724	624	615
Proton	381	162	157	-	-	-
EC photon	56.0	46.7	38.2	34.2	-	-
IC photon	98.3	62.4	39.3	-	-	-

Table 4.1: Event numbers after successive particle ID cuts. Numbers quoted are in millions.

4.6 Exclusive Electroproduction of Hard Photons

The methods used to identify events corresponding to the exclusive electroproduction of hard photons will now be described. The sample of data used contained events with one and only one electron, one and only one proton and at least one photon with energy above 300 MeV. Events in which one or more neutral pions were identified were rejected from this part of the study. Events containing more than one photon were not discarded from the sample that the reaction identification cuts were applied to. This approach was motivated by the fact that there were few photon identification cuts which meant that some some photon candidate particles corresponded to random coincidences and removing events containing these particles would have resulted in a loss of many of the good events. The highest energy photon in each event was chosen as the reaction product. Reactions in which more than one photon was genuinely produced were rejected along with other background reactions using exclusive cuts.

4.7 Kinematic Cuts

Prior to applying exclusivity cuts, the following kinematic cuts were imposed:

1. $Q^2 > 1$ (GeV/c)^2 and $Q^2 > -t$. The first condition removed events that were not within the Bjorken scaling regime. The handbag approximation is valid for $Q^2 >> -t$. The second condition was imposed to minimise the contributions from higher twist effects, which are interesting in themselves but it was not the goal of this analysis to investigate them.

2. $W > 2$ GeV. There are strong contributions to the cross section from elastic scattering and scattering from proton resonances for events with $W < 2$ GeV. In this analysis only photon production on the proton ground state was of interest so this low-W region was rejected.

3. $E_\gamma > 1$ GeV. This condition was applied to reduce the size of the data set at this stage of the analysis. It is shown in the next section that it had no effect on the final sample. The top left panels of Figures 4.31 and 4.32 show photon energy distributions before and after the reaction identification cuts were applied. Events containing photons with energies less than 1 GeV would also have been removed by the reaction identification cuts.

4.7.1 Event numbers

Table 4.2 lists the numbers of events after successive kinematic cuts were applied to the sample of data remaining after all particle ID cuts were applied. In each event the highest energy photon was selected as the photon in the reaction of interest, which was either detected by the EC or the IC.

Cut	1	2	3
γ^{EC}	19.1	16.1	5.01
γ^{IC}	23.1	21.4	9.27

Table 4.2: Event numbers after successive kinematic cuts. Numbers are given in millions and quoted for events in which there was one and only one electron, one and only one proton and at least one photon with energy above 300 MeV and no neutral pions. Numbers in different rows correspond to events in which the highest energy photon was in either the EC (top) or the IC (bottom).

4.8 Exclusive Variables

This section explains how the exclusive variables were calculated from measured variables. The energy-momentum four-vectors for particles in hard photon reactions, $P_{beam} + P_{target} \rightarrow P_e + P_p + P_\gamma$, were defined:

$$\begin{aligned}
P_{beam} &= (0,0,E_{beam},E_{beam}), && \text{(electron beam);} \\
P_{target} &= (0,0,0,M_p), && \text{(proton target);} \\
P_e &= (c_x^e.p_e, c_y^e.p_e, c_z^e.p_e, p_e), && \text{(scattered electron);} \\
P_p &= (c_x^p.p_p, c_y^p.p_p, c_z^p.p_p, (p_p^2+M_p^2)^{1/2}), && \text{(recoil proton);} \\
P_\gamma &= (c_x^\gamma.E_\gamma, c_y^\gamma.E_\gamma, c_z^\gamma.E_\gamma, E_\gamma), && \text{(produced photon);}
\end{aligned} \tag{4.1}$$

where E_i (p_i) is the measured energy (momentum) of particle i, c_j^i is the corresponding particle direction cosine in the j direction, and M_p is the PDG value for proton mass.

Other four-vectors that were used were:

$$\begin{array}{lcll} P_{\gamma^*} & = & P_{beam} - P_e, & \text{(virtual photon);} \\ P_X^{ep\gamma} & = & P_{beam} + P_{target} - (P_e + P_p + P_\gamma), & \text{(reaction);} \\ P_X^{ep} & = & P_{beam} + P_{target} - (P_e + P_p), & \text{(reconstructed photon);} \\ P_X^{e\gamma} & = & P_{beam} + P_{target} - (P_e + P_\gamma), & \text{(reconstructed proton);} \end{array} \tag{4.2}$$

which were used to calculate missing masses:

$$\begin{array}{lcl} MM_X^2(ep\gamma) & = & (P_X^{ep\gamma})^2, \\ MM_X^2(ep) & = & (P_X^{ep})^2, \\ MM_X^2(e\gamma) & = & (P_X^{e\gamma})^2. \end{array} \tag{4.3}$$

The elements of

$$P_X^{ep\gamma} = (p_x^X, p_y^X, p_z^X, E^X); \tag{4.4}$$

are the missing momenta in three directions and the missing energy.

The total angle between the detected photon and the reconstructed photon was defined:

$$\theta_{\gamma X} = \cos^{-1}\left(\frac{\vec{P}_\gamma.\vec{P}_X^{ep}}{|\vec{P}_\gamma||\vec{P}_X^{ep}|}\right). \tag{4.5}$$

The hadron production plane contains the virtual photon, produced photon and recoil proton and can therefore be calculated in three unique ways:

$$\begin{array}{lcl} \vec{H}_1 & = & (\vec{P}_p \times \vec{P}_{\gamma^*}); \\ \vec{H}_2 & = & (\vec{P}_p \times \vec{P}_\gamma); \\ \vec{H}_3 & = & (\vec{P}_{\gamma^*} \times \vec{P}_\gamma); \end{array} \tag{4.6}$$

from which the difference in the cross section ϕ angle can be calculated in three unique ways. The most narrow distribution was used, which was found to be:

$$\begin{array}{lcll} \Delta\phi & = & \cos^{-1}\left(\frac{\vec{H}_1.\vec{H}_2}{|\vec{H}_1||\vec{H}_2|}\right) & \text{for} \quad \vec{H}_1.\vec{P}_\gamma \geq 0.0; \\ \Delta\phi & = & -\cos^{-1}\left(\frac{\vec{H}_1.\vec{H}_2}{|\vec{H}_1||\vec{H}_2|}\right) & \text{for} \quad \vec{H}_1.\vec{P}_\gamma < 0.0. \end{array} \tag{4.7}$$

4.9 Exclusive Event Selection

After the application of the particle identification and kinematic cuts, there were already clear peaks in some of the exclusive variable distributions which corresponded to the reaction of interest. Figures 4.21 and 4.22 show MM_X^2(ep) distributions at this stage of the analysis for parts A and B of the experiment respectively. In the top panels of both

figures, these distributions are shown on a wide scale so that the full ranges can be seen. The pure NH_3 sample consists of a combination of events on Nitrogen, and various other reactions that occurred on Hydrogen. The events that occurred on the Nitrogen part of the NH_3 target are represented by data acquired using a Carbon target, which have been scaled using relative integrated luminosities. After the subtraction of the scaled Carbon distributions it is evident that various other reactions still contribute to the sample. These reactions include the exclusive electroproduction of neutral pions, etas and rhos, which have squared-masses: $M^2_{\pi^0} = 0.0182$ (GeV/c^2)^2, $M^2_{\eta^0} = 0.300$ (GeV/c^2)^2 $M^2_{\rho} = 0.601$ (GeV/c^2)^2.

The neutral pion and photon production peaks are overlapping. This caused difficulties in determining the peak widths for exclusive variable distributions for photon events. Monte Carlo (MC) simulated exclusive electroproduction of photon events were used to help guide the choice of cut widths for the reaction identification part of the analysis. Details of the method used to produce Monte Carlo data are given in Section 4.12.

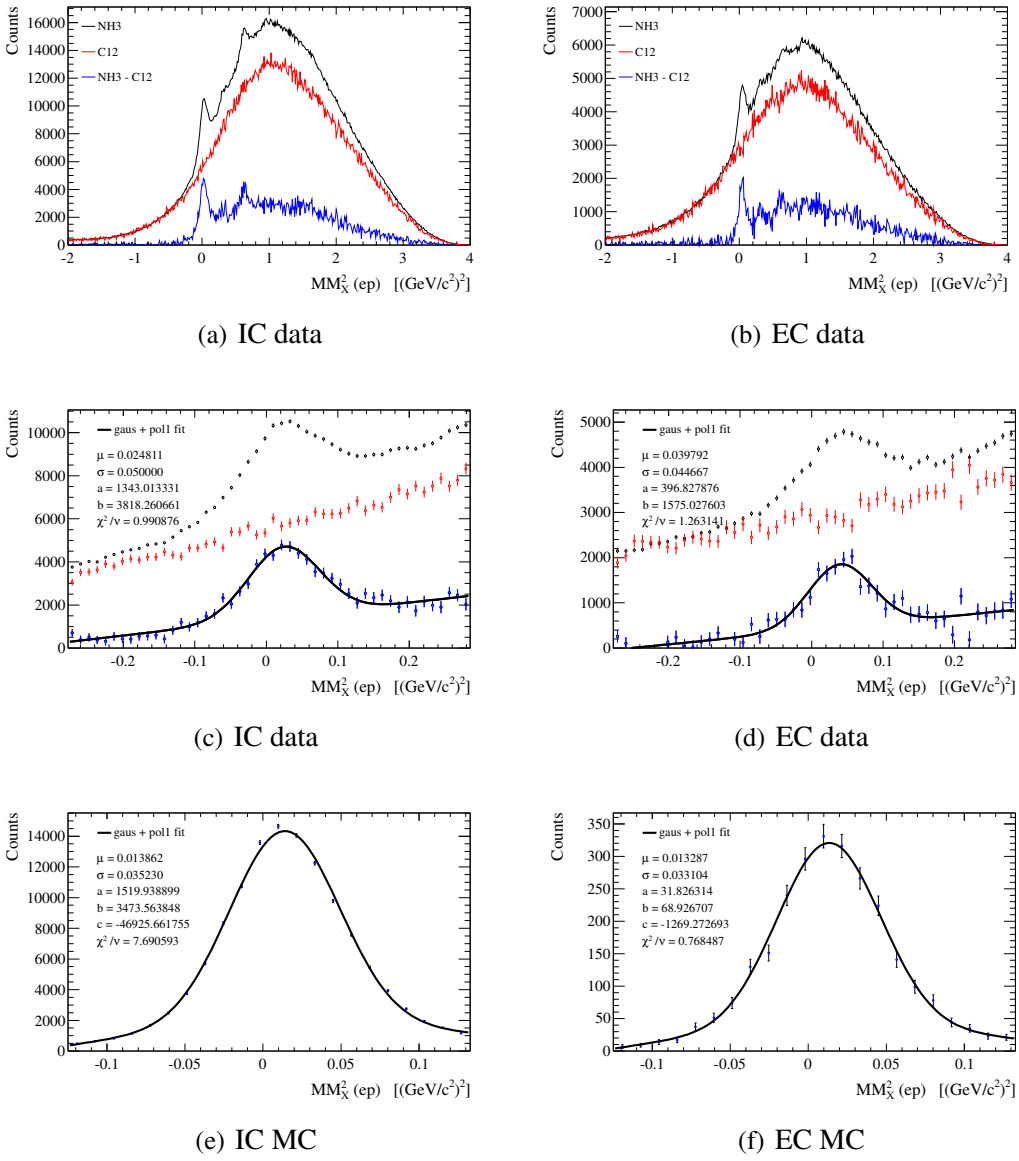

(a) IC data (b) EC data

(c) IC data (d) EC data

(e) IC MC (f) EC MC

Figure 4.21: MM_X^2(ep) for part A events. IC and EC photon event distributions are shown separately. The black (red) histograms are of data taken on NH_3 (Carbon) target. Carbon histograms were scaled using the relative integrated beam lumonisities. The blue histograms are of the NH_3 data minus the Carbon data. The bottom two plots are of Monte Carlo DVCS generated data. The x-axes for data and MC in the middle and bottom plots have not been plotted over the same ranges. Data distributions were plotted over a wider range to show the reaction background at either side of the peaks and wider function range used.

4.9.1 Missing mass cut

All other exclusive cut widths were determined after applying a cut to MM_X^2 (ep). Data from different experimental configurations were treated independently to investigate variations in the resolutions of exclusive variable peaks. Exclusive variables for some experimental configurations did not always have visible peaks until after applying the MM_X^2 (ep) cut. The cut widths were determined using MC simulated DVCS and BH events as a guide. Simulated events were subjected to the same analysis procedures as the data. This method allowed a consistent approach to be used for each subset of data, which was found to not be possible in all cases by basing the cuts on fits to the data.

In Figures 4.21 and 4.22 the middle panel plots are the same as the top panels but are shown over a more narrow range so that the region of interest can be seen clearly. These distributions have been fitted with a Gaussian distribution, with mean μ and width σ, plus a first order polynomial. Parameters representing coefficients for terms of increasing order in polynomial fits are given by increasing letters of the alphabet starting at a, which is the zeroth order coefficient (constant term). The Gaussian fits aim to represent the widths of exclusive electroproduction of photons reactions but are broader than the MC data. This may be due to the contribution from neutral pion production events and/or because detector noise contributions were not fully represented in the MC simulation. The first order polynomial part of the fits aim to represent the combined background. Other Gaussian plus higher order polynomial fits were attempted on the experimental data, but no improvement was found for the goodness of fit parameter: χ^2/ν, where ν is the number of degrees of freedom - see Chapter 5 for a definition of the goodness of fit parameter.

The bottom panels in the same figures show MC data which has been fitted with a Gaussian plus second order polynomial. The fit range has been reduced for these distributions in order to obtain a good measure of the peak width but still covers more than 3-σ either side of the mean, which in general was taken as the minimum acceptable fit range. For these distributions, it was necessary to include a second-order polynomial to represent the tails of the main distributions well, which were found to fall off less sharply than a Gaussian. This suggests that they are caused by radiative effects, which may also be the reason for the peaks not being centred exactly on zero. The cut width applied was taken as a fixed value, $|MM_X^2| < 0.12$ (GeV/c^2)^2, for all experimental configurations. This is slightly larger than the 3-σ value from the simulated data fits but since the data were found in general to have wider distributions this was considered to be reasonable, and was also consistent with the width used in the previous CLAS target spin asymmetry analysis [76]. The aim of the reaction identification cuts was to maximise the number of photon production events and minimise the contributions from the neutral pion produc-

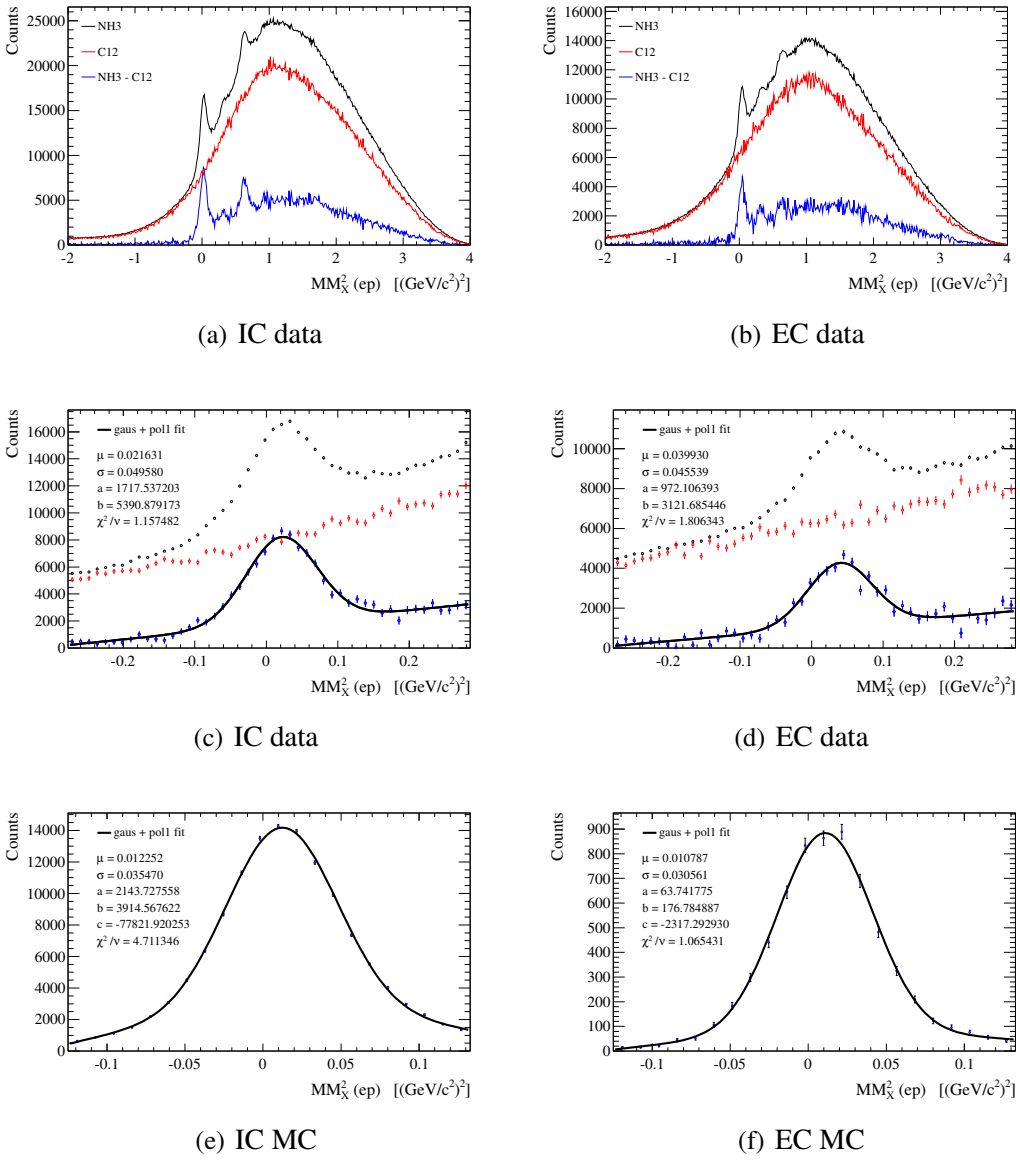

(a) IC data (b) EC data

(c) IC data (d) EC data

(e) IC MC (f) EC MC

Figure 4.22: MM_X^2(ep) for part B events. IC and EC photon event distributions are shown separately. The black (red) histograms are of data taken on NH_3 (Carbon) target. Carbon histograms were scaled using the relative integrated beam lumonisities. The blue histograms are of the NH_3 data minus the Carbon data. The bottom two plots are of Monte Carlo DVCS generated data. The x-axes for data and MC in the middle and bottom plots have not been plotted over the same ranges. Data distributions were plotted over a wider range to show the reaction background at either side of the peaks and wider function range used.

tion channel and events on the nitrogen part of the target. It was not to deemed possible to obtain a sample of pure photon production events.

4.9.2 Hadron production plane matching cut

For good photon production events, the $\Delta\phi$ angle is expected to be sharply peaked around zero because the produced photon must lie in the same plane as the virtual photon and recoil proton. For events in which other particles were produced and a photon was detected from their decay, this photon need not lie in the same plane as the virtual photon and proton. This means that the $\Delta\phi$ angle may take larger values for other reactions. Figures 4.23 and 4.24 show $\Delta\phi$ distributions after particle ID, kinematic cuts and the cut on MM_X^2(ep). The width for IC photon events for part B events is most similar to the MC distribution. The Part B IC data set has the largest number of events. The EC event data distribution fit widths are around four times larger than the MC data. This is likely due to there being a larger background contribution for EC events, although there may be some contribution from the simulation not representing the EC resolutions well. As a conservative approach, the philosophy adopted here was to base the EC cut closer to the more narrow MC distributions. A fixed value of $|\Delta\phi| < 1.2^\circ$ was used, which is consistent with approximately 4-σ for both parts of the experiment and EC and IC events for the MC data.

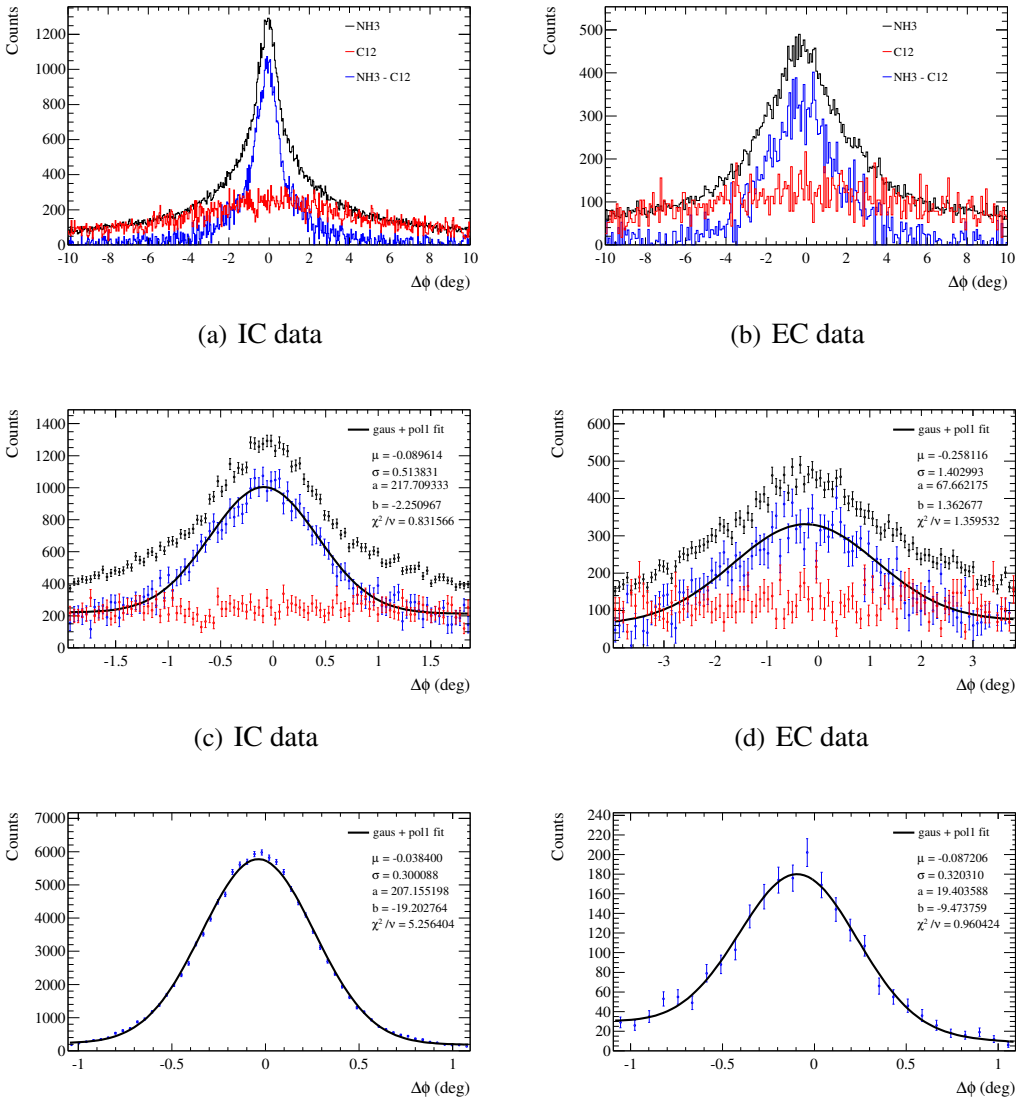

(a) IC data (b) EC data

(c) IC data (d) EC data

(e) IC MC (f) EC MC

Figure 4.23: $\Delta\phi$ for part A events. The plots are laid out in the same way as Figure 4.21 but (c)-(f) are plotted after the cut on MM_X^2(ep). Note the wider x-axis range in (d) compared to (c). For plots with fits, the ranges covered on the x-axes indicate the range used for the fit function.

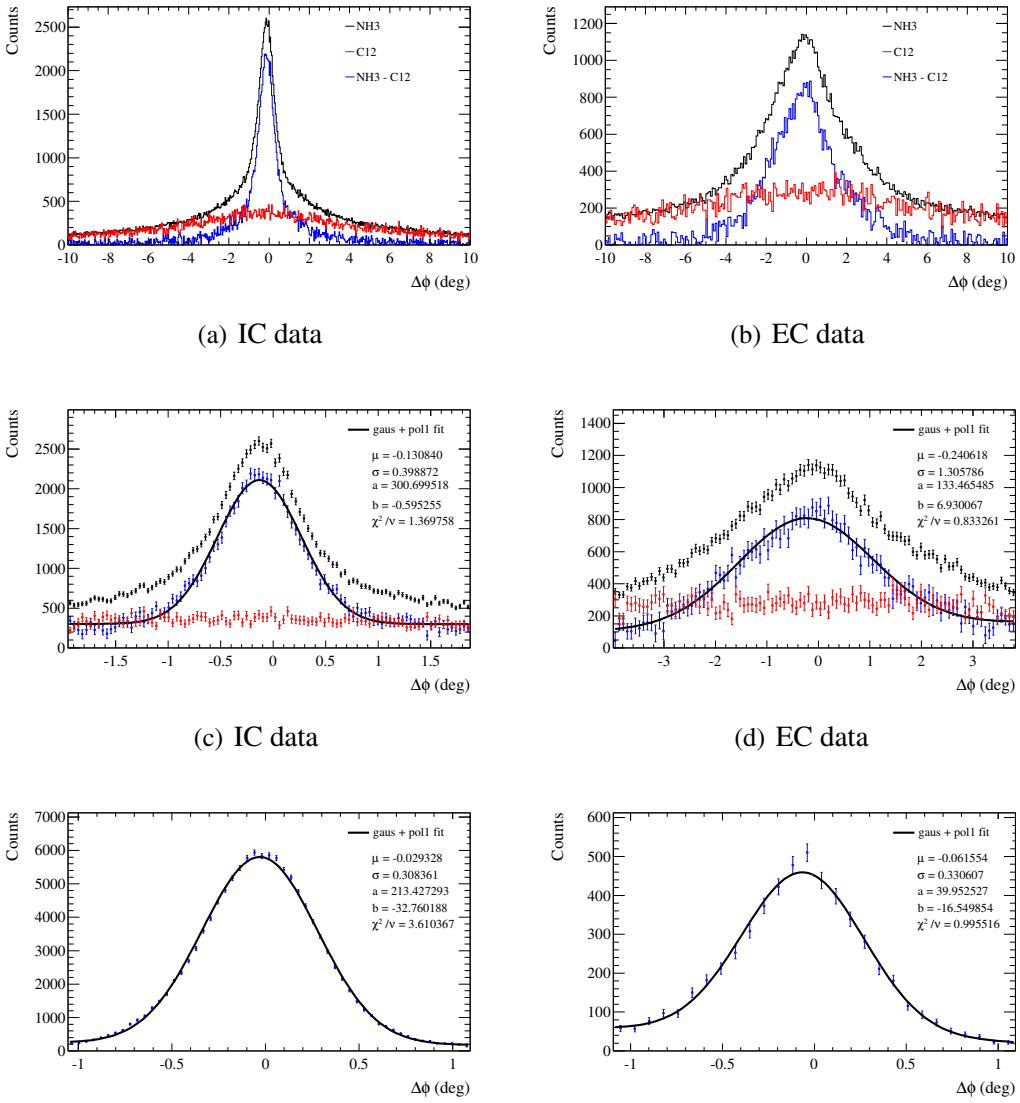

(a) IC data (b) EC data

(c) IC data (d) EC data

(e) IC MC (f) EC MC

Figure 4.24: $\Delta\phi$ for part B events. The plots are laid out in the same way as Figure 4.23. For plots with fits, the ranges covered on the x-axes indicate the range used for the fit function.

4.9.3 Photon angular matching cut

The four-vectors of the electron and proton from before and after the reaction were used to reconstruct the expected trajectory of the produced photon. The total angle between the true photon and the reconstructed photon directions should ideally be zero. In the case where some other reaction occurred, this angle can take large values. Figures 4.25 and 4.26 show histograms of this angle plotted after particle ID and kinematic cuts and the cut on $MM_X^2(\mathrm{ep})$. The distributions drop towards zero as $\theta_{\gamma X} \to 0$, which is a result of the fact that the solid angular coverage for each $\theta_{\gamma X}$ bin reduces with $\theta_{\gamma X}$. In the same figure there are plots of these same distributions that have been weighted by the relative solid angle per bin. In this case the data and MC distributions peak at zero. The fit function used for the weighted histograms was a half-Gaussian plus a first-order polynomial. The widths for IC and EC MC data differ by around 25 %, which is not unexpected as the resolutions of the IC and EC are not the same. Two different cut values were therefore adopted, which approximate to 5-σ from the MC fits: $\theta_{\gamma X}^{IC} < 1.0^\circ$ and $\theta_{\gamma X}^{EC} < 1.25^\circ$.

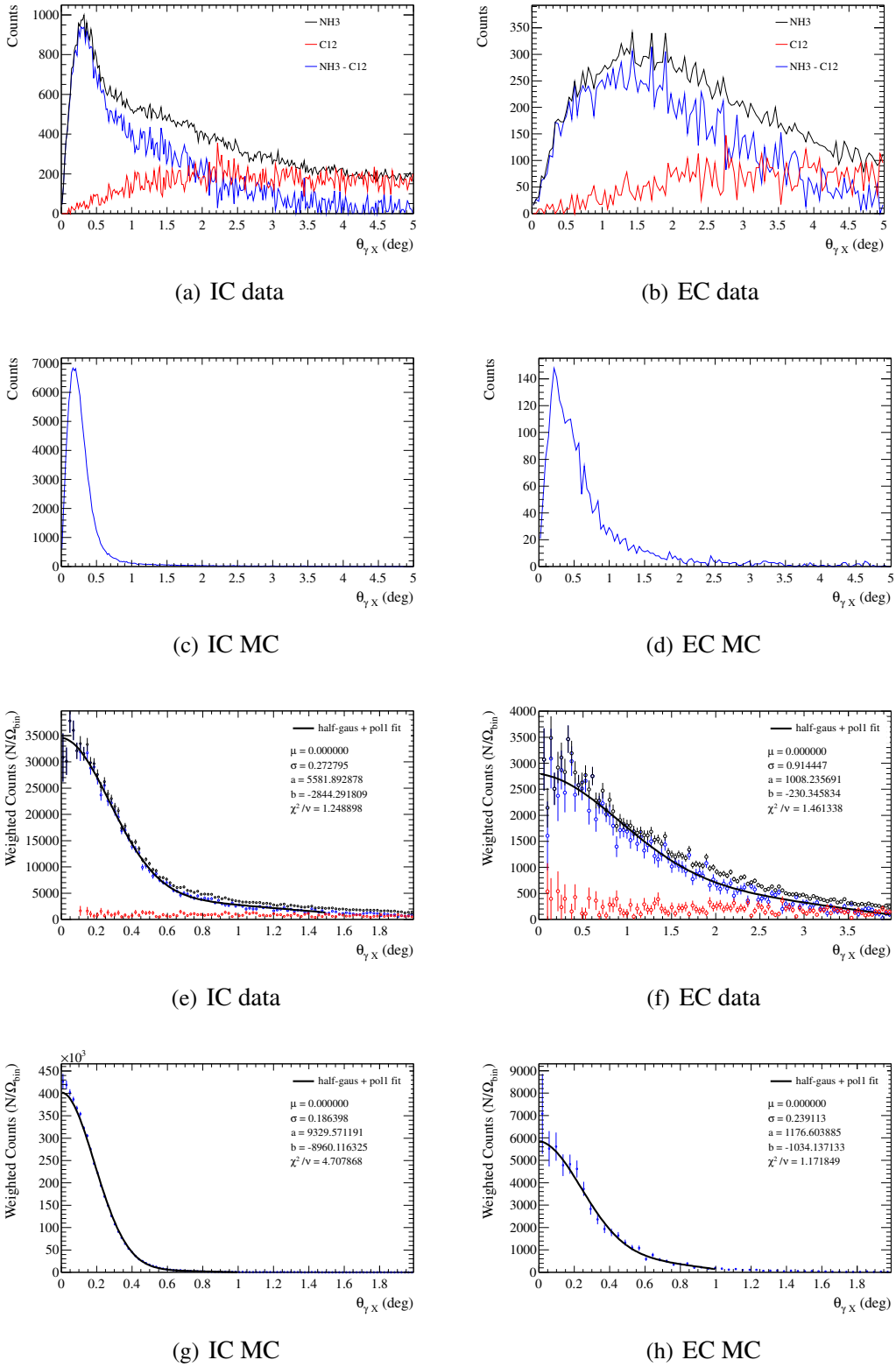

(a) IC data (b) EC data

(c) IC MC (d) EC MC

(e) IC data (f) EC data

(g) IC MC (h) EC MC

Figure 4.25: $\theta_{\gamma X}$ for part A events. The top (bottom) four plots were made before (after) the cut on $MM_X^2(ep)$. The number of counts per bin falls off at small values of $\theta_{\gamma X}$ in (a) and (b) due to the solid angle coverage per bin reducing with $\theta_{\gamma X}$. The distributions in (c)-(f) were weighted by the relative solid angle per bin, which has resulted in a reasonably flat background from Nitrogen events and a strong peak for photon production events. Plots (c), (d), (g) and (h) are of Monte Carlo generated data. For plots with fits, the ranges covered on the x-axes indicate the range used for the fit function.

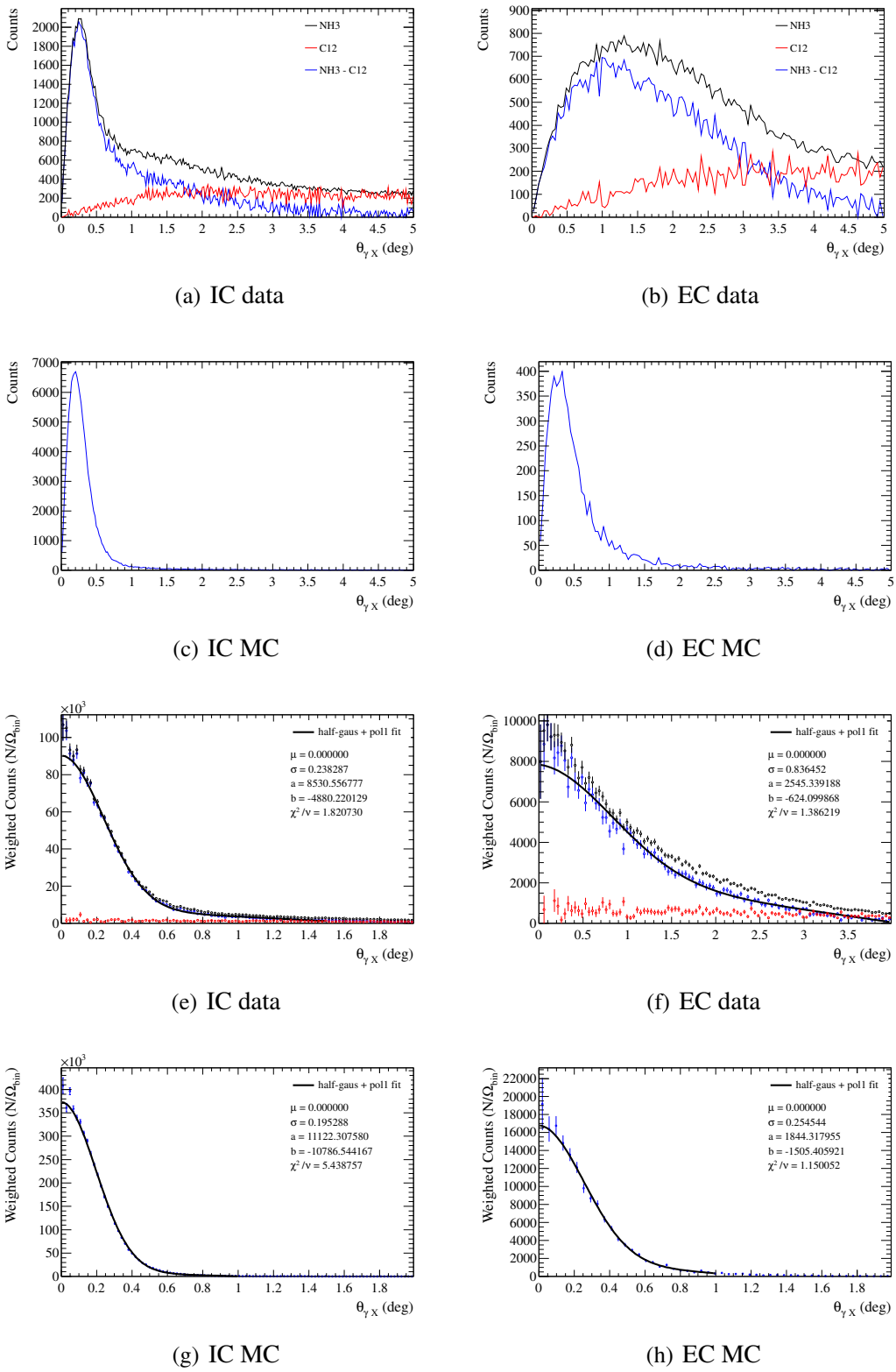

(a) IC data (b) EC data

(c) IC MC (d) EC MC

(e) IC data (f) EC data

(g) IC MC (h) EC MC

Figure 4.26: $\theta_{\gamma X}$ for part B events. The plots are are laid out in the same way as in Figure 4.25. For plots with fits, the ranges covered on the x-axes indicate the range used for the fit function.

4.9.4 Missing perpendicular momentum cut

The components of the reaction four-vector are the missing momenta in three directions and the missing energy, which should each be distributed around zero for well reconstructed photon production events. The strategy adopted here was to develop cuts based on the missing perpendicular momentum components p_x^X and p_y^X and check the other components after all the other cuts. Figures 4.27, 4.28, 4.29 and 4.30 show histograms of these missing perpendicular momentum components after the particle ID, kinematic and missing mass cuts. Different cuts were used for IC and EC events to reflect the different resolutions. These cuts were imposed on the total perpendicular missing momentum $p_\perp = \sqrt{(p_x^X)^2 + (p_y^X)^2}$, and are consistent with approximately 4-σ from the MC fits: $p_\perp^{IC} < 0.06, p_\perp^{EC} < 0.14$

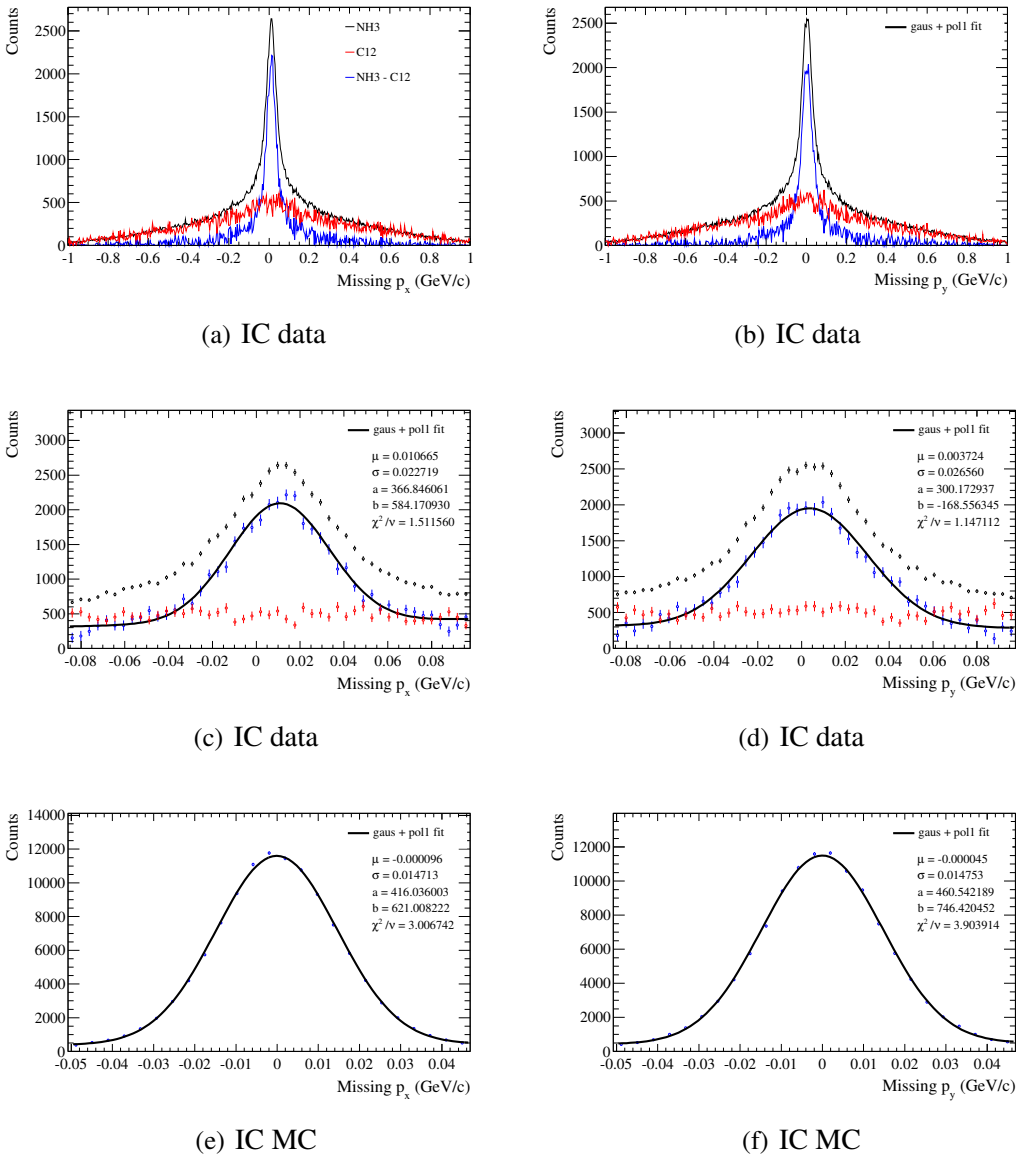

(a) IC data (b) IC data

(c) IC data (d) IC data

(e) IC MC (f) IC MC

Figure 4.27: Missing perpendicular momenta: p_x^X (LHS) and p_y^X (RHS) for part A IC photon events. The black (red) histogram is of data taken on NH_3 (Carbon) target. Carbon histograms were scaled using the relative integrated beam luminosities. The blue histograms are of the NH_3 data minus the Carbon data. The bottom two plots are of Monte Carlo DVCS generated data. For plots with fits, the ranges covered on the x-axes indicate the range used for the fit function.

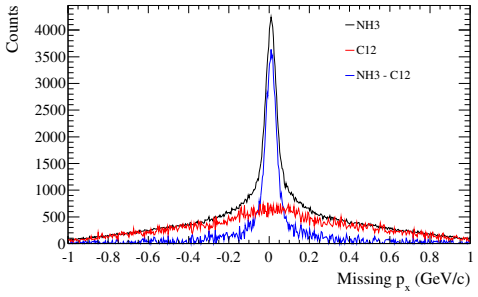

(a) IC data

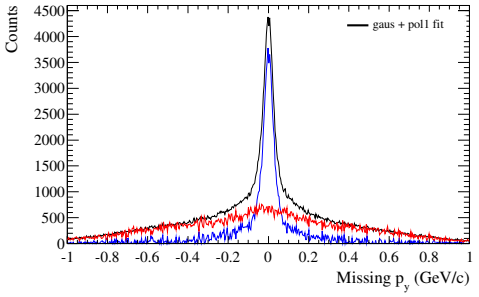

(b) IC data

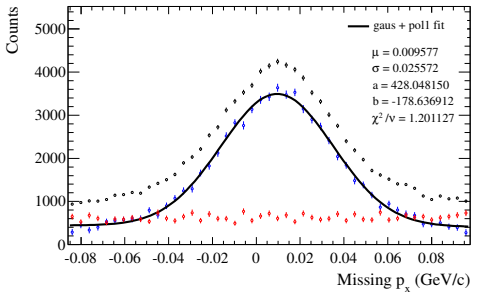

(c) IC data

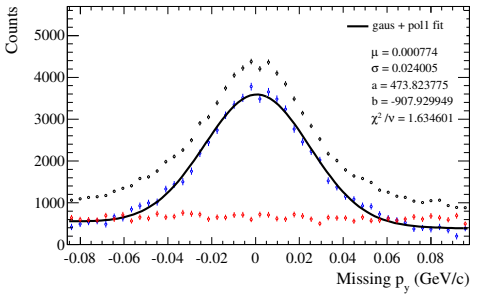

(d) IC data

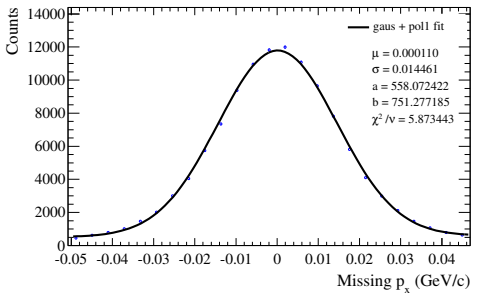

(e) IC MC

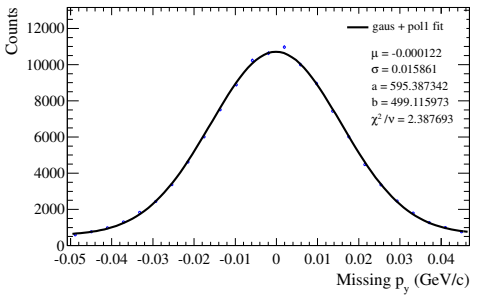

(f) IC MC

Figure 4.28: Missing perpendicular momenta: p_x^X (LHS) and p_y^X (RHS) for part B IC photon events. Plots are laid out in the same way as in Figure 4.27. For plots with fits, the ranges covered on the x-axes indicate the range used for the fit function.

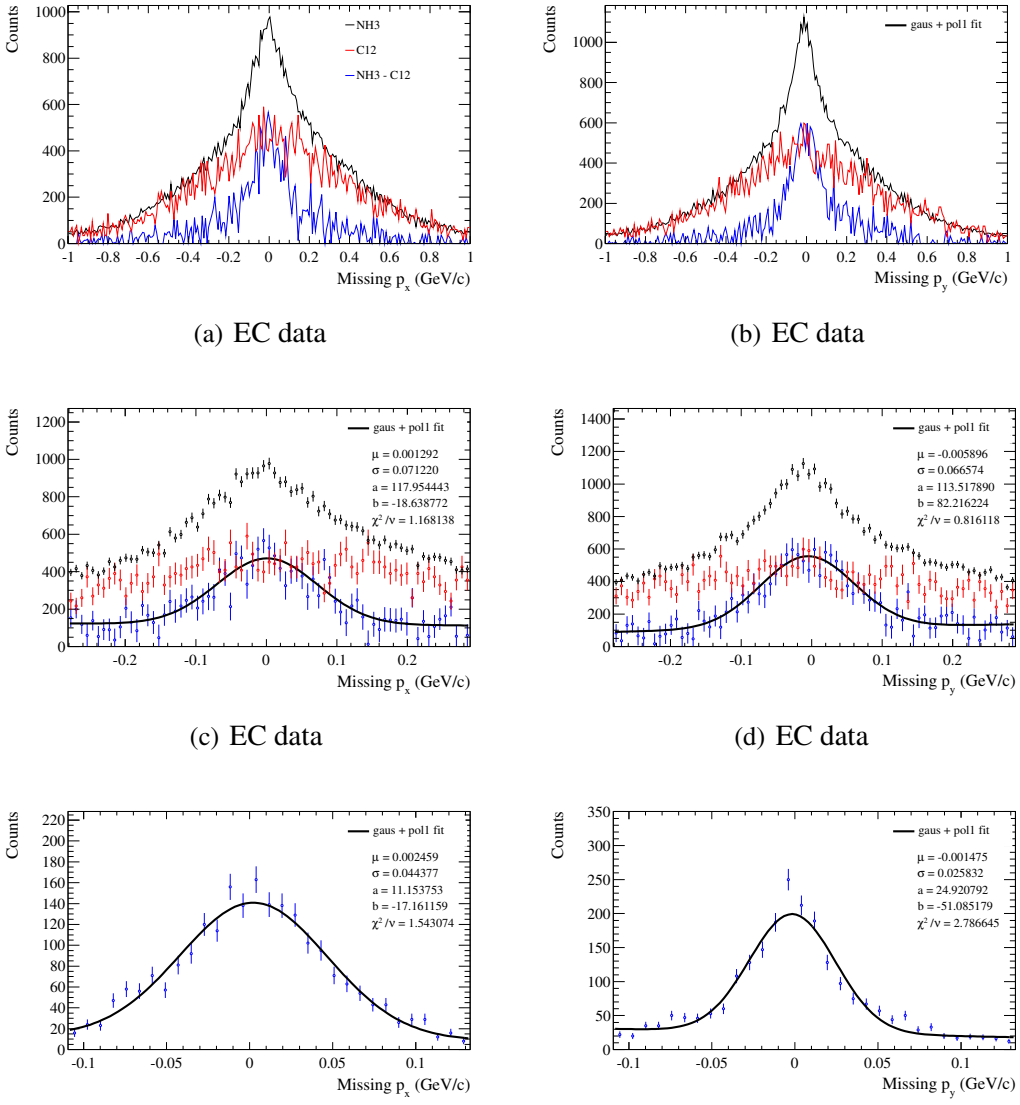

(a) EC data (b) EC data

(c) EC data (d) EC data

(e) EC MC (f) EC MC

Figure 4.29: Missing perpendicular momenta: p_x^X (LHS) and p_y^X (RHS) for part A EC photon events. Plots are laid out in the same way as in Figure 4.27. For plots with fits, the ranges covered on the x-axes indicate the range used for the fit function.

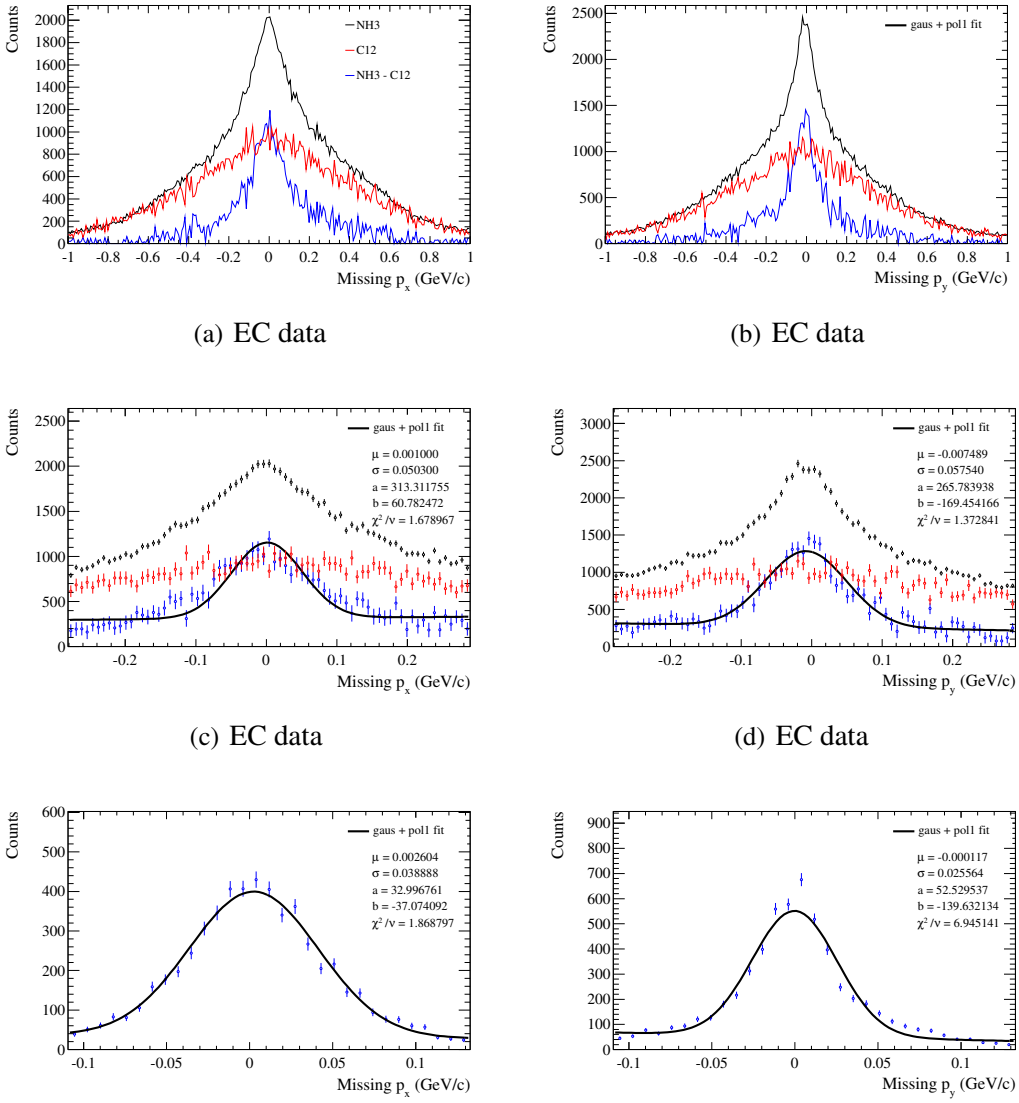

(a) EC data (b) EC data

(c) EC data (d) EC data

(e) EC MC (f) EC MC

Figure 4.30: Missing perpendicular momenta: p_x^X (LHS) and p_y^X (RHS) for part B EC photon events. Plots are laid out in the same way as in Figure 4.27. For plots with fits, the ranges covered on the x-axes indicate the range used for the fit function.

4.9.5 Other exclusive variables

The effects of the exclusive cuts described above on other exclusive variable distributions are shown in Figures 4.31 and 4.32. Only part B data distributions are shown. The distributions for part A were very similar. The top panel plots show that the distribution of events with small photon energies were dominated by events with large missing energy values. This illustrates that minimum photon energy cut at 1 GeV mainly removed background events. Table 4.3 lists all of the reaction identification cuts for photon production events.

cut	variable	condition	units
1	$\lvert MM_X^2(ep)\rvert$	< 0.12	$(\mathrm{GeV/c^2})^2$
2	$\Delta\phi$	< 1.2	(deg)
3	$\theta_{\gamma X}^{IC,EC}$	$< 1.0, 1.25$	(deg)
4	$p_\perp^{IC,EC}$	$< 0.06, 0.14$	(GeV/c)

Table 4.3: Cut widths for exclusive variables for photon production events.

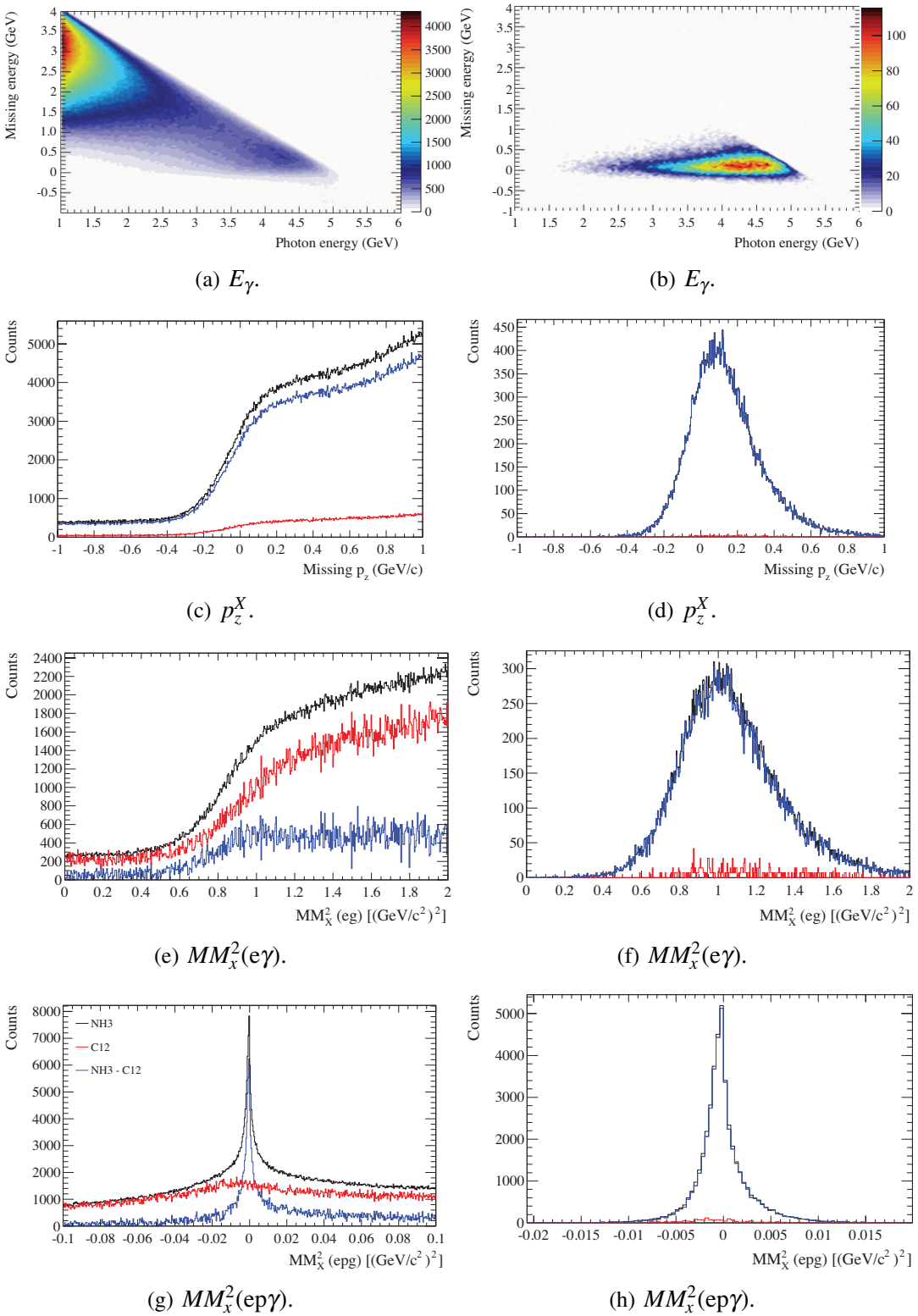

(a) E_γ. (b) E_γ.

(c) p_z^X. (d) p_z^X.

(e) $MM_x^2(e\gamma)$. (f) $MM_x^2(e\gamma)$.

(g) $MM_x^2(ep\gamma)$. (h) $MM_x^2(ep\gamma)$.

Figure 4.31: Distributions of other exclusive variables before (LHS) and after (RHS) the application of exclusive cuts for part B IC photon events. No data cuts were applied to these variables in the event selection process.

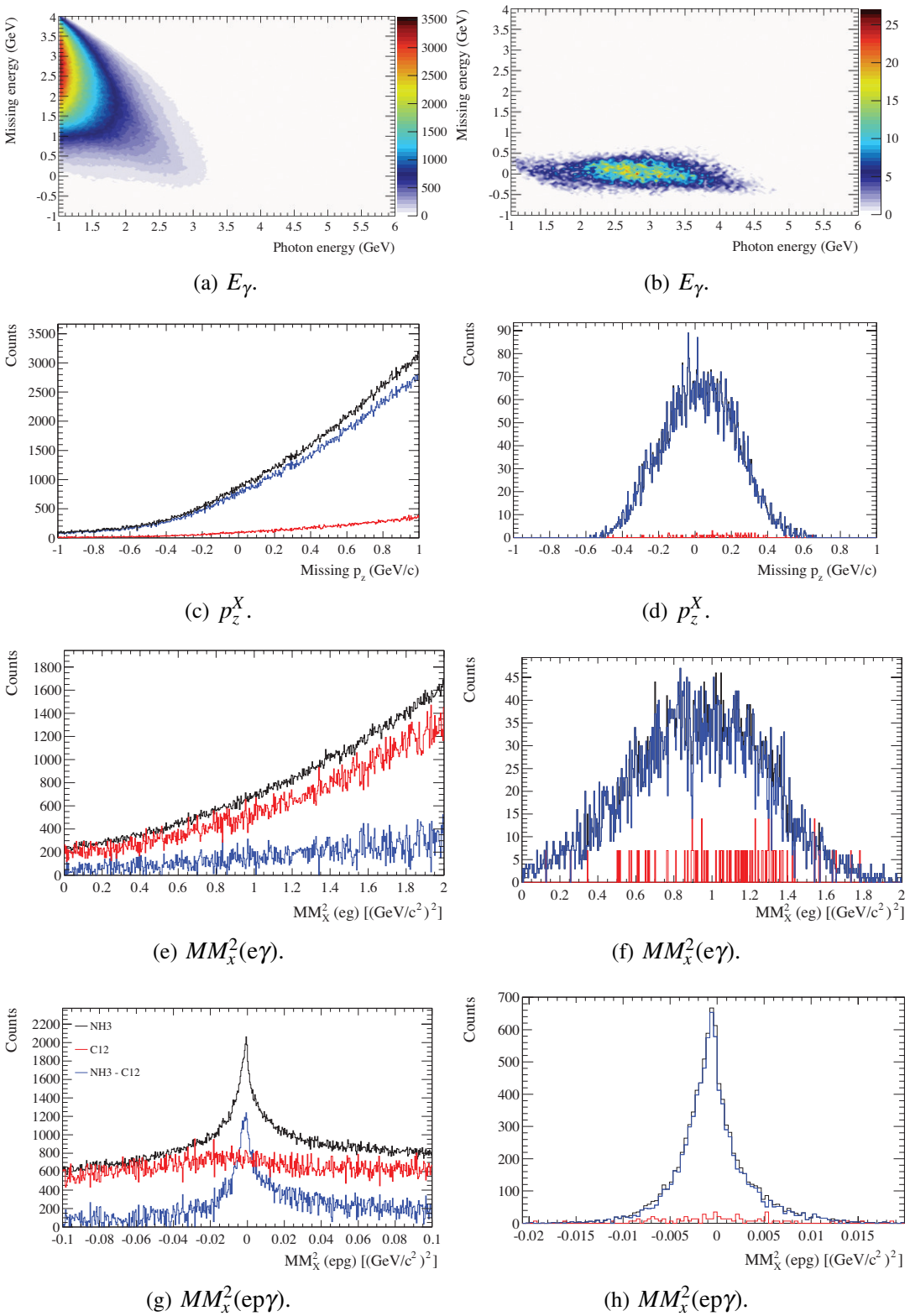

(a) E_γ. (b) E_γ.

(c) p_z^X. (d) p_z^X.

(e) $MM_x^2(e\gamma)$. (f) $MM_x^2(e\gamma)$.

(g) $MM_x^2(ep\gamma)$. (h) $MM_x^2(ep\gamma)$.

Figure 4.32: Distributions of other exclusive variables before (LHS) and after (RHS) the application of exclusive cuts for part B EC photon events.

4.10 Exclusive Electroproduction of Neutral Pions

The selection of exclusive electroproduction of neutral pion events followed similar methods as the selection of exclusive electroproduction of photon events. Exclusive variables for pion production events were created using the same construction of four-vectors except that the photon four-vector was replaced by a four-vector for the pion, which was recontructed using the two detected photons:

$$P_{\pi^0} = P_{\gamma_1} + P_{\gamma_2}. \tag{4.8}$$

The cuts used to identify exclusive electroproduction of neutral pion reactions are given in Table 4.4. Figure 4.33 shows exclusive variable distributions for pion events before and after these cuts were applied.

variable	condition	units
$\lvert MM_X^2(ep) - M_{\pi^0}^2 \rvert$	< 0.12	$(\mathrm{GeV/c^2})^2$
$\theta_{\pi^0 X}$	< 1.5	(deg)
$p_\perp$	< 0.1	$(\mathrm{GeV/c^2})$
$\Delta\phi$	< 1.2	(deg)

Table 4.4: Cut widths for exclusive variables for all pion production events.

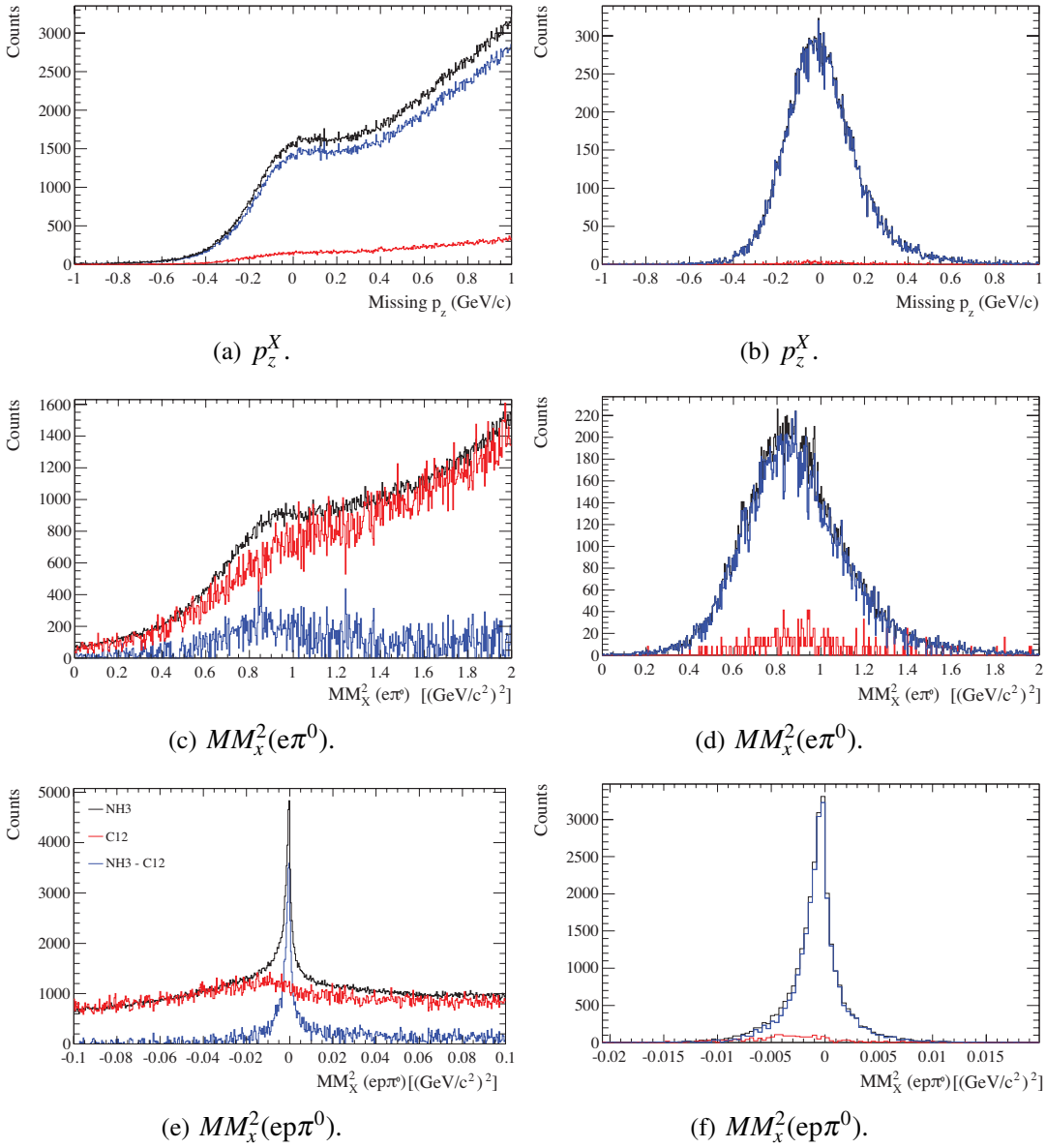

(a) p_z^X. (b) p_z^X.

(c) $MM_x^2(e\pi^0)$. (d) $MM_x^2(e\pi^0)$.

(e) $MM_x^2(ep\pi^0)$. (f) $MM_x^2(ep\pi^0)$.

Figure 4.33: Distributions of other exclusive variables before (LHS) and after (RHS) the application of exclusive cuts for all pion production events.

4.11 Kinematic Coverages

The distributions of the final event samples in terms of the kinematic variables Q^2, xB, $-t$ and ϕ for photon production and pion production events are shown in Figure 4.34. Table 4.5 lists the average values for the variables Q^2, xB and $-t$.

	photons	pions
$< -t > (GeV/c)^2$	0.49	0.64
$< Q^2 > (GeV/c)^2$	2.41	2.44
$< x_B >$	0.31	0.33

Table 4.5: Average kinematics for the final data sets for photon (LHS) and pion (RHS) production events.

4.11.1 Event numbers

Table 4.6 lists the number of events remaining after successive reaction ID cuts were applied. There were over two and a half times as many photon production events than neutral pion production events.

Cut	1	2	3	4
Photons	548	148	97	74
Pions	201	48	36	27

Table 4.6: Event numbers after successive reaction ID cuts. Numbers quoted are in thousands.

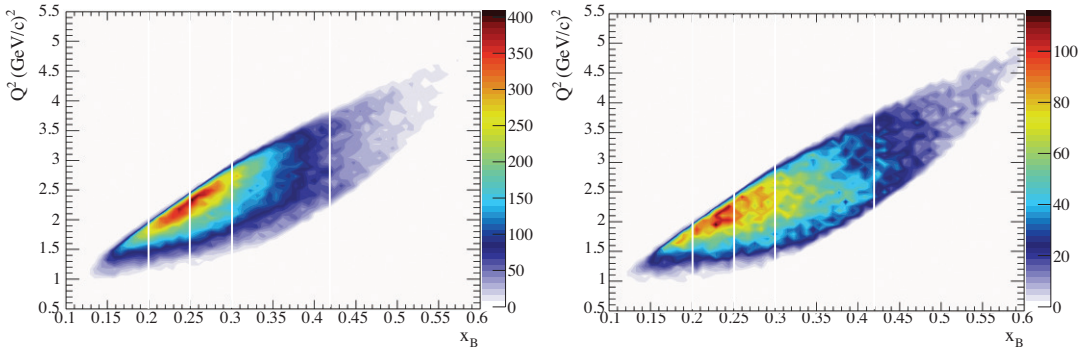

(a) Q^2 vs x_B for photon events.

(b) Q^2 vs x_B for π^0 events.

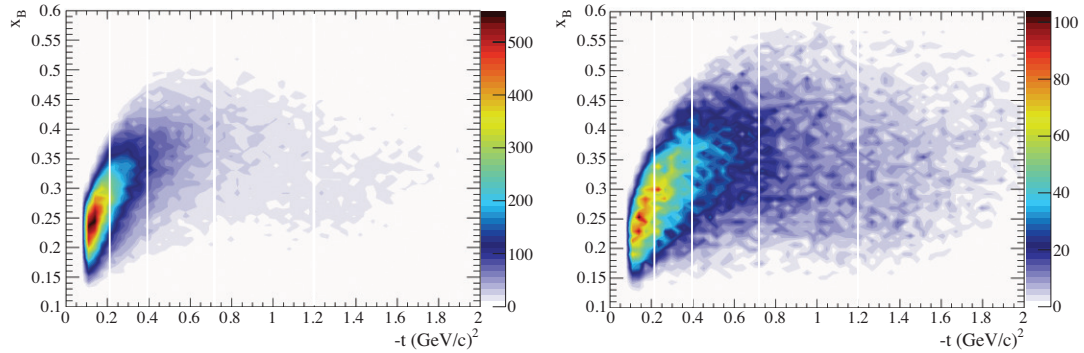

(c) x_B vs $-t$ for photon events.

(d) x_B vs $-t$ for π^0 events.

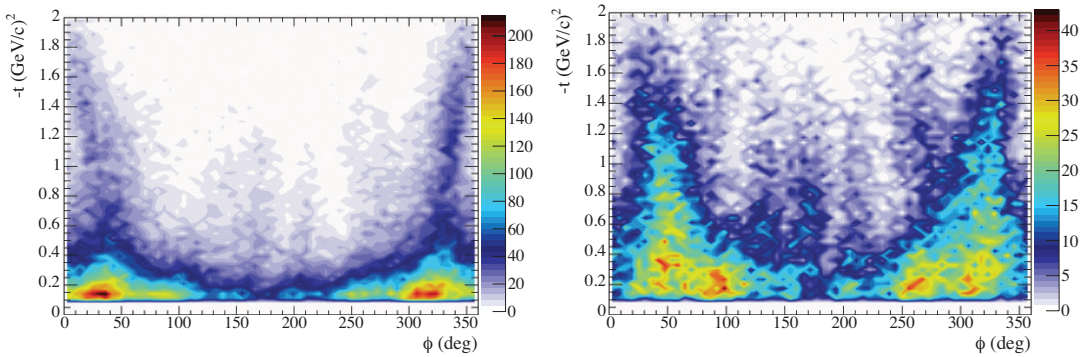

(e) $-t$ vs ϕ for photon events.

(f) $-t$ vs ϕ for π^0 events.

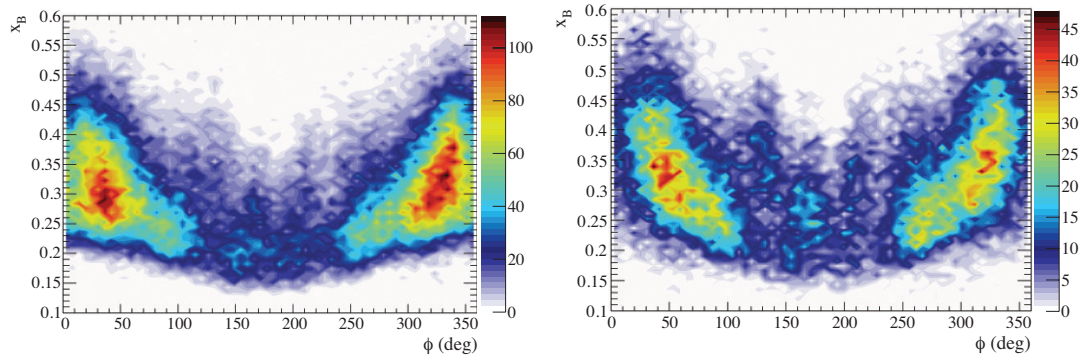

(g) x_B vs ϕ for photon events.

(h) x_B vs ϕ for π^0 events.

Figure 4.34: Kinematic coverages for the final data sets for photon (LHS) and pion (RHS) production events. In plots (a), (b), (c) and (d) the white lines indicate the edges of the bins used for the asymmetry analysis.

4.12 Monte Carlo Simulation

Monte Carlo (MC) simulations were used in this analysis for the purposes of: optimising exclusive variable cut widths, performing angular and momentum corrections for electrons and protons, and quantifying the level of neutral pion production contamination. As already mentioned, the procedure used for quantifying the level of neutral pion production contamination will be explained in the next Chapter. Angular and momentum corrections were adopted from the work in [99]. Two MC generators were used:

1. Exclusive electroproduction of photons: DVCS and BH events were generated using a code called *dvcsgen* [100], which is based on code written by V. Kortkov [101] and follows the formalism in [57].

2. Exclusive electroproduction of neutral pions: $ep\pi^0$ events were generated using a code called *aoo_rad* [102], which was modified to match the experimental cross section measurements in [103].

The outputs from these generators were fed into a GEANT3 [104] simulation of the CLAS detector system. The standard version of this simulation, called GSIM, was modified by S. Niccolai [105] to account for the specific EG1DVCS experimental setup. Two configuration files were used to represent the different target locations and shielding variations of parts A and B of the experiment. The outputs from these versions of GSIM were sent through a program called GPP, which was used to simulate the Drift Chamber efficiencies and smear the data according to the Drift Chamber resolutions. The MC data were then treated in the same way as the experimental data. Figure 4.35 shows plots of the main kinematic variable distributions for real and MC data for the final photon production event sample.

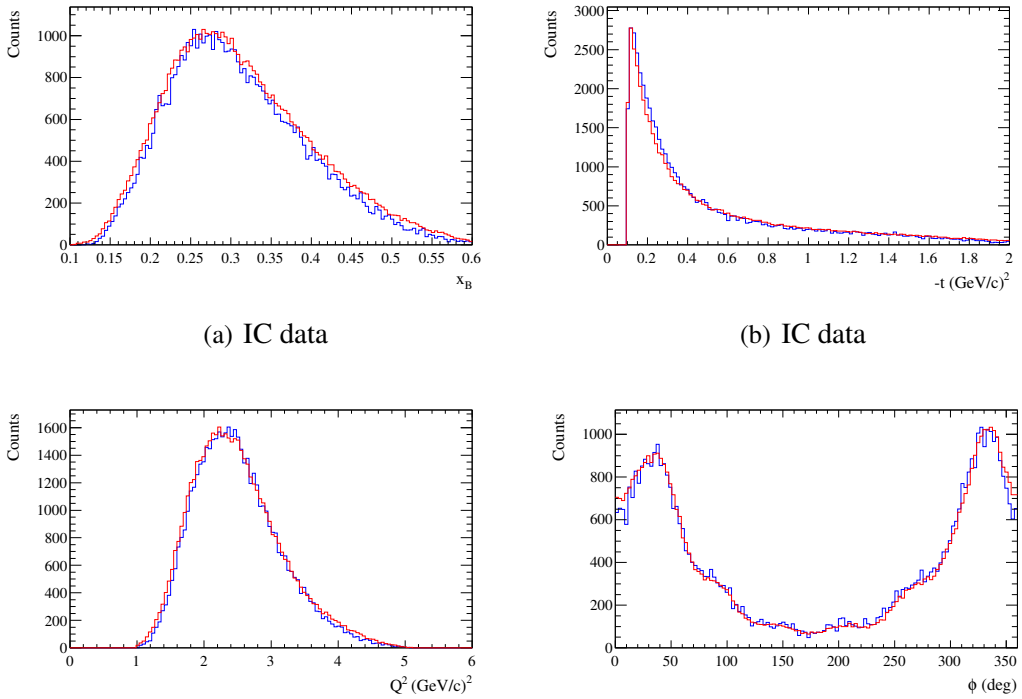

(a) IC data

(b) IC data

(c) IC data

(d) IC data

Figure 4.35: Comparison of MC data to real data for the kinematic variables x_B, $-t$, Q^2 and ϕ for IC photon events after all data cuts were applied. MC data distributions were scaled to the data using the relative values in the bins containing the maximum number of counts.

4.13 Summary

In this chapter the methods used to select DVCS candidate events from data recorded during the EG1DVCS experiment were described. On an event-by-event basis this reaction could not be completely isolated from the exclusive electroproduction of neutral pions reaction for the case in which only one photon from the neutral pion decay was detected. This background reaction was also therefore identified for the purposes of background subtraction, by selecting a sample of events in which the exclusive electroproduction of neutral pions was identified. The next chapter deals with how these two event samples are used to extract results that can be used to obtain information about proton structure.

Chapter 5

Analysis 2 - Proton Spin Asymmetries

In Chapter 2 it was shown that Compton form factors are experimentally observable quantities and relate directly to Generalised Parton Distributions. The connection between them and the ϕ-harmonic amplitudes of spin asymmetries for the exclusive electroproduction of photons was also explained. This chapter is dedicated to discussing the means by which the final asymmetry amplitudes of this analysis were determined, which involved performing fits to the samples of data that were selected by the methods described in the previous chapter.

Two different methods of fitting were carried out. To begin with the Least-Squares fitting method will be discussed. This is perhaps the most common method of parameter determination and will likely be known to the reader. Describing the Least-Squares method first is intended to provide a familiar starting point from which to move on to a discussion of the perhaps less-well-known but more widely applicable Maximum Likelihood (ML) method. The ML method was used to determine the final asymmetry amplitudes in this work.

5.1 Least-Squares Fitting

The purpose of parameter determination is to test data against a hypothesis. A series of data $(x_i, y_i \pm \sigma_{y_i})$ is fitted with a theoretical curve $y(s_n)$, with n fit parameters s_n, yielding a prediction for y at every x_i [106]. This method can be used for example to fit a finite Fourier series,

$$f(s_n) = \sum_{n_{min}}^{n_{max}} s_n \sin(n\phi), \tag{5.1}$$

to a spin asymmetry:

$$A(\phi_i) = \frac{N_i^{\rightarrow} - N_i^{\leftarrow}}{N_i^{\rightarrow} + N_i^{\leftarrow}}; \tag{5.2}$$

where $N_i^{\rightarrow}$ ($N_i^{\leftarrow}$) is the number of counts with positive (negative) helicity in ϕ-bin i. A feature of the Least-Squares method is that the errors, σ_{y_i}, must be normally distributed [107]. In counting experiments, errors are Poisson-distributed and calculated using the number of counts in each bin: $\sigma_{N_i} = \sqrt{N_i}$. Conveniently, for the situation where the number of counts is large, a Poisson distribution is equivalent to a Normal distribution with mean N_i and sigma $\sqrt{N_i}$ [106]. This means that for ϕ-bins in which a large number of measurements are made, the errors are properly calculated. On the other hand, when only a few measurements are made in a given bin, the error on the number of counts follows the wrong probability density function for the use of the Least-Squares fitting method. In [106] the number is 5 is suggested as being sufficiently large.

Propagation of the errors on the number of counts yields:

$$\sigma_{A_i} \equiv \sigma_i = 2\frac{(N_i^{\rightarrow}N_i^{\leftarrow})^{1/2}}{(N_i^{\rightarrow}+N_i^{\leftarrow})^{3/2}} \tag{5.3}$$

as the error on $A(\phi_i)$; assuming that the errors are uncorrelated. Keep in mind that σ_i is the error on the asymmetry value in bin-i and not on the number of counts. When the errors are known, as in the example given, the weighted sum of squares,

$$S = \sum_i^M \left(\frac{f(s_n)_i - A(\phi_i)}{\sigma_i}\right)^2, \tag{5.4}$$

where M is the number of data points (or bins), is usually preferred over the un-weighted sum of squares case; which is the same formula as above but with $\sigma_i = 1$. The weighted sum of squares is minimised by finding the turning points with respect to the parameters:

$$\frac{\partial S}{\partial s_n} = \frac{\partial}{\partial s_n}\left(\sum_i^M \left(\frac{f(s_n)_i - A(\phi_i)}{\sigma_i}\right)^2\right) = 0. \tag{5.5}$$

Taking as an example the simple case in which the hypothesis predicts that there is only a $\sin(\phi)$ harmonic, the condition:

$$\frac{1}{2}\frac{\partial S}{\partial s_1} = \sum_i^M \left(\frac{s_1 sin^2(\phi_i) - A(\phi_i)sin(\phi_i)}{\sigma_i^2}\right) = 0, \tag{5.6}$$

gives the best estimate of the single parameter s_1. Solving for s_1 yields:

$$s_1 = \frac{[A(\phi)\sin(\phi)]}{[\sin^2(\phi)]}; \tag{5.7}$$

where the notation:

$$[f] = \sum_i^M \frac{f_i}{\sigma_i^2}, \tag{5.8}$$

has been used to make the equation compact. It is worth noting that using the Least-Squares approach requires that only the errors on $A(\phi_i)$ are used, and it has been necessary to assume that the ϕ_i values are known without error [106].

5.1.1 Goodness of fit

A convenient feature of using the Least-Squares approach is that there is an easy method of quantifying the 'goodness' of the fit result. Inserting the values for the parameters into weighted sum of squares formula gives:

$$\chi^2 = S_{min} = \sum_i^M \left(\frac{f(s_n^{min})_i - A(\phi_i)}{\sigma_i} \right)^2. \tag{5.9}$$

This quantity can be used to test how good the fit results are. It is most instructive to divide χ^2 by the number of degrees of freedom:

$$ndf = -n + \sum_i^M 1 = M - n. \tag{5.10}$$

Values of χ^2/ndf close to unity suggest that the fit has been successful. Values much smaller than unity indicate that the errors are too large. Large values indicate that the hypothesis is incorrect [106].

5.2 Raw Asymmetries

The Least-Squares method was used to perform fits to beam, target and double asymmetries using the full samples of photon-production and pion-production data. Figure 5.1 shows the results. These asymmetries are raw in the sense that the magnitudes of beam and target polarisation were not taken into account, and the photon-production asymmetries were not corrected for pion contamination. These corrections are discussed below. Each of the asymmetries were formed using 12 equally spaced ϕ-bins. Respectively the

beam, target, and double spin asymmetries were constructed as follows:

$$\begin{aligned} A_{LU}(\phi_i) &= \frac{N_i^{\rightarrow} - N_i^{\leftarrow}}{N_i^{\rightarrow} + N_i^{\leftarrow}}, \\ A_{UL}(\phi_i) &= \frac{N_i^{\Rightarrow} - N_i^{\Leftarrow}}{N_i^{\Rightarrow} + N_i^{\Leftarrow}}, \\ A_{LL}(\phi_i) &= \frac{N_i^{\rightarrow\Rightarrow} + N_i^{\leftarrow\Leftarrow} - N_i^{\leftarrow\Rightarrow} - N_i^{\Leftarrow\rightarrow}}{N_i^{\rightarrow\Rightarrow} + N_i^{\leftarrow\Leftarrow} + N_i^{\leftarrow\Rightarrow} + N_i^{\Leftarrow\rightarrow}}; \end{aligned} \tag{5.11}$$

where the right (left) arrows refer to a positive (negative) polarisation state, and the single (double) arrows refer to beam (target) polarisation. The numbers of counts in each polarisation state were weighted by the beam luminosity for that state, integrated over the full beam time. For example in the double spin asymmetry the numbers of counts in positive-beam negative-target state bins were given by: $N_i^{\rightarrow\Leftarrow} \rightarrow N_i^{\rightarrow\Leftarrow}/L^{\rightarrow\Leftarrow}$; and similarly for the other polarisation states. This ensured that the numbers of counts in each state were relatively proportional to the differential cross section. The average kinematic values for $-t$, x_B and Q^2 correspond to the values given in Table 4.5.

The fit functions used were:

$$\begin{aligned} A^{LU} &= A_1^{LU} sin(\phi) + A_2^{LU} sin(2\phi), \\ A^{UL} &= A_1^{UL} sin(\phi) + A_2^{UL} sin(2\phi), \\ A^{LL} &= A_0^{LL} cos(0\phi) + A_1^{LL} cos(\phi) + A_2^{LL} cos(2\phi). \end{aligned} \tag{5.12}$$

All four single spin asymmetries are dominated by their $\sin(\phi)$ terms. For photon-production data, a dominant $\sin(\phi)$ term is expected for single spin asymmetries when the handbag approximation for DVCS is valid. Non-zero higher order parameters may be the result of contributions from: higher-twist CFF terms, cosine terms in the asymmetry denominator, or the Bethe-Heitler propagators. No attempt is made here to distinguish their relative contributions. The double spin asymmetries have significant $\cos(0\phi)$ (constant) terms. In the photon production case this is expected mainly because of the contribution from the Bethe-Heitler process, which as discussed previously, is not cancelled in the asymmetry numerator. The theoretical background behind harmonic contributions for pion-production data is not discussed here.

The χ^2/ndf values for the fits are all between 0.5 and 2. The primary motivation for performing fits to pion data was to correct the asymmetry parameters for the photon production case. The fit functions were therefore kept the same for each type of asymmetry throughout.

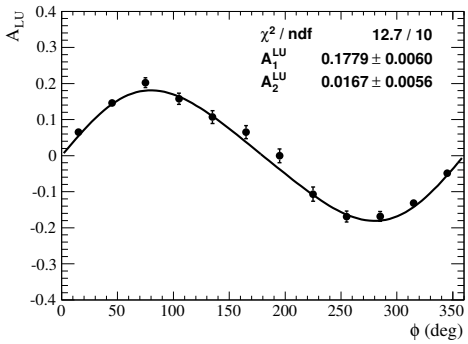

(a) Beam spin asymmetry

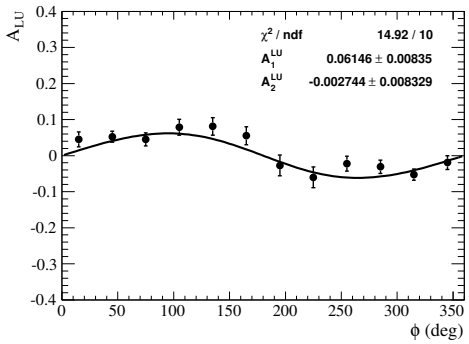

(b) Beam spin asymmetry

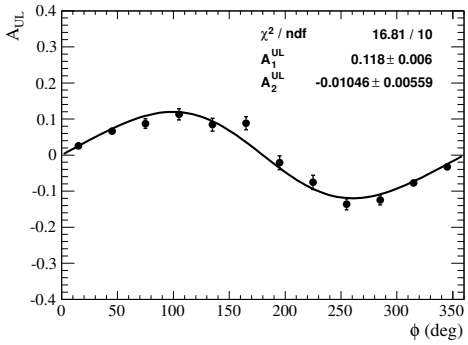

(c) Target spin asymmetry

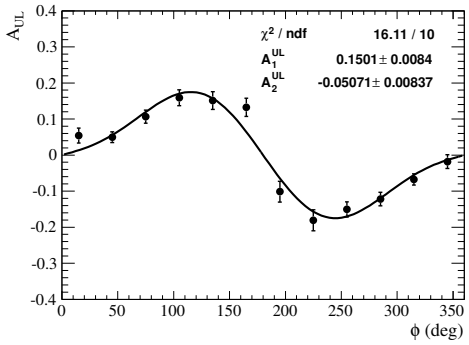

(d) Target spin asymmetry

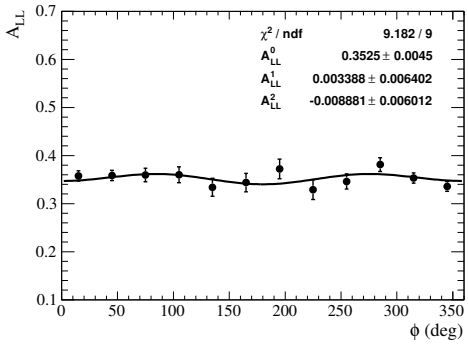

(e) Double spin asymmetry

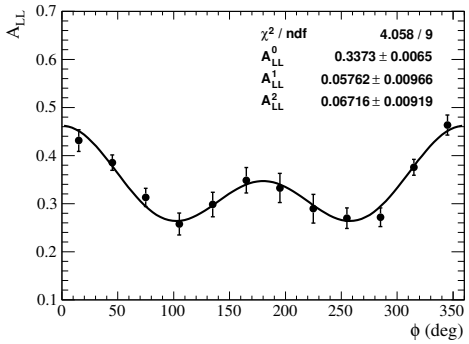

(f) Double spin asymmetry

Figure 5.1: Raw asymmetries using all data after the event selection cuts were applied. Left-hand-side (right-hand-side) plots are for photon (pion) production.

5.3 Beam Polarisation

It was mentioned in Chapter 3 that beam polarisation was measured in dedicated runs using a Møller polarimeter. These measured values were assigned to every event in the standard data taking runs that were recorded after the Møller measurement was carried out. A single overall value for beam polarisation was used for the asymmetry analysis, which was the average of the magnitude of all events for both positive and negative states for the full photon production data set. This value was:

$$P_B \equiv < |P_B| > = 0.85. \tag{5.13}$$

The beam polarisation sign was recorded on an event-by-event basis and was used to assign the correct state to each event for the purposes of constructing asymmetries. The error on the beam polarisation was consistently less than 2% [31] and was neglected in the asymmetry calculations.

5.4 Target Polarisation

The target polarisation was monitored using NMR during experimental operations. This method is known to give an inaccurate measure since the values recorded are biased towards the degree of polarisation at the edges of the target material, and therefore do not properly account for the centre of the target where heating caused by the beam can cause depolarisation to occur. NMR measurements for the target polarisation were therefore not used in the asymmetry analysis. The value of the target polarisation that was used, was taken from a study in which the beam polarisation multiplied by the target polarisation ($P_B P_T$) was extracted using a study of elastic electron-proton scattering [99]. The magnitude of the target polarisation was determined by dividing out the value of the average beam polarisation. The value used in this work was the average of the values for positive and negative states for parts A and B:

$$P_T \equiv < |P_T| > = 0.76 \tag{5.14}$$

The error on this value was around 3 % and was neglected in the asymmetry calculations. The target polarisation sign was flipped after groups of runs were recorded: Figure 4.1 gives an indication of how frequently the target polarisation sign was flipped as a function of run number. Each event in these groups were assigned the corresponding sign for the purposes of constructing asymmetries.

5.5 Dilution Factor

For some of the events remaining in the final samples, the reaction occurred on nucleons in the target which were not polarised. This was not taken into account in the method used to determine the target polarisation. The magnitude of dilution was quantified using a dilution factor, d_f. The value for the dilution factor used in the asymmetry analysis was the average of the results given in the same internal analysis note as mentioned above. This value was:

$$d_f = 0.91. \tag{5.15}$$

The dilution factor was calculated separately for exclusive electroproduction of photon and pion events but these values were very similar so only one value was used in the asymmetry analysis. Taking the differences into account the error on d_f was approximately 3 % and was neglected in the asymmetry calculations.

5.6 Maximum Likelihood Fitting

The principle of maximum likelihood (ML) provides a more general method of parameter estimation than Least-Squares fitting. The best estimates of parameters are found by maximising the likelihood function [107]:

$$L(\phi_i; s_n) = \prod_{i=1}^{N} p(\phi_i, s_n), \tag{5.16}$$

where $p(\phi_i, s_n)$ is a probability density function (pdf). The likelihood function represents the joint probability for all N measurements. In the case where it is appropriate to use a normally-distributed pdf, maximising $L(\phi_i; s_n)$ is equivalent to minimising the sum of squares [108]. This will now be demonstrated using again the simple example of fitting an asymmetry with a single Fourier harmonic. Inserting the normally distributed pdf,

$$p(\phi_i, s_n) = \frac{1}{\sigma_i \sqrt{2}\pi} e^{-(A(\phi_i) - s_1 \sin(\phi_i))^2/(2\sigma_i^2)}, \tag{5.17}$$

into the likelihood function and taking the natural logarithm yields:

$$\ln L = -\sum_{i}^{M} \left(\ln(\sigma_i \sqrt{2}\pi) + (A(\phi_i) - s_1 \sin(\phi_i))^2/(2\sigma_i^2) \right). \tag{5.18}$$

Minimising the negative of this quantity is equivalent to maximising L and is done by taking its derivative with respect to the parameter and setting it equal to zero:

$$\frac{d(-\ln L)}{ds_1} = \sum_i^M \left(\frac{s_1 \sin^2(\phi_i) - A(\phi_i)\sin(\phi_i)}{\sigma_i^2} \right) = 0. \tag{5.19}$$

This is the same as the result that was obtained using the Least-Squares approach. The same equivalence applies in general to any fit function.

Both the Least-Squares method and this example using ML required that the data were binned in order to form the asymmetries. Using these methods means that information on the precise value of ϕ for each event is lost, thus introducing a systematic error. By implementing an un-binned fitting procedure using the likelihood formalism, this loss of information is overcome. The method adopted in this work was a variation of the standard Maximum Likelihood method called Extended Maximum Likelihood (EML).

5.6.1 Extended Maximum Likelihood

In both the previous examples a normal distribution was used as the pdf, which has the property of being normalised to unity. In the case whereby an arbitrary pdf, $f(\phi_i, s_n)$, is chosen, it can be normalised to unity by dividing by its integral:

$$p(\phi_i, s_n) = f(\phi_i, s_n) / \int_{\phi_1}^{\phi_2} f(\phi_i, s_n) \equiv f(\phi_i, s_n)/F; \tag{5.20}$$

where the integral limits correspond to the limits of the range over which it applies: $[\phi_1, \phi_2]$. By normalising, the area of the distribution has been removed.

In some cases, such as in this work, the area of the distribution may be important. In experiments that run for a fixed period of time rather than until a fixed number of events are recorded, the total expected number of counts may provide a better estimate of the true value than the total observed number of counts [109]. As will be shown below, the area under the pdf used in this work corresponds to the expected number of counts.

In the EML method a Poisson distribution is included in the likelihood function,

$$L(\phi_i; s_n) = \frac{F(s_n)^N e^{-F(s_n)}}{N!} \prod_i^N \frac{f(\phi_i, s_n)}{F(s_n)}, \tag{5.21}$$

to account for the probability of observing the total number of counts, N; given the expected number of counts, $F(s_n)$. In this case, the negative of the logarithm of the likeli-

hood is

$$-\ln L(\phi_i;s_n) = -N\ln F(s_n) + F(s_n) + \ln N! - \sum_i^N \ln f(\phi_i,s_n) + \sum_i^N \ln F(s_n). \tag{5.22}$$

On the right-hand-side of this equation the first and last terms cancel and the middle term is not dependent upon the parameters which means it will vanish when the parameters are minimised and can therefore be neglected. The function that is minimised to determine the best estimates of the parameters is:

$$-\ln L(\phi_i;s_n) = F(s_n) - \sum_i^N \ln f(\phi_i,s_n); \tag{5.23}$$

where $f(\phi_i,s_n)$ is called the extended (or un-normalised) pdf and $F(s_n)$ is referred to as the normalisation.

5.7 EML and Spin Asymmetries

EML has already been shown to be an effective method of fitting polarised asymmetries by the HERMES collaboration. They found it to out-perform the standard ML [110] and Least-Squares [111] methods. This section explains the procedures used in this work which are consistent with those used in [87].

For an experiment in which the beam and target are both longitudinally polarised, the reaction rate is:

$$f(\phi_i,s_n) = \mathcal{L}(t)\eta\,\sigma_{UU}(\phi)[1 + P_B A_{LU} + P_B P_T A_{LL} + P_T A_{UL}] \tag{5.24}$$

where $\mathcal{L}(t)$ is the luminosity per unit time, P_B (P_T) is the beam (target) polarisation, η is the detector efficiency, and σ_{UU} is the unpolarised cross section for exclusive events. Integrated over the duration of the experiment and all phase-space, this quantity gives the expected number of counts. Taking the detector efficiency to be unity, the expected number of counts is:

$$\begin{aligned} F(\phi_i,s_n) &= \int [F^{\rightarrow\Leftarrow}(\phi;s_n) + F^{\rightarrow\Rightarrow}(\phi;s_n) + F^{\leftarrow\Leftarrow}(\phi;s_n) + F^{\leftarrow\Rightarrow}(\phi;s_n)]\,dx \\ &\approx \sum_i^N \frac{1}{4L^{\leftrightarrow\Leftrightarrow}} \left[m_{UU} + m_{LU}A_{LU} + m_{LL}A_{LL} + m_{UL}A_{UL}\right], \end{aligned} \tag{5.25}$$

where $L^{\leftrightarrow\Leftrightarrow}$ is either: $L^{\rightarrow\Rightarrow}$, $L^{\leftarrow\Rightarrow}$, $L^{\rightarrow\Leftarrow}$, or $L^{\leftarrow\Leftarrow}$ depending on the polarisation state

relevant to the event; and the other factors are:

$$\begin{aligned} m_{UU} &= L^{\rightarrow\Rightarrow} + L^{\rightarrow\Leftarrow} + L^{\leftarrow\Rightarrow} + L^{\leftarrow\Leftarrow} \\ m_{UL} &= (L^{\rightarrow\Rightarrow} - L^{\rightarrow\Leftarrow} + L^{\leftarrow\Rightarrow} - L^{\leftarrow\Leftarrow})P_T \\ m_{LU} &= (L^{\rightarrow\Rightarrow} + L^{\rightarrow\Leftarrow} - L^{\leftarrow\Rightarrow} - L^{\leftarrow\Leftarrow})P_B \\ m_{LL} &= (L^{\rightarrow\Rightarrow} - L^{\rightarrow\Leftarrow} - L^{\leftarrow\Rightarrow} + L^{\leftarrow\Leftarrow})P_B P_T. \end{aligned} \tag{5.26}$$

The resulting likelihood function to be minimised is:

$$-\ln L = -\sum_{i=0}^{N} \ln[1 + P_B A_{LU} + P_T A_{UL} + P_B P_T A_{LL}] + F(\phi_i, s_n); \tag{5.27}$$

where $F(\phi_i, s_n)$ from Equation 5.25, and the asymmetries from Equation 5.12 were used; without the $\cos(2\phi)$ terms.

The target and double spin asymmetries were corrected for the dilution factor by dividing the amplitudes and errors of the fit parameters by the value of d_f quoted previously.

5.8 EML and Least-Squares Comparison

Fits to the photon and pion production data were carried out using both the EML and Least-Squares methods. This time the Least-Squares asymmetries were corrected for the dilution factor and beam and target polarisations, which was done by scaling Equations 5.11 as follows:

$$\begin{aligned} A_{LU} &\rightarrow \frac{A_{LU}}{P_B} \\ A_{UL} &\rightarrow \frac{A_{UL}}{P_T d_f} \\ A_{LL} &\rightarrow \frac{A_{LL}}{P_B P_T d_f}. \end{aligned} \tag{5.28}$$

Further to this, the data were split into five kinematic bins. Five bins for $-t$ and x_B were used separately. The binning schemes adopted are given in Table 5.1. Tables 5.2 and 5.3 give the average values for the kinematic variables $-t$, x_B and Q^2 in these bins for photon and pion production data respectively. Figures 5.2 and 5.3 show the results for the primary fit parameters for photon and pion production data in five $-t$ bins and five x_B bins respectively. Figures 5.4 and 5.5 show the same for the secondary fit parameters.

These results show a good level of consistency between both fitting methods for all three types of asymmetries in both binning schemes and for both the photon-production and pion-production data sets. This indicates that the results obtained are almost indepen-

dent of the fitting method used. Small differences in the results between the two fitting methods that are observed could be assigned as a source of systematic uncertainty, however the difference is in general far smaller than the random uncertainties and does not appear to result in the best estimates of the parameters taking consistently larger or smaller values for one method rather than the other. At close inspection some of the parameters determined using the EML method have smaller errors than for the Least-Squares method. This is perhaps most evident for the double spin asymmetry primary coefficient results binned in $-t$: see the bottom left plot of Figure 5.2 for example. The reason for this is likely due to the EML method being performed on and event-by-event basis, which utilises the exact values for ϕ.

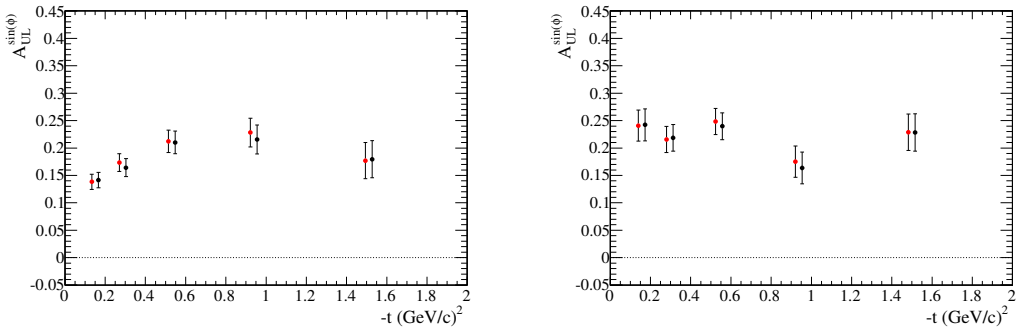

(a) TSA $\sin(\phi)$

(b) TSA $\sin(\phi)$

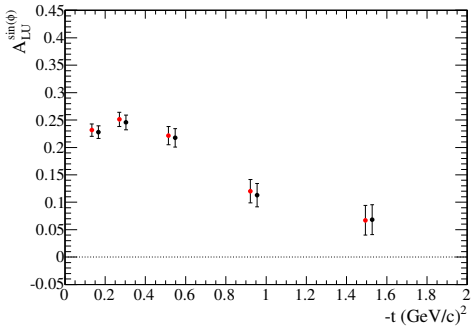

(c) BSA $\sin(\phi)$

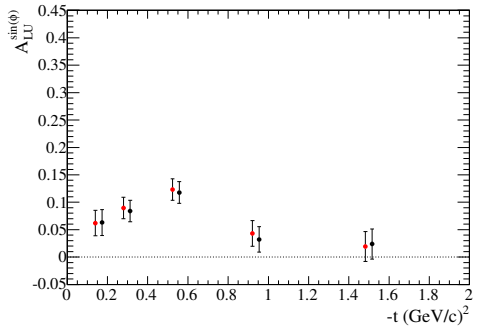

(d) BSA $\sin(\phi)$

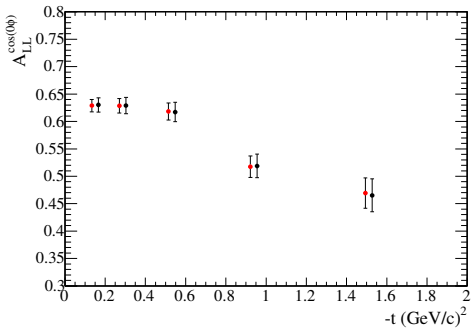

(e) DSA $\cos(0\phi)$

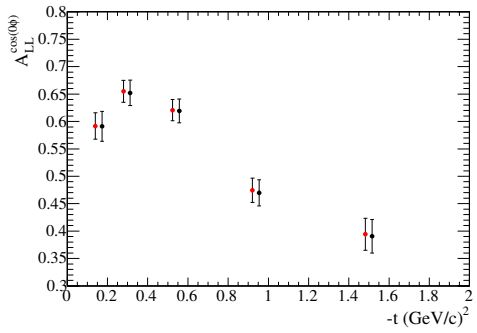

(f) DSA $\cos(0\phi)$

Figure 5.2: $-t$ progression of the primary DVCS (LHS) and DVMP (RHS) spin asymmetry coefficients. Data points are plotted at the average values of the kinematic variable being binned. The results for the Least-Squares (EML) fits are shown in black (red) and have been offset in the x coordinate by $+0.017$ (-0.017) to avoid them being obscured.

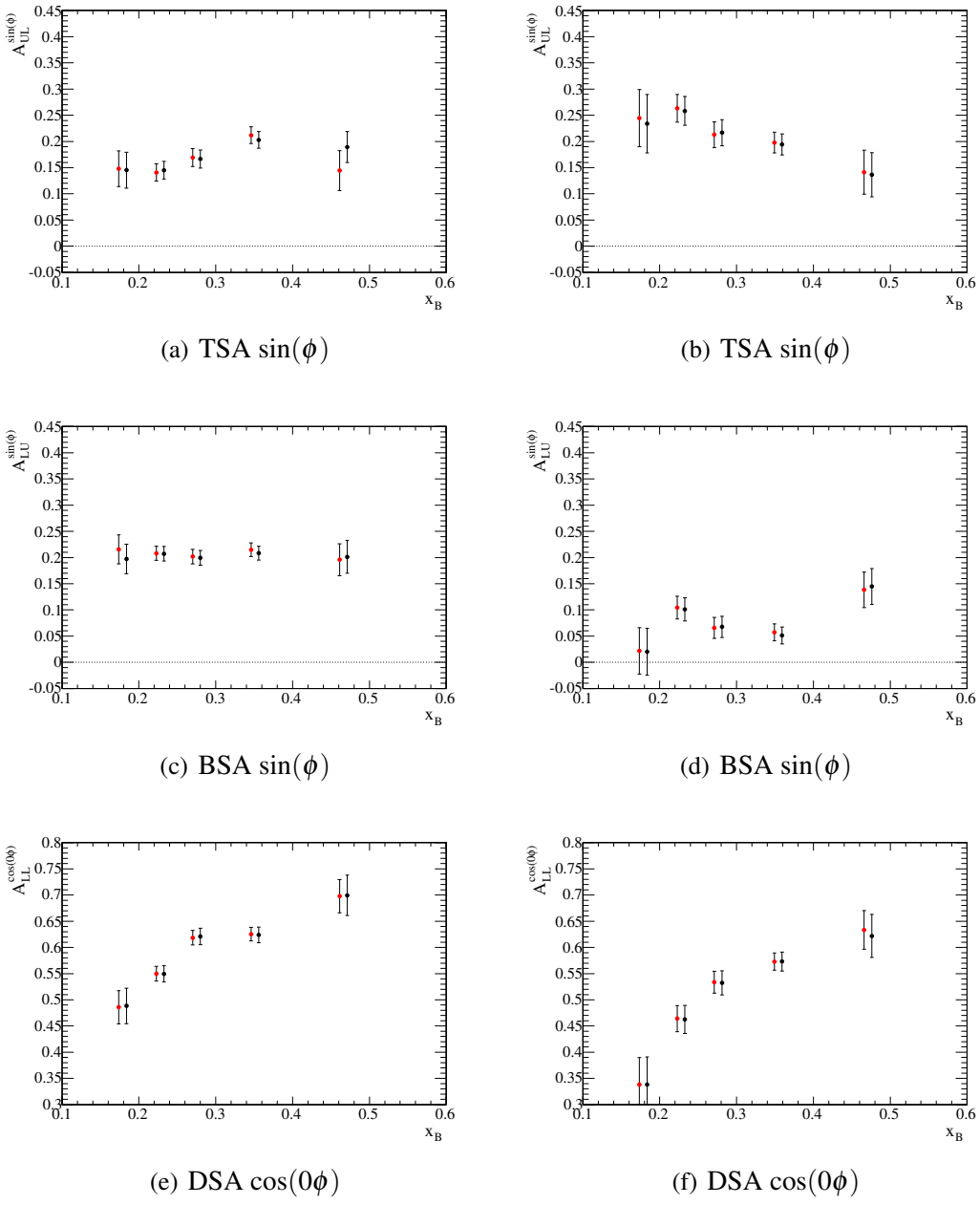

(a) TSA $\sin(\phi)$ (b) TSA $\sin(\phi)$

(c) BSA $\sin(\phi)$ (d) BSA $\sin(\phi)$

(e) DSA $\cos(0\phi)$ (f) DSA $\cos(0\phi)$

Figure 5.3: x_B progression of the primary DVCS (LHS) and DVMP (RHS) spin asymmetry coefficients. Data points are plotted at the average values of the kinematic variable being binned. The results for the Least-Squares (EML) fits are shown in black (red) and have been offset in the x coordinate by $+0.005$ (-0.005) to avoid them being obscured.

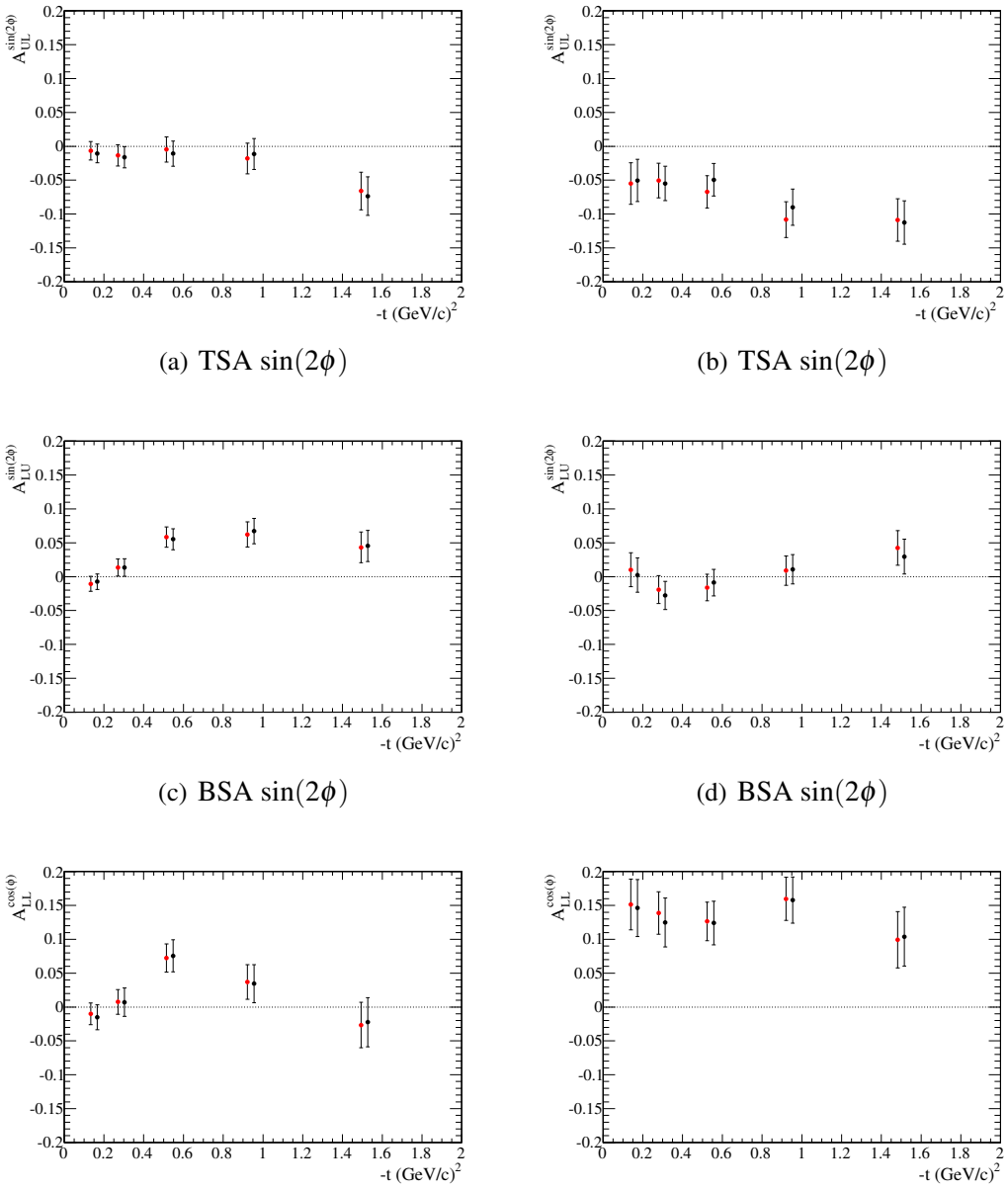

(a) TSA $\sin(2\phi)$ (b) TSA $\sin(2\phi)$

(c) BSA $\sin(2\phi)$ (d) BSA $\sin(2\phi)$

(e) DSA $\cos(\phi)$ (f) DSA $\cos(\phi)$

Figure 5.4: $-t$ progression of the secondary DVCS (LHS) and DVMP (RHS) spin asymmetry coefficients. Data points are plotted at the average values of the kinematic variable being binned. The results for the Least-Squares (EML) fits are shown in black (red) and have been offset in the x coordinate by $+0.017$ (-0.017) to avoid them being obscured.

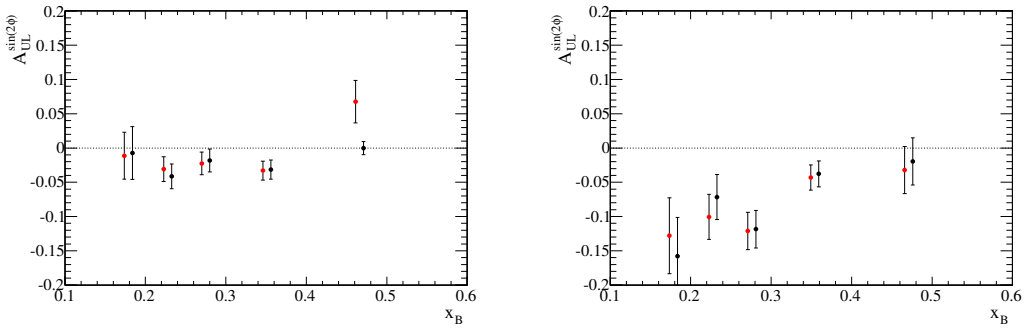

(a) TSA $\sin(2\phi)$

(b) TSA $\sin(2\phi)$

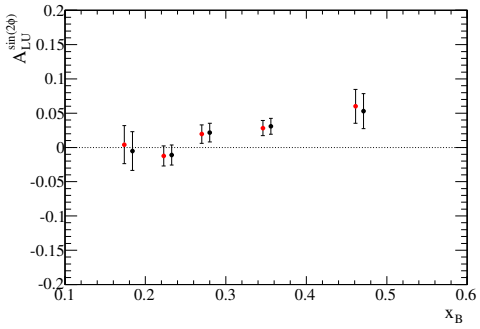

(c) BSA $\sin(2\phi)$

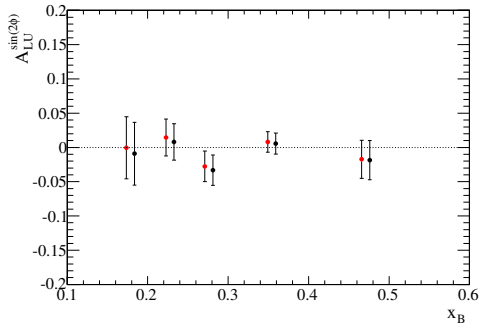

(d) BSA $\sin(2\phi)$

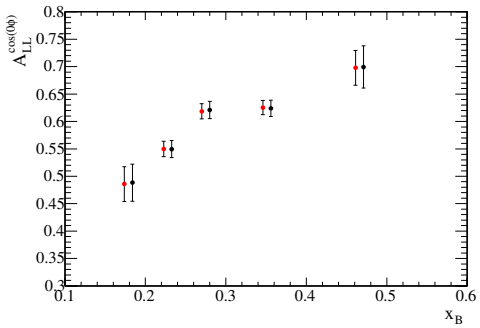

(e) DSA $\cos(\phi)$

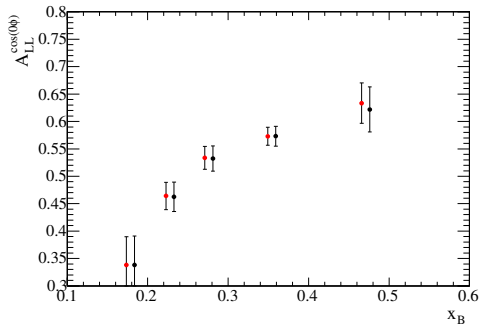

(f) DSA $\cos(\phi)$

Figure 5.5: x_B progression of the secondary DVCS (LHS) and DVMP (RHS) spin asymmetry coefficients. Data points are plotted at the average values of the kinematic variable being binned. The results for the Least-Squares (EML) fits are shown in black (red) and have been offset in the x coordinate by $+0.005$ (-0.005) to avoid them being obscured.

bin	1	2	3	4	5
$-t$ bin width	[0.00,0.21)	[0.20,0.39)	[0.39,0.72)	[0.72,1.20)	[1.20,2.00)
yield (γ)	22988	18212	13894	9714	7690
yield (π^0)	4411	6538	7770	6664	4455
x_B bin width	[0.10,0.20)	[0.20,0.25)	[0.25,0.30)	[0.30,0.42)	[0.42,0.60)
yield (γ)	4996	13389	18073	28813	7227
yield (π^0)	1725	4512	6232	12634	4735

Table 5.1: Binning schemes for the variables $-t$ and x_B and yields per bin. These systems were used for both the photon-production and pion-production data-sets.

data-set	$-t$ bin	1	2	3	4	5
γ	$<-t>\ (GeV/c)^2$	0.15	0.29	0.53	0.93	1.51
π^0	$<-t>\ (GeV/c)^2$	0.16	0.30	0.54	0.94	1.50
γ	$<x_B>$	0.25	0.31	0.35	0.36	0.35
π^0	$<x_B>$	0.25	0.31	0.35	0.36	0.36
γ	$<Q^2>\ (GeV/c)^2$	2.06	2.47	2.70	2.63	2.50
π^0	$<Q^2>\ (GeV/c)^2$	1.95	2.36	2.60	2.60	2.59

Table 5.2: Average kinematics in $-t$ bins for photon and pion production data-sets.

	x_B bin	1	2	3	4	5
γ	$<-t>\ (GeV/c)^2$	0.33	0.32	0.40	0.63	1.03
π^0	$<-t>\ (GeV/c)^2$	0.45	0.50	0.57	0.73	1.07
γ	$<x_B>$	0.18	0.23	0.27	0.35	0.46
π^0	$<x_B>$	0.18	0.23	0.28	0.35	0.47
γ	$<Q^2>\ (GeV/c)^2$	1.52	1.90	2.22	2.66	3.45
π^0	$<Q^2>\ (GeV/c)^2$	1.52	1.84	2.12	2.55	3.46

Table 5.3: Average kinematics in x_B bins for photon and pion production events.

5.9 Neutral Pion Contamination

The contribution from neutral pion contamination to the DVCS spin asymmetry coefficients was calculated using a combination of the exclusive pion production asymmetry coefficients and the Monte Carlo simulated data for neutral pion production.

The ratio of acceptances for the CLAS detector for neutral pion production in which one and two photons were detected was estimated using the relative number of neutral pion generated MC events passing all the DVCS $\left(N_{MC}^{ep\pi^0(\gamma)}\right)$ and neutral pion cuts $\left(N_{MC}^{ep\pi^0(\gamma\gamma)}\right)$. This acceptance ratio was calculated as:

$$A_R = \frac{N_{MC}^{ep\pi^0(\gamma)}}{N_{MC}^{ep\pi^0(\gamma\gamma)}}. \tag{5.29}$$

The acceptance ratio was used to determine the number of events in the DVCS data sample corresponding to pion production as follows:

$$N^{ep\pi^0(\gamma)} = A_R N^{ep\pi^0(\gamma\gamma)}; \tag{5.30}$$

where $N^{ep\pi^0(\gamma\gamma)}$ is the number of events in the neutral pion data sample. The fraction of events in the DVCS sample coming from neutral pion contamination was then calculated to be:

$$f^{\pi^0} = \frac{N^{ep\pi^0(\gamma)}}{N^{ep\gamma}}. \tag{5.31}$$

The measured DVCS asymmetries came from a combination of DVCS and neutral pion production:

$$A_{measured}^{DVCS} = (1 - f^{\pi^0})A_{true}^{DVCS} + f^{\pi^0}A^{ep\pi^0}. \tag{5.32}$$

The true values for the asymmetries were determined by rearranging the equation above:

$$A_{true}^{DVCS} = \frac{A_{measured}^{DVCS} - f^{\pi^0}A^{ep\pi^0}}{1 - f^{\pi^0}}. \tag{5.33}$$

The standard error on this quantity is:

$$\sigma_{true} = \frac{\left(\sigma_{measured}^2 + (f^{\pi^0}\sigma_{\pi^0})^2\right)^{\frac{1}{2}}}{1 - f^{\pi^0}}. \tag{5.34}$$

Contamination fractions were calculated for all the bins given in Table 5.1. The resulting values are given in Table 5.4. These values were used along with the last two equations to correct the EML fit parameters. The contamination-corrected asymmetry fit parameter

results are presented in Chapter 6.

bin	1	2	3	4	5
$-t$	0.076	0.168	0.302	0.413	0.369
x_B	0.168	0.161	0.173	0.246	0.375

Table 5.4: Pion-contamination fractions for $-t$ and x_B bins.

5.10 Systematic Uncertainties

The quantities that are expected to contribute a source systematic error on the final asymmetry results are listed in Table 5.5. These results are quoted from an internal CLAS analysis note [99] to which this author contributed. It should be noted that since the analysis methods used in this work were carried out independently[1], these results only serve as an approximation of the systematic uncertainties. The calculations for these quantities were performed as follows:

- Exclusivity cuts. The exclusivity cuts were varied to observe what effect they had on the resulting ϕ-binned DVCS target spin asymmetries. Three different cut widths were used: 2.5-σ, 3-σ and 3.5-σ. The deviation of the asymmetry data points from the value found when 3-σ cuts were used, were averaged to arrive at the quoted result. It should be noted that for the analysis used in this part of the systematic study, 3-σ values were used as standard for exclusive variable cut widths, which as explained in Chapter 4 was not the case for this work.

- $P_B P_T$. The target spin asymmetry was re-calculated using two additional values for P_T. These values were the extreme values for P_T found when the maximum and minimum for $P_B P_T$ was used, as calculated by including the minimum and maximum random errors: $(P_B P_T)^{max} = P_B P_T + \sigma_{P_B P_T}, (P_B P_T)^{min} = P_B P_T - \sigma_{P_B P_T}$. The result quoted was the average deviation of the asymmetries for the two extreme cases.

- Dilution factor. The target spin asymmetry was re-calculated using two additional values for d_f. In the same manner as the systematic error for P_T was determined, minimum and maximum values for d_f were calculated using the maximum and

[1]The author is grateful for collaborative discussions with the analysis note co-authors and EG1DVCS run group in regards to event selection procedures. These discussions led to a largely consistent particle identification procedure for independent DVCS and pion analyses and some consistency in the reaction identification and background subtraction procedures.

minimum random errors: $d_f^{max} = d_f + \sigma_{d_f}, d_f^{min} = d_f - \sigma_{d_f}$. The result quoted was the average deviation of the asymmetries for the two extreme cases.

- π^0 background subtraction. All three types of spin asymmetries were re-calculated using varied acceptance ratio values (A_R). The values used were: $A_R^{max} = 1.3 \cdot A_R$, $A_R^{min} = 0.7 \cdot A_R$. The results quoted were the average deviations of each of the asymmetries for the two extreme cases.

- Analysis technique. The exclusivity cut widths for analyses carried out by two of the analysis note co-authors [99] (E. Seder and S. Pisano) were developed using slightly different fitting techniques: the exclusive variable fit ranges, fit functions and binning were not common to both analyses. This resulted in different sets of exclusivity cut widths. Furthermore the analysis codes were written independently. Whilst some contribution from these differences was already taken into account by altering the exclusivity cut widths, it was considered that these differing techniques may indicate an additional systematic uncertainty. The value quoted corresponds to half the relative difference in the results obtained for the target spin asymmetries for these two analyses. In the future an additional check could be performed using the exclusivity cuts procedure developed in this work.

- Radiative corrections. The theoretical formalism that was used to extract the asymmetry results was based on the leading order processes for DVCS and BH. The radiative emission of a photon has a probability to occur during these processes and was not taken into account in the analysis method. However, calculations have shown that the contribution in the CLAS kinematic range is expected to be small [112]. This discrepancy is therefore included as a source of systematic error.

Source	Systematic uncertainty
Exclusivity cuts	2.5%
$P_B P_t$	2.6%
Dilution factor	1.4%
π^0 Background subtraction	0.75% (TSA), 4.0% (BSA), 0.9% (DSA)
Analysis technique	1.9%
Radiative corrections	0.1%
Total (sum in quadrature)	4.4% (TSA), 5.9% (BSA), 4.4% (DSA)

Table 5.5: Summary table of all the kinds of systematic uncertainties studied. Table adapted from [99].

5.11 Summary

In this chapter, two methods of parameter estimation were compared: Least-Squares fitting and the Extended Maximum Likelihood method. These methods were both shown to provide a suitable framework for fitting sinusoidal functions to beam, target and double spin asymmetries for photon and pion production reactions. In the next and final chapter, results will be shown for pion contamination corrected DVCS asymmetries using the EML results.

Chapter 6

Results, Conclusions and Outlook

In this chapter final results are presented and compared to model predictions. The document concludes by summarising this work and briefly discussing the future for nucleon structure physics experiments in Hall B at Jefferson Lab.

6.1 Final Results

The DVCS target, beam and double spin asymmetry fit parameters were corrected for neutral pion contamination using the procedures discussed in Chapter 5. The parameters obtained using the EML fitting method were used and have been plotted alongside VGG model predictions. These predictions were calculated for this work specifically using the VGG code [113]. The inputs to the code are explained in Appendix A.

6.1.1 Target Spin Asymmetry

Figures 6.1 and 6.2 show target spin asymmetry fit parameters as a function of the variables x_B and $-t$ for data (red points), and VGG model predictions in which the contribution from the GPD $\widetilde{H}$ was (blue points) and was not (black points) included.

In Figure 6.1(a) it is clear that the model in general underestimates the magnitudes of the asymmetries when $\widetilde{H}$ is not included. This agrees with the expectation that the target spin asymmetry is a result of significant contributions from both of the GPDs H and $\widetilde{H}$, and highlights the importance of performing experiments with a polarised target: beam spin asymmetry measurements are mostly sensistive to H only. The progression of the data in x_B follows a similar trend to the VGG model points, and for all but one point, the magnitudes of the asymmetries are consistent, within experimental error, to all the VGG points when $\widetilde{H}$ was included. These results appear to show consistency with the previous CLAS target spin asymmetry analysis [76] and significantly increases the total data-set

available. The experimental error bars for these results are approximately half the size of the previous result, the range over x_B covered is larger, and there are five bins instead of three.

It is worth noting that due to the acceptance of the CLAS detector, increasing bins in x_B also tend to have increasingly large values of Q^2. This was taken into account in the model points, which were calculated using the same average kinematic values as the photon-production data. One source of discrepancy is the difference in kinematic averages between the photon- and pion-production data. These differences can be seen in Table 5.3. The pion production data has relatively more events at larger $-t$ and x_B values - as shown in Figure 4.34. The main differences are for $-t$ in the x_B-bins: the pion production data has in general larger average values for $-t$ than the photon-production data. A potential improvement to the results could be made by extrapolating between the pion asymmetry points to the position at which the average kinematics have the best agreement with the photon-production data.

In Figure 6.1(b) the $\sin(2\phi)$ coefficients are small and in three bins they are consistent with zero within experimental error. The model predictions in general overestimate these parameters. This could be due to higher-order twist processes contributing to the data which are not included in the model.

Figure 6.2(a) shows the $-t$ progression of the target spin asymmetry $\sin(\phi)$ coefficient. The agreement between the data and model predictions are not as good as for the x_B progression results. In the two smallest $-t$-bins, the version of model without $\widetilde{H}$ agrees better with the data. The data and model predictions are both seen to peak but at quite different values of $-t$.

It is not clear why the $\sin(2\phi)$ coefficients in Figure 6.2(b) agree better with the model predictions than the those in Figure 6.1(b).

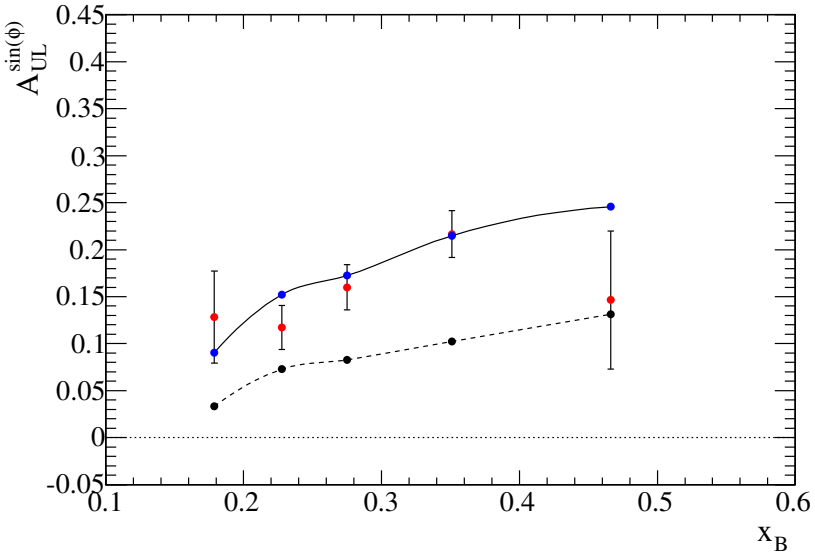

(a) DVCS TSA $sin(\phi)$ coefficients.

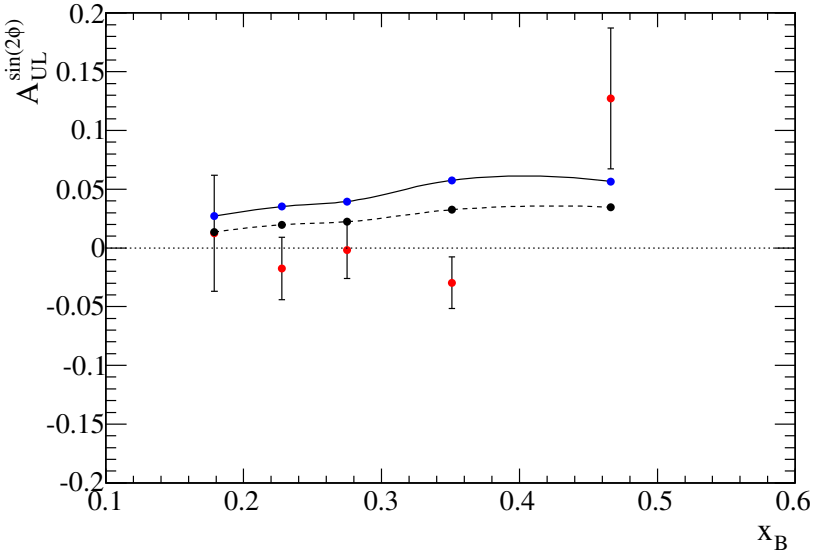

(b) DVCS TSA $sin(2\phi)$ coefficients.

Figure 6.1: x_B progression of proton DVCS target spin asymmetry (TSA) coefficients. The red points are EML fit results with the contribution from neutral pion production subtracted. The blue and black points are the results from χ^2 fits to the output from VGG-code, calculated at the average kinematics of the data points. The contribution from $\widetilde{H}$ was omitted for the black points. Lines that join the model points are there to help guide the eye.

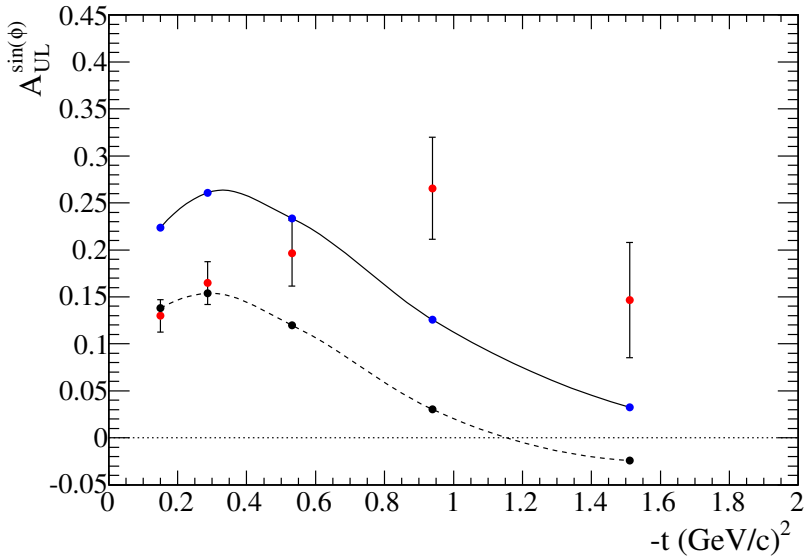

(a) DVCS TSA $sin(\phi)$ coefficients.

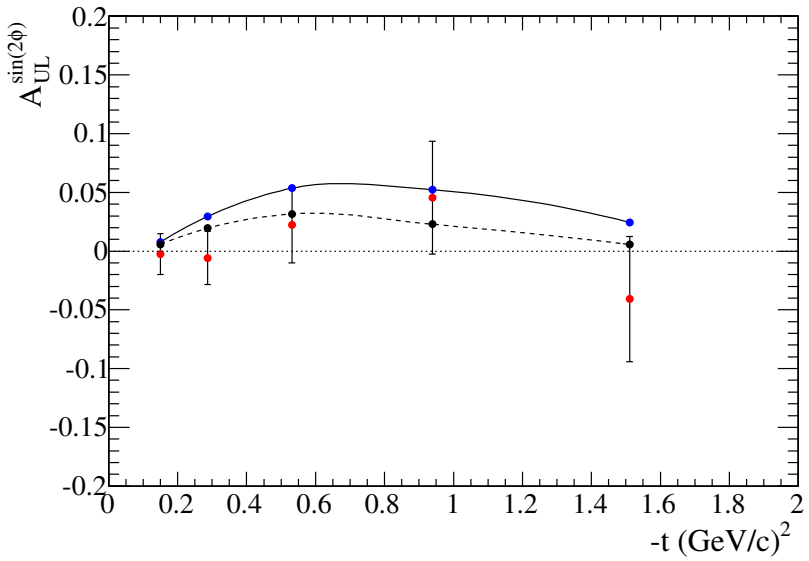

(b) DVCS TSA $sin(2\phi)$ coefficients.

Figure 6.2: $-t$ progression of proton DVCS target spin asymmetry (TSA) coefficients. Data and model points have the same convention as in Figure 6.1.

6.1.2 Beam Spin Asymmetry

Figures 6.3 and 6.4 show beam spin asymmetry (BSA) fit parameters as a function of the variables x_B and $-t$. The similarity between the two model versions highlights that the relative contribution from $\widetilde{H}$ compared to H is expected to be less for the beam spin asymmetry than for the target spin asymmetry.

Figure 6.3(a) shows the x_B progression of the $\sin(\phi)$ coefficient. The asymmetries take quite constant values which are larger than the same coefficient for the target spin asymmetry. The model points tend to overestimate the data.

Similar differences between the data and the model predictions can be seen for the $\sin(2\phi)$ parameters in Figure 6.3(b) as for the same parameters for the target spin asymmetry: the models generally appear to overestimate the data except in the largest x_B bin where the model point lies close to the lower limits of the experimental error.

The $-t$ progression of the beam spin asymmetry $\sin(\phi)$ coefficient is shown in Figure 6.3(a). The agreement with the model is better at large values of $-t$. In the lowest $-t$ bins the model overestimates the results. This observation shows consistency with the main previous CLAS beam spin asymmetry results [72] - as shown in Figure 2.8. In general the magnitudes of the $\sin(2\phi)$ parameters in Figure 6.3(b) agree reasonably well with the model points; as was the case for the same parameters for the target spin asymmetry.

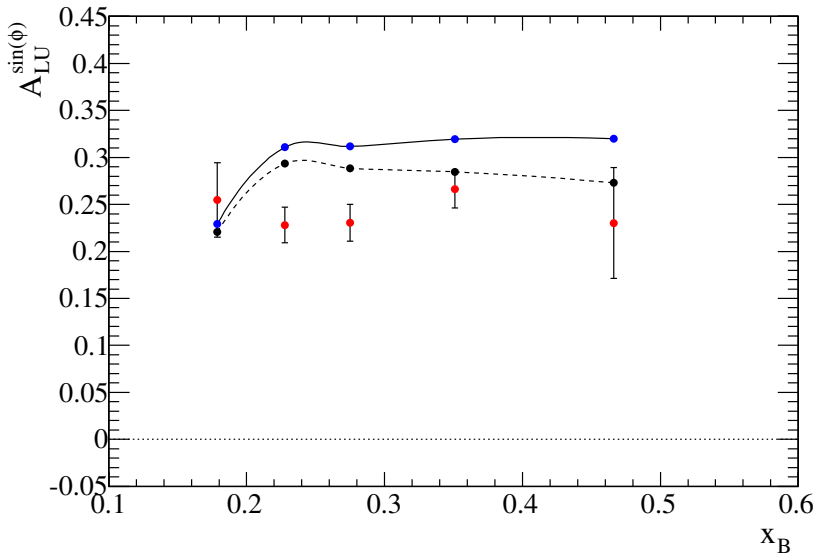

(a) DVCS BSA $sin(\phi)$ coefficients.

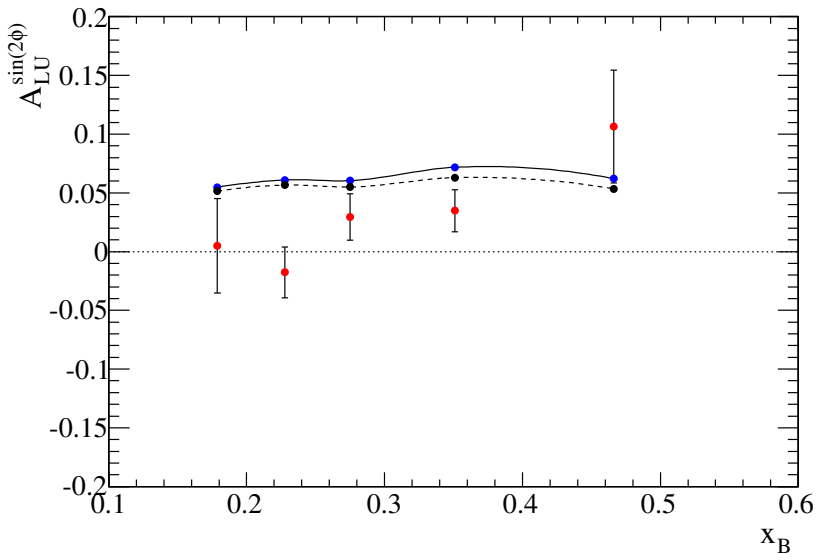

(b) DVCS BSA $sin(2\phi)$ coefficients.

Figure 6.3: x_B progression of proton DVCS beam spin asymmetry (BSA) coefficients. Data points have the same convention as in Figure 6.1.

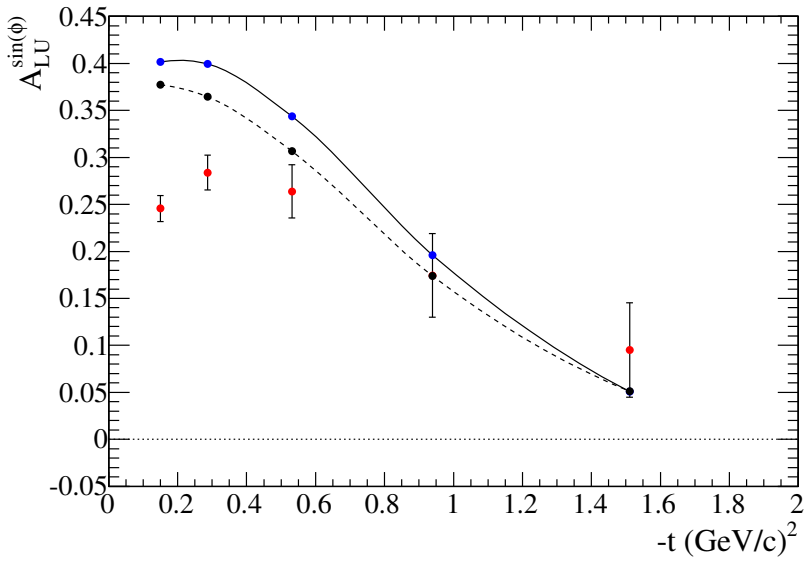

(a) DVCS BSA $sin(\phi)$ coefficients.

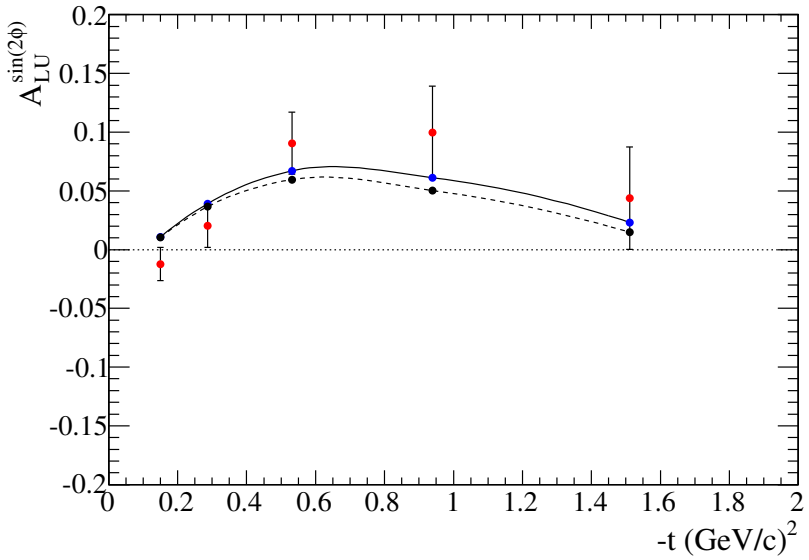

(b) DVCS BSA $sin(2\phi)$ coefficients.

Figure 6.4: t progression of proton DVCS beam spin asymmetry (BSA) coefficients. Data points have the same convention as in Figure 6.1.

6.1.3 Double Spin Asymmetry

Figures 6.5 and 6.6 show the final results for the double spin asymmetry fit parameters. In Figure 6.5(a) there is a poorer agreement between the data and the model predictions than in Figure 6.6(a). It is not clear why all of the model points underestimate the data when it is binned in x_B but not when it is binned in $-t$. This could be because the differences in the average kinematics for the pion data compared to the photon data are more significant for the x_B binning scheme, or because deficiancies in the model are more pronounced for the double spin asymmetry at the average kinematics of the x_B bins. The double spin asymmetry dependends on the amplitudes for the BH process, DVCS and the interference term and therefore has a rather complicated dependence on CFFs and therefore also GPDs. The GPD E was not included in the version of the model used and could for example play a significant role.

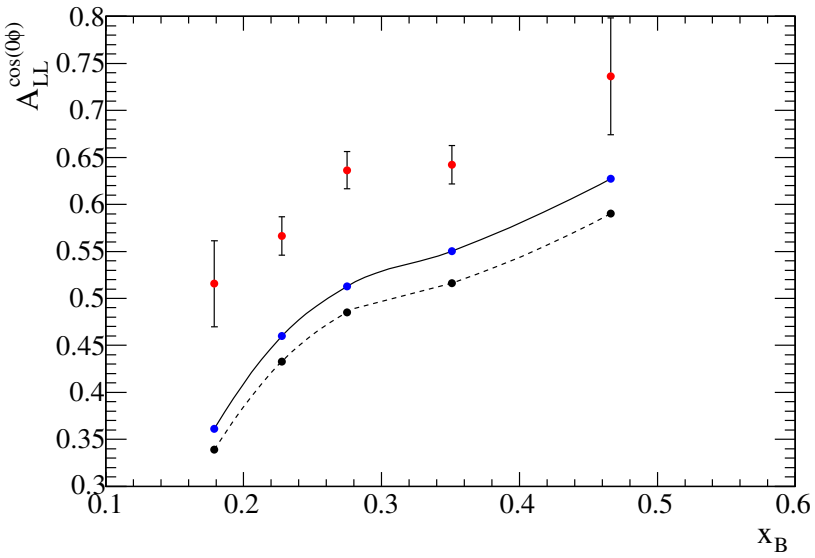

(a) DVCS DSA $cos(0\phi)$ coefficients.

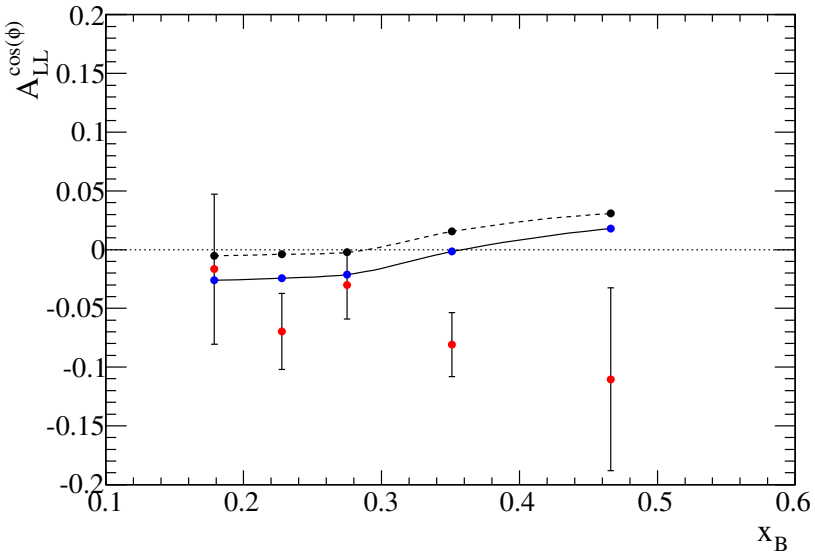

(b) DVCS DSA $cos(\phi)$ coefficients.

Figure 6.5: x_B progression of proton DVCS double spin asymmetry (DSA) coefficients. Data points have the same convention as in Figure 6.1.

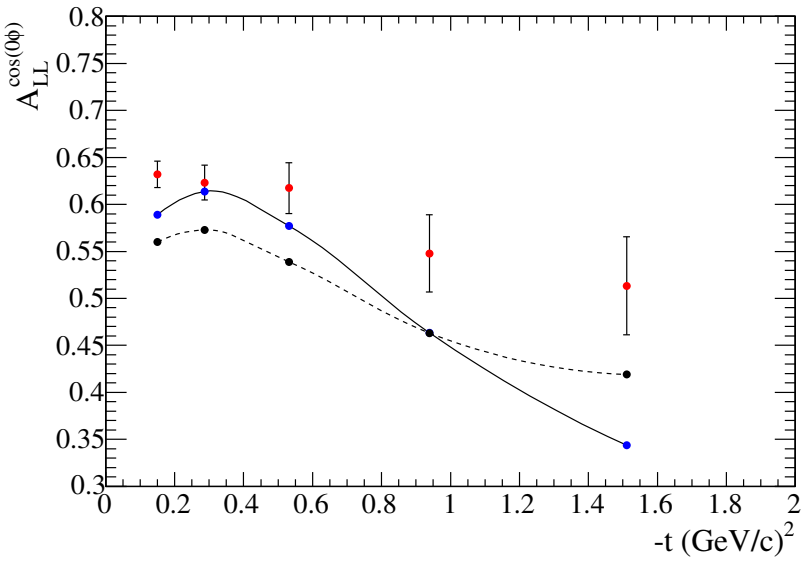

(a) DVCS DSA $cos(0\phi)$ coefficients.

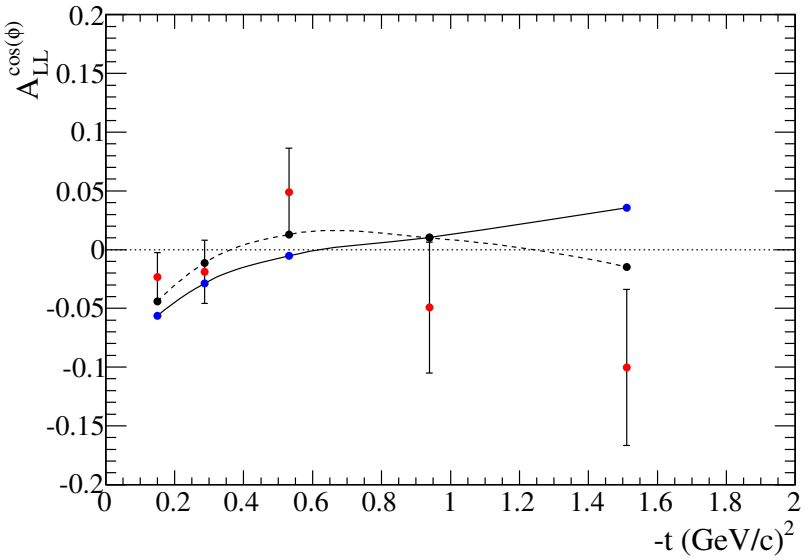

(b) DVCS DSA $cos(\phi)$ coefficients.

Figure 6.6: $-t$ progression of proton DVCS double spin asymmetry (DSA) coefficients. Data points have the same convention as in Figure 6.5.

6.2 Summary, Conclusions and Outlook

This thesis presented measurements of spin asymmetries for deeply virtual Compton scattering off the proton using the Extended Maximum Likelihood method. The primary motivation for undertaking this study was to investigate the dependencies of the target spin asymmetry on the variables x_B and $-t$. These results were shown in this chapter along with results for beam and double spin asymmetries. Varying levels of agreement were found when the results were compared to model predictions using the VGG framework.

The data used were recorded with the CLAS detector system at Jefferson Laboratory in a dedicated polarised target experiment. Starting with a sample of over a billion events containing all kinds of different electron scattering processes, reactions corresponding to the exclusive electroproduction of photons were carefully selected. This was achieved by identifying the reaction final-state particles, and rejecting background processes by imposing conditions based on the reaction kinematics and exclusivity of the process.

The theoretical background for proton structure physics was reviewed in the first two chapters. Generalised parton distributions (GPDs) were introduced via their relation to Wigner distributions, form factors and parton distribution functions. The connection between GPDs and deeply virtual Compton spin asymmetry amplitudes was described. Compton form factors were shown to provide the link between these experimental observables and GPDs.

This analysis offers a new source of input to the deep exclusive processes global data set and thus an important additional constraint to apply to GPD models. It is foreseen that such constraints will lead to a more thorough understanding of the structure of protons, and help to explain how the underlying distributions of quarks and gluons inside it, give rise to the global properties by which it is defined.

The electron accelerator at Jefferson Laboratory is in the process of being upgraded. The maximum beam energy available will be 12 GeV, twice the maximum energy available previously. A new detector system has been designed for Hall B called CLAS12, which will be able to operate at an order of magnitude higher luminosity than CLAS. Figure 6.7 is an illustration of CLAS12, which has a more forward-focussed design than CLAS to reflect the higher beam energy. This will enable a wide experimental program of high precision measurements in a large region of unexplored phase phase, taking future investigations into nucleon structure to an even deeper level.

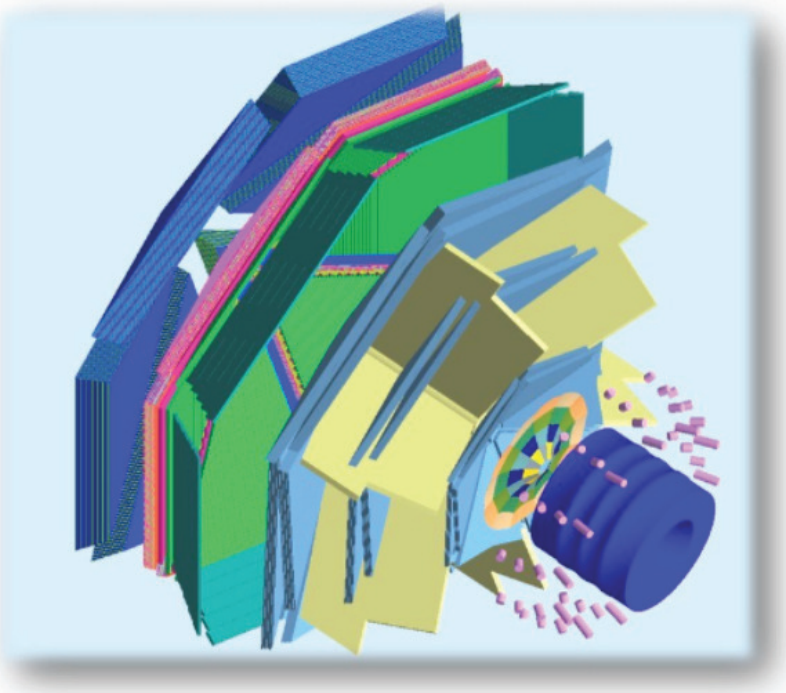

Figure 6.7: Illustration of the CLAS12 detector system.

Appendix A

VGG Code

The VGG code has many input options, which allows the user to pick which version of the model they require and what they want to calculate with it. For this work the code was used to calculate the ϕ-dependance of 2-body doubly-polarised cross-sections for DVCS using a polarised lepton beam and a polarised target. Two different model versions were utilised. They were the same in all respects except that the contribution from $\widetilde{H}$ was excluded in one.

The code was executed once for each x_B and $-t$ bin. The average values of the kinematics of the photon production data for x_B, Q^2 and $-t$ for each bin were used. The output contained values for the differential cross section for each of the four possible polarisation states at 12 ϕ values corresponding to the centre of the ϕ bins used for the data in the Least-Squares fitting method. This data was used to construct target, beam and double spin asymmetries using the same procedures as the data, which were then fitted using the Least-Squares method. The following section lists the inputs to the code used.

A.1 VGG code inputs

- 4 : 2-body DOUBLY POLARISED cross sections for (D)DVCS polarised electron, polarised target
- 3 : Bethe-Heitler + DVCS contribution
- 1 = proton
- 35 : xi dependent parametrisation with MRST02 NNLO distribution at μ^2 = 1 GeV^2
- 1 (Give the value for the power b in the profile function for the valence contribution to H)
- 1 (Give the value for the power b in the profile function for the sea contribution to H)
- 8 = R2 Regge ansatz model (t-dep in DDs)
- 1.08 (Enter slope alphap (GeV-2))
- 2 = No (Do you want to evaluate the D-term contribution to the GPD H?)
- 3 = No, E = 0 (Do you want to evaluate the GPD E?)
- 2 = No (Do you want to evaluate the pi0 pole contribution (i.e. SPD Etilde)?)
- 1: Do not include twist-3 corrections for L photon, but include the minimal corrections to restore gauge invariance for T photon
- 1 = Yes; 2 = No (With (1) or without (2) Htilde ?
- 3 : proton polarised along z-axis (along the virtual photon direction)
- 1 : negatively charged lepton (JLab)
- 5.95 (E_{beam})
- $< Q^2 >$
- $< x_B >$
- $Q^{'} = 0$
- $< -t >$
- 3 : As a function of Phi

- 15
- 30
- 345

Bibliography

[1] F. Halzen and A. D. Martin. *Quarks and Leptons*. John Wiley and sons, 1884.

[2] A. W. Thomas and W. Weise. *The Structure of the Nucleon*. Wiley-VCH, 2001.

[3] S. Bass. *The Spin Structure of the Proton*. World Scientific, 2008.

[4] R. Eisberg and R.. Resnick. *Quantum Physics of Atoms, Molecules, Solids, Nuclei, and Particles*. John Wiley and sons, 1985.

[5] E. Rutherford. The Scattering of α and β Particles by Matter and the Structure of the Atom. *Philosophical Magazine Series 6*, 21(125):669–688, 1911.

[6] E. Rutherford and J.M. Nuttall. Scattering of α Particles by Gases. *Philosophical Magazine Series 6*, 26(154):702–712, 1913.

[7] N. Bohr. On the Constitution of Atoms and Molecules. *Philosophical Magazine Series 6*, 26(151):1–25, 1913.

[8] Editor. Physics at the British Association. *Nature*, 106(2663):357, November 1920.

[9] J. Chadwick. Possible Existence of a Neutron. *Nature*, 129:312, 1932.

[10] J. Beringer et al. Review of Particle Physics. *Physical Review D*, 86:010001, Jul 2012.

[11] W. Heisenberg. Über den Bau der Atomkerne. *Zeitschrift für Physik*, 77(1-2):1–11, 1932.

[12] W. Gerlach and O. Stern. Das magnetische Moment des Silberatoms. *Zeitschrift für Physik*, 9(1):353–355, 1922.

[13] EMC Collaboration: J. Ashman et al. A Measurement of the Spin Asymmetry and Determination of the Structure Function g_1 in Deep Inelastic Muon-Proton Scattering. *Physics Letters B*, 206(2):364 – 370, 1988.

[14] Xiangdong Ji. Gauge-Invariant Decomposition of Nucleon Spin. *Physical Review Letters*, 78:610–613, 1997.

[15] R. Frisch I. Estermann and O. Stern. Magnetic Moment of the Proton. *Nature*, 132:169–170, 1933.

[16] P. J. Mohr, B. N. Taylor, and D. B. Newell. CODATA Recommended Values of the Fundamental Physical Constants: 2010. *Reviews of Modern Physics*, 84:1527–1605, October 2012.

[17] R. Pohl et al. The size of the proton. *Nature*, 466(7303):213–216, July 2010.

[18] G Kubon et al. Precise neutron magnetic form factors. *Physics Letters B*, 524(12):26 – 32, 2002.

[19] L. Koester, W. Waschkowski, and J. Meier. Experimental Study on the Electric Polarizability of the Neutron. *Zeitschrift für Physik A Atomic Nuclei*, 329(2):229–234, 1988.

[20] G Höhler et al. Analysis of Electromagnetic Nucleon Form Factors. *Nuclear Physics B*, 114(3):505–534, 1976.

[21] M. Gell-Mann and Y. Ne'eman. *The Eighfold Way*. Westview Press, 2000.

[22] V. E. Barnes et al. Observation of a Hyperon with Strangeness Minus Three. *Physical Review Letters*, 12:204–206, Feb 1964.

[23] R. P. Feynman. Very High-Energy Collisions of Hadrons. *Physical Review Letters*, 23:1415–1417, Dec 1969.

[24] J. D. Bjorken and E. A. Paschos. Inelastic Electron-Proton and γ-Proton Scattering and the Structure of the Nucleon. *Physical Review*, 185:1975–1982, Sep 1969.

[25] S. Bethke. World Summary of α_s (2012). *Nuclear Physics B - Proceedings Supplements*, 234(0):229 – 234, 2013.

[26] E. Wigner. On the Quantum Correction For Thermodynamic Equilibrium. *Physical Review*, 40:749–759, Jun 1932.

[27] C. Lorcé, B. Pasquini, and M. Vanderhaeghen. Unified framework for generalized and transverse-momentum dependent parton distributions within a 3Q light-cone picture of the nucleon. *Journal of High Energy Physics*, 2011(5):1–40, 2011.

[28] A. Bachetta and M. Contalbrigo. The Proton in 3D. *Nuovo Saggiatore*, 28:1–2, 2012.

[29] A. Bacchetta et al. Semi-inclusive deep inelastic scattering at small transverse momentum. *Journal of High Energy Physics*, 2007(02):093, 2007.

[30] H. Avakian et al. Measurement of Single- and Double-Spin Asymmetries in Deep Inelastic Pion Electroproduction with a Longitudinally Polarized Target. *Physical Review Letters*, 105:262002, Dec 2010.

[31] S.S. Jawalkar. *Measurement of Single and Double Spin Asymmetries in* $\vec{p}(e,e'\pi^{\pm,0})X$ *Semi-Inclusive Deep-Inelastic Scattering*. PhD thesis, The College of William and Mary, 2012.

[32] HERMES Collaboration: A. Airapetian et al. Single-Spin Asymmetries in Semi-Inclusive Deep-Inelastic Scattering on a Transversely Polarized Hydrogen Target. *Physical Review Letters*, 94:012002, 2005.

[33] E. Zemlyanichkina. Measurement of the longitudinal spin structure of the proton at COMPASS. In *Proceedings of Science*, 2012.

[34] R. Hofstadter and R. W. McAllister. Electron Scattering from the Protons. *Physical Review*, 98:217–218, Apr 1955.

[35] R. Hofstadter. Electron scattering and nuclear structure. *Reviews of Modern Physics*, 28:214–254, 1956.

[36] R. Rosenfelder. Coulomb corrections to elastic electron-proton scattering and the proton charge radius. *Physics Letters B*, 479(4):381 – 386, 2000.

[37] M. N. Rosenbluth. High energy elastic scattering of electrons on protons. *Physical Review*, 79:615–619, Aug 1950.

[38] R. C. Walker et al. Measurements of the proton elastic form factors for $1 \leq Q^2 \leq 3$ $(\mathrm{GeV}/c)^2$ at SLAC. *Physical Review D*, 49:5671–5689, Jun 1994.

[39] P. E. Bosted. Empirical fit to the nucleon electromagnetic form factors. *Physical Review C*, 51(1):409–411, 1995.

[40] M. K. Jones et al. G_{E_p}/G_{M_p} Ratio by Polarization Transfer in $\vec{e}p \rightarrow e\vec{p}$. *Physical Review Letters*, 84:1398–1402, Feb 2000.

[41] O. Gayou et al. Measurements of the elastic electromagnetic form factor ratio $\mu_p G_{Ep}/G_{Mp}$ via polarization transfer. *Physical Review C*, 64:038202, Aug 2001.

[42] O. Gayou et al. Measurement of G_{E_p}/G_{M_p} in $\vec{e}p \to e\vec{p}$ to $Q^2 = 5.6$ (GeV)^2. *Physical Review Letters*, 88:092301, Feb 2002.

[43] J. Arrington, P.G. Blunden, and W. Melnitchouk. Review of two-photon exchange in electron scattering. *Progress in Particle and Nuclear Physics*, 66(4):782 – 833, 2011.

[44] M. Kohl. Status of the OLYMPUS Experiment at DESY. In *AIP Conference Proceedings*, volume 1374, 2010.

[45] C. Peña, W. K. Brooks and H. Hakobyan. Experimental Background Studies in the Two Photon Exchange (TPE) Experiment at Jefferson Lab. In *AIP Conference Proceedings*, volume 1265, 2010.

[46] J. I. Friedman and H. W. Kendall. Deep inelastic electron scattering. *Annual Review of Nuclear Science*, 22(1):203–254, 1972.

[47] D. Müller et al. Wave Functions, Evolution Equations and Evolution Kernels from Light-Ray Operators of QCD. *Fortsch.Phys.*, 42:101, 1994. arXiv:hep-ph/9812448v1.

[48] A.V Radyushkin. Scaling limit of deeply virtual Compton scattering. *Physics Letters B*, 380(34):417 – 425, 1996.

[49] Xiangdong Ji. Deeply virtual Compton scattering. *Physical Review Letters*, 55:7114–7125, 1997.

[50] M. Diehl. Generalized Parton Distributions. *Physics Reports*, 388(24):41 – 277, 2003.

[51] M. Guidal, H. Moutarde, and M. Vanderhaeghen. Generalized Parton Distributions in the valence region from Deeply Virtual Compton Scattering. *arXiv:1303.6600*, 2013.

[52] A.V. Radyushkin. Asymmetric gluon distributions and hard Diffractive Electroproduction. *Physics Letters B*, 385(14):333 – 342, 1996.

[53] M. Burkardt. Impact Parameter Dependent Parton Distributions and Off-Forward Parton Distributions for $\zeta \to 0$. *Physical Review D*, 62:071503, 2000.

[54] M. Guidal. Generalized Parton Distributions and deep virtual Compton scattering. *Progress in Particle and Nuclear Physics*, 61(1):89 – 105, 2008.

[55] R. L. Jaffe. *Spin, twist and hadron structure in deep inelastic processes*, volume 496 of *Lectures on QCD*. Springer, 1997.

[56] M. Vanderhaeghen, P. A. M. Guichon, and M. Guidal. Deeply virtual electroproduction of photons and mesons on the nucleon: Leading order amplitudes and power corrections. *Physical Review D*, 60:094017, Oct 1999.

[57] Belitsky A. V., Müller D. and Kirchner A. Theory of deeply virtual Compton scattering on the nucleon. *Nuclear Physics B*, 629:323 – 392, 2002.

[58] M. Guidal and M. Vanderhaeghen. Double Deeply Virtual Compton Scattering off the Nucleon. *Physical Review Letters*, 90:012001, Jan 2003.

[59] G. Piller and W. Weise. Nuclear deep-inelastic lepton scattering and coherence phenomena. *Physics Reports*, 330(1):1 – 94, 2000.

[60] S.V. Goloskokov and P. Kroll. The role of the quark and gluon GPDs in hard vector-meson electroproduction. *The European Physical Journal C*, 53(3):367–384, 2008.

[61] A. V. Belitsky and D. Müller. Exclusive electroproduction revisited: Treating kinematical effects. *Physical Review D*, 82:074010, Oct 2010.

[62] H. Moutarde. Extraction of the Compton form factor $\mathcal{H}$ from deeply virtual Compton scattering measurements at Jefferson Lab. *Physical Review D*, 79:094021, May 2009.

[63] M. Guidal. Constraints on the generalized parton distribution from deep virtual Compton scattering measured at HERMES . *Physics Letters B*, 693(1):17 – 23, 2010.

[64] F. Gautheron et al. COMPASS-II proposal. *CERN-SPSC-2010-014*, 2010.

[65] A. Biselli et al. Deeply Virtual Compton Scattering with CLAS at 11 GeV. *E12-06-119, Jefferson Lab PAC 30*.

[66] S. Niccolai et al. Deeply Virtual Compton Scattering on the Neutron with CLAS12 at 11 GeV. *E12-11-003, Jefferson Lab PAC 30*.

[67] A. V. Radyushkin. Double distributions and evolution equations. *Physical Review D*, 59:014030, Dec 1998.

[68] M. Vanderhaeghen, P. A. M. Guichon, and M. Guidal. Hard electroproduction of photons and mesons on the nucleon. *Physical Review Letters*, 80:5064–5067, Jun 1998.

[69] M. V. Polyakov and C. Weiss. Skewed and double distributions in the pion and the nucleon. *Physical Review D*, 60:114017, Nov 1999.

[70] P. Kroll, H. Moutarde, and F. Sabati. From hard exclusive meson electroproduction to deeply virtual Compton scattering. *The European Physical Journal C*, 73(1):1–19, 2013.

[71] A. Bacchetta, U. D'Alesio, M. Diehl, and C. A. Miller. Single-spin asymmetries: The Trento conventions. *Physical Review D*, 70:117504, Dec 2004.

[72] CLAS collaboration: Girod, F. X. and others. Measurement of Deeply Virtual Compton Scattering Beam-Spin Asymmetries. *Physical Review Letters*, 100:162002, Apr 2008.

[73] S. Chen. *First measurement of deeply virtual Compton scattering with a polarised proton target.* PhD thesis, Florida State University, 2006.

[74] HERMES Collaboration: A. Airapetian et al. Exclusive leptoproduction of real photons on a longitudinally polarised hydrogen target. *Journal of High Energy Physics*, 2010:1–19, 2010.

[75] H. Avakian et al. Deeply virtual Compton scattering at 6 GeV with a polarized-proton target and polarised beam using the CLAS detector. *Jefferson Lab PAC 28*, PR05-114, 2001.

[76] CLAS collaboration: Chen, S. and others. Measurement of deeply virtual Compton scattering with a polarized-proton target. *Physical Review Letters*, 97:072002, 2006.

[77] C.W. Leemann, D.R. Douglas, and G.A. Krafft. The Continuous Electron Beam Accelerator Facility: CEBAF at the Jefferson Laboratory. *Annual Review of Nuclear and Particle Science*, 51(1):413–450, 2001.

[78] M. Missiroli. Proceedings of the International School of Physics "Enrico Fermi". In *Three-Dimensional Partonic Structure of the Nucleon*, 2012.

[79] J. M. Grames et al. Unique electron polarimeter analyzing power comparison and precision spin-based energy measurement. *Physical Review Special Topics: Accelerators and Beams*, 7:042802, Apr 2004.

[80] B.A. Mecking et al. The CEBAF large acceptance spectrometer (CLAS). *Nuclear Instruments and Methods A*, 503(3):513–553, 2003.

[81] M.D Mestayer et al. The CLAS drift chamber system. *Nuclear Instruments and Methods A*, 449(12):81 – 111, 2000.

[82] E.S. Smith et al. The time-of-flight system for CLAS. *Nuclear Instruments and Methods A*, 432:265 – 298, 1999.

[83] M. Amarian et al. The CLAS forward electromagnetic calorimeter. *Nuclear Instruments and Methods A*, 460:239 – 265, 2001.

[84] G. Adams et al. The CLAS Cherenkov detector. *Nuclear Instruments and Methods A*, 465:414 – 427, 2001.

[85] W. Meyer. Ammonia as a polarized solid target material. *Nuclear Instruments and Methods A*, 526:12 – 21, 2004.

[86] C.D Keith et al. A polarized target for the CLAS detector. *Nuclear Instruments and Methods A*, 501(23):327 – 339, 2003.

[87] D. Mahon. *Deeply Virtual Compton Scattering off Longitudinally Polarised Protons at HERMES*. PhD thesis, University of Glasgow, 2010.

[88] Rene Brun et al. *PAW-Physics analysis workstation: the complete reference; version 1.07*. CERN Program Library. CERN, Geneva, 1989. CERN Program Library Long Writeup Q121.

[89] Rene B. and Rademakers F. ROOT - an object oriented data analysis framework. *Nuclear Instruments and Methods A*, 389(12):81 – 86, 1997. New Computing Techniques in Physics Research.

[90] A. Kim. Technical Note 022 Good File List from file rate study. Technical report, Jefferson Laboratory, 2012.

[91] Mher Aghasyan. *Private communication*. CLAS Collaboration, 2012.

[92] Y. Prok. Technical Note 009 Checking for beam scraping on target edges using raster ADCs. Technical report, Jefferson Laboratory, 2012.

[93] P. Bosted and A. Kim. Technical Note 002 Beam position (x,y) and target center (z) from raster ADCs. Technical report, Jefferson Laboratory, 2012.

[94] P. Bosted and A. Kim. Technical Note 004 Tracking from drift chambers to target solenoid. Technical report, Jefferson Laboratory, 2012.

[95] P. Bosted. Technical Note 012 New way of doing Cherenkov mirror matching. Technical report, Jefferson Laboratory, 2012.

[96] P. Bosted, N. Kvaltine, and Y. Prok. CLAS-ANALYSIS-NOTE, Inclusive Polarized Structure Functions g_1^p and g_1^d from the eg1-DVCS experiment. Technical report, Jefferson Laboratory, 2013.

[97] P. Bosted. Technical Note 013 Fiducial cuts based on IC shielding. Technical report, Jefferson Laboratory, 2012.

[98] P. Bosted. Technical Note 021 Photon energy corrections and reduction of backgrounds under π^0 mass peak. Technical report, Jefferson Laboratory, 2012.

[99] A. Biselli, S Pisano, G. Smith, E Seder, and S Niccola. CLAS-ANALYSIS-NOTE: Measurements of single- and double-spin asymmetries for deeply virtual Compton scattering with a polarized electron beam and a longitudinally polarised proton target. Technical report, CLAS collaboration, 2013.

[100] H. Avakian. Private communication. 2013.

[101] V.A. Korotkov and W.-D. Nowak. Future measurements of deeply virtual compton scattering. *The European Physical Journal C - Particles and Fields*, 23(3):455–461, 2002.

[102] K. Joo. Private communication. 2013.

[103] CLAS collaboration: Bedlinskiy, I. and others. Measurement of Exclusive π^0 Electroproduction Structure Functions and their Relationship to Transverse Generalized Parton Distributions. *Physical Review Letters*, 109:112001, Sep 2012.

[104] R Brun et al. *GEANT 3: user's guide Geant 3.10, Geant 3.11; rev. version*. CERN, Geneva, 1987.

[105] S Niccolia. Private communication. 2012.

[106] Louis Lyons. *Data Analysis for Physical Science Students [A Practical Guide To]*. Cambridge University Press, 1991.

[107] R.J. Barlow. *Statistics: A Guide to the Use of Statistical Methods in the Physical Sciences*. John Wiley and sons, 1999.

[108] J.H. Pollard. *Numerical and statistical techniques*. Cambridge University Press, 1977.

[109] R. Barlow. Extended maximum likelihood. *Nuclear Instruments and Methods A*, 297(3):496 – 506, 1990.

[110] Aram Movsisyan. *Deeply virtual Compton scattering off a deuterium target at the HERMES experiment*. PhD thesis, Yerevan Physics Institute, 2010.

[111] Zhenyu Ye. *Transverse Target-spin Asymmetry associated with DVCS on the Proton and a resulting model-dependent constraint on the total angular momentum of quarks in the Nucleon*. PhD thesis, University of Hamburg, 2006.

[112] A.V. Afanasev, M.I. Konchatnij, and N.P. Merenkov. Single-spin asymmetries in the Bethe-Heitler process $e^- + p \to e^- + \gamma + p$ induced by loop corrections. *Journal of Experimental and Theoretical Physics*, 102(2):220–233, 2006.

[113] M. Vanderhaeghen, P. A. M. Guichon, and M. Guidal. Computer code for the calculation of DVCS and BH processes in $ep \to ep\gamma$. *Private communication*, 2012.